CLARKSON UNIVERSITY

Method for the Separation of Toner Particles based on Particle Density Differences

A dissertation

by

Brendan H. Williamson

Department of Chemical Engineering

Submitted in partial fulfillment of the requirements for the degree of

Doctor of Philosophy

Chemical Engineering

December 2005

Accepted by the Graduate School

1/25/06
Date

Dean

INFORMATION TO USERS

The quality of this reproduction is dependent upon the quality of the copy submitted. Broken or indistinct print, colored or poor quality illustrations and photographs, print bleed-through, substandard margins, and improper alignment can adversely affect reproduction.

In the unlikely event that the author did not send a complete manuscript and there are missing pages, these will be noted. Also, if unauthorized copyright material had to be removed, a note will indicate the deletion.

ProQuest Information and Learning Company
300 North Zeeb Road
P.O. Box 1346
Ann Arbor, MI 48106-1346

The undersigned have examined the dissertation entitled *Method for the Separation of Toner Particles based on Particle Density Differences* presented by Brendan H. Williamson, a candidate for the degree of Doctor of Philosophy in Chemical Engineering, and hereby certify that it is worthy of acceptance.

1/23/06	Ruth E. Baltus
Date	**Ruth E. Baltus (Advisor)**
1/23/06	Gregory A. Campbell
Date	**Gregory A. Campbell**
1/23/06	Suresh Dhaniyala
Date	**Suresh Dhaniyala**
1/23/06	Thomas M. Holsen
Date	**Thomas M. Holsen**
1/23/06	Philip K. Hopke
Date	**Philip K. Hopke**
12-5-05	Thomas L. Theis
Date	**Thomas L. Theis**

Abstract

A baseline life-cycle inventory (LCI) performed on toner used in the xerographic process reveals that the system is mainly a classical "cradle to grave" model, although recycle streams within the system improve the overall environmental performance. The majority of the solid process waste produced (95%) is associated with post-toner production processes, and the majority of the air emissions in the system result from energy use. Post-production processes combine for just over 85% of the total energy used in the system, with customer use accounting for 58% of the total. The LCI results also show a 29% reduction in virgin material use and a 24% reduction of solid waste production over the life-cycle when waste toner is recycled.

Full color xerographic copiers and printers produce a mixed waste stream of the four colored toners. To maintain the gains realized through the recycling of toner, a separation process must be developed. In this thesis, the use of centrifugal split-flow thin-celled (SPLITT) fractionation as a method for separating toner particles was examined. The system was designed and operated in the equilibrium mode of SPLITT fractionation, where the separation was based on particle density differences. Numerical modeling showed a significant presence of secondary flows for all channel configurations. The dependence of secondary flow on the Ekman number was quantified and three flow regimes were discovered. For $N_{Ek}>0.05$, secondary flows are isolated near the end walls and are relatively small in magnitude. The vortices transition to a rectangular flow pattern for $0.05>N_{Ek}>0.009$. Below $N_{Ek}=0.009$, secondary flows become less structured, and multiple vortices develop near the end walls. The impact of

secondary flows on the separation show a degradation in the performance as the Ekman number of the system is decreased.

An experimental SPLITT fractionation device was tested as a binary separation process. With the system run in an antiparallel orientation, the recovery of the more dense fraction was very high (90-99.7%), while the recovery of the less dense fraction was much lower (60-75%). This result was predicted by the numerical model due to the orientation of the vortices in antiparallel systems. An asymmetric outlet splitter was shown to enhance the purity of the more dense fraction without overly degrading the purity of the less dense fraction. With this modification, a purity of greater than 90% was achieved for both outlet streams.

Table of Contents **Page**

List of Figures

List of Tables

Nomenclature

b	Channel breadth
b_1	Breadth of separation channel
b_2	Breadth of outlet splitter
d_p	Particle diameter
f	Correction factor for wall effects
$\vec{F}_C$	Coriolis force
L	Channel length
m	Particle mass
N_{Ek}	Ekman number
R	Radial distance from the axis of rotation to the outer wall
U	Terminal settling velocity
$\vec{v}$	Velocity vector
$\dot{V}$	Volumetric flowrate
$\Delta\dot{V}$	Volumetric flowrate of a differential layer of the carrier fluid
$\dot{V}_a$	Volumetric flowrate of outlet a
$\dot{V}_b$	Volumetric flowrate of outlet b
v_{ax}	Axial velocity in the separation channel
v_{pri}	Primary (tangential) velocity in the separation channel

$\langle v_{pri} \rangle$	Average primary velocity in the separation channel
v_{rad}	Radial velocity in the separation channel
w	Channel thickness
x	Radial distance from the outer wall
y	Axial distance from the end wall
μ	Dynamic viscosity
ν	Kinematic viscosity
$\vec{\omega}$	Angular velocity vector
Ω	Rotation rate

Acknowledgements

There are many people that deserve to be acknowledged for their help in my research experience. First of all I would like to thank Tom Theis. Without the EvMM program, my life would be very different today. Thank you to my advisor and my committee for keeping me on track and focused. To Ted Ritzko and LeRoy Willard in the machine shop, this wouldn't have been possible without your patience and skills. To Goodarz Ahmadi for encouragement and advice. To my family for all of their support and unwavering confidence, even when my own was running low. A number of people at Xerox Corporation, Webster, NY, provided assistance during this journey, including George Vianco, Joe Stulb, Jack Azar, John Laing, Mike Walker, Tom Peer, Mit Turakhia, Frank DiBisceglie, and others. I would like to specifically thank John Ianni for materials,

and Dick Eisemann for saying, "we need to make October 10th work". I also acknowledge the support of the National Science Foundation for the Environmental Manufacturing Management program at Clarkson University, grant DGE 9870646 of the Integrative Graduate Education Research and Training (IGERT) program, Wyn Jennings and Larry Goldberg program directors. Finally, to my wife, thank you for standing beside me through this journey. Finding you was my biggest reward.

This thesis is dedicated to my late grandfather, who never graduated from high school, but was one of the smartest men I have known. There is no substitute for hard work and common sense. Thank you for showing me how to be a man.

Chapter 1: Introduction to Particle Separation Systems

Xerography was a revolutionary invention in document reproduction. Developed by Chester Carlson in the 1930's and 1940's, it has come to be an integral part of the workplace. The xerographic industry has seen remarkable advances in speed and quality of image production in the past few decades. This technology is still improving today with many companies competing for the future in copy and print technology. My research experience at Clarkson University has been closely linked to the xerographic process. Through the Environmental Manufacturing Management program, I was exposed to Xerox Corporation (Webster, NY) as part of a summer internship. The original idea was to form a research topic out of this summer internship, and after much discussion and run-ins with confidentiality problems, the topic of the separation of mixed color toner waste was formed.

Mixed color toner waste results from most full color xerographic processes. Toner is dry ink that creates the image on paper during the xerographic process used in most copiers and some large printers. An inherent problem with the xerographic process is its transfer efficiency of toner from the photoreceptor to the paper. This efficiency (currently around 85-95%) requires that the photoreceptor be cleaned after each copy is made. The toner that is cleaned is collected in a single waste bin. The four colors that go into making a color copy are thus mixed in the bin based on the use of the individual colors by the machine. To initiate the research in toner, and to determine the current state of toner manufacturing and use, a life-cycle inventory was performed on conventional toner. The

conventional method of toner production is a process by which particles are mechanically fractured to the desired size distribution. The methodology and results of this analysis are reported in Chapter 2.

One of the results of the analysis shows a decrease in environmental factors through the use of a recycling loop, where toner waste from production and use is recycled back into the toner manufacturing process. As black and white printers are replaced with full color xerographic devices, the gains realized by the recycling of black toner cannot be maintained with color toner unless a reasonable separation technique can be achieved. The desire to separate toner particles for recycle was the initial driver of the research. Separation techniques explored include: The use of an impactor to separate particles by size; the use of a charge spectrograph to separate particles by their surface charge; acoustic separation processes, which separate particles by their interaction with an acoustic field; field flow fractionation experiments, which separate particles based on a number of criteria; and the use of a density gradient column to separate particles by density.

The impactor is based on the theory that a particle with sufficient inertia will maintain its straight line path in a curving air stream. The separation is by the hydrodynamic radius of the particle and the particle mass. Initial experimentation with a Micro-Orifice Uniform Deposit Impactor (MOUDI) was rather inconclusive, with all four colors showing up on the first five stages. A possible reason for this is that the physical diameter and the aerodynamic diameter of the particles differ greatly. Toner particles are

very rough in nature, and have somewhat of an oblong shape. The size, shape, and surface characteristics all vary widely even among particles of the same color. Thus, an attempt at separating particles based on their aerodynamic diameter was deemed too complex.

Particle separation based on charge is a topic that has had significant research in recent years, most notably in the separation of bulk plastics. Most of this research has been on particles with diameters on the order of a few millimeters [1], but there have been some efforts to separate smaller sized particles based on charge [2]. The theory behind this process is that in an electric field, a force is imparted on charged particles. This force controls the location of the particle. Thus, particles with different surface charges will move along different trajectories. Initial experimentation on a charge spectrograph [3] showed promising results. Thus, this research topic was explored further by a colleague [4].

Density gradient columns have also been used to separate particles [5]. This technique uses a long fluid filled tube in which a density gradient is established such that the density profile along the tube length is linear. This can be accomplished by limited mixing, where the lighter liquid is filled on top of the heavier fluid and then stirred using a stirring stroke of increasing amplitude, starting at the point where the two fluids were layered. Special pouring of the two solutions can also be used to set up the gradient. Once the gradient is set up, it is very stable. Particles are charged at the top of the column and travel down the column until the particle density and the fluid density are

equal. The resolution of the density gradient column can be as high as 10^{-7} g/cc. Closely linked to the density gradient column is density gradient centrifugation. This method uses test tubes and a developed centrifugal force instead of a long column and gravity, but the theory is the same.

The acoustic particle separation process is less developed than some of the other processes, but the concept does have some interesting ideas. This process entails developing an ultrasonic standing wave across a channel. The standing wave is of such intensity that a pressure gradient forces the particles to the center of the channel [6]. An emerging topic from this area is that of particle/particle separations. The interaction of particles entrained in an ultrasonic standing wave with an applied external field causes the particles to deviate from their centerline position. Different particles would have different interactions with the two fields, thus causing the separation of the particles. Such external fields as gravity [7] and electric fields [8] have been used with good initial results.

Competition of fields is also the basis for separations in field-flow fractionation (FFF). This technique combines an external force field, dispersion forces, and a laminar flow profile to facilitate the separation of particles [9]. The separations are based on the residence times in a channel. In the classic theory of FFF, particles are forced to one wall of a thin channel by an external force (gravity, centrifugal, magnetic, electric, flow, etc.) where the particles become concentrated. Diffusion forces resist this concentration and a

concentration profile across the channel develops for each particle set. The average height of the particle set from the accumulating wall determines the residence time.

A related separation technique is split-flow thin-celled (SPLITT) fractionation. This technique again uses flow cells with an external force applied across the channel. The main difference between SPLITT fractionation and FFF is the axis of the separation. FFF is limited to small batch scales due to its use of the channel length for the particle separations. SPLITT fractionation can be run in a continuous fashion due to its use of the channel thickness for the particle separations. Thus, there is potential for scale-up of the SPLITT fractionation process.

The goal of the present work is to investigate the feasibility of separating mixed particle streams using centrifugal SPLITT fractionation. Chapter 3 will examine the system flow properties of both FFF and SPLITT fractionation channels. The CFD program FLUENT (Fluent Inc., Lebanon, NH) was used to analyze the response of the system to specific variables. The models were also used to quantify the particle behaviors within the systems. The results of this analysis showed promise for one operational mode in particular: centrifugal SPLITT fractionation operating in equilibrium mode. An equilibrium SPLITT fractionation device was designed, fabricated, and tested to verify the numerical modeling results as well as to analyze a novel asymmetric splitter design. The system design and performance are reported in Chapter 4.

1.2 References

[1] Xiao,C., Allen, L., Biddle, M., and Fisher, M. **Presented at SPE's Annual Recycling Conference**, Dearborn, MI, Nov. 9-11, (1999).

[2] Eichas K., and Schonert K., **Proc. 18th Int. Mineral Processing Congr., Sydney, Australia,** Vol. 2, pp. 417-423, (1993).

[3] Lewis, R. B., Koehler, R. F., and Connors, E. W., *Patent #4,375,673*, **US Patent and Trademark Office**, (March 1, 1983).

[4] Williamson, A.A., PhD Thesis. *to be submitted.*

[5] Oster, G., and Yamamoto, M., **Chemical Reviews**, 63 (3) 257-268 (1963).

[6] Tolt, T.L., and Feke, D.L., **Chem. Eng. Sci.** 48: 527-540. (1993).

[7] Masudo T, Okada T **Anal. Chem.** 73 (14): 3467-3471. (2001).

[8] Yasuda K., Umemura S., Takeda K., **J. Acoust. Soc. Am.** 99 (4): 1965-1970 Part 1 (1996).

[9] Giddings, J.C., **Science**, 260, 1456-1465 (1993).

Chapter 2: Life-cycle Inventory of Toner Produced for Xerographic Processes

2.1 Introduction

One of the main components in the xerographic process is the marking material, or toner. Toner is dry ink that creates the image on paper during the xerographic process used in most copiers and some large printers. It consists of small particles in the size range of 8-13 μm, and is composed of three basic raw materials – polymer, colorant (pigments), and small amounts of additives that help to control the image quality. A diagram of a general toner particle is shown in Figure 2.1. The specific toner for this analysis was chosen due to its high production volume and its use in many of the high throughput xerographic machines.

Working in conjunction with an imaging technology corporation, it was requested by toner plant engineers and upper management that the conventional manufacturing process of toner be evaluated to determine where the greatest environmental concerns lie. Quantifying the improvements associated with recent recycling initiatives was also desired. The conventional method of toner production is a process by which particles are mechanically fractured to the desired size distribution. There were specific industrial concerns regarding energy used and solid waste generated within this process. However, the manufacturing process for toner production is progressing as the industry advances and as environmental considerations become more important. To evaluate the

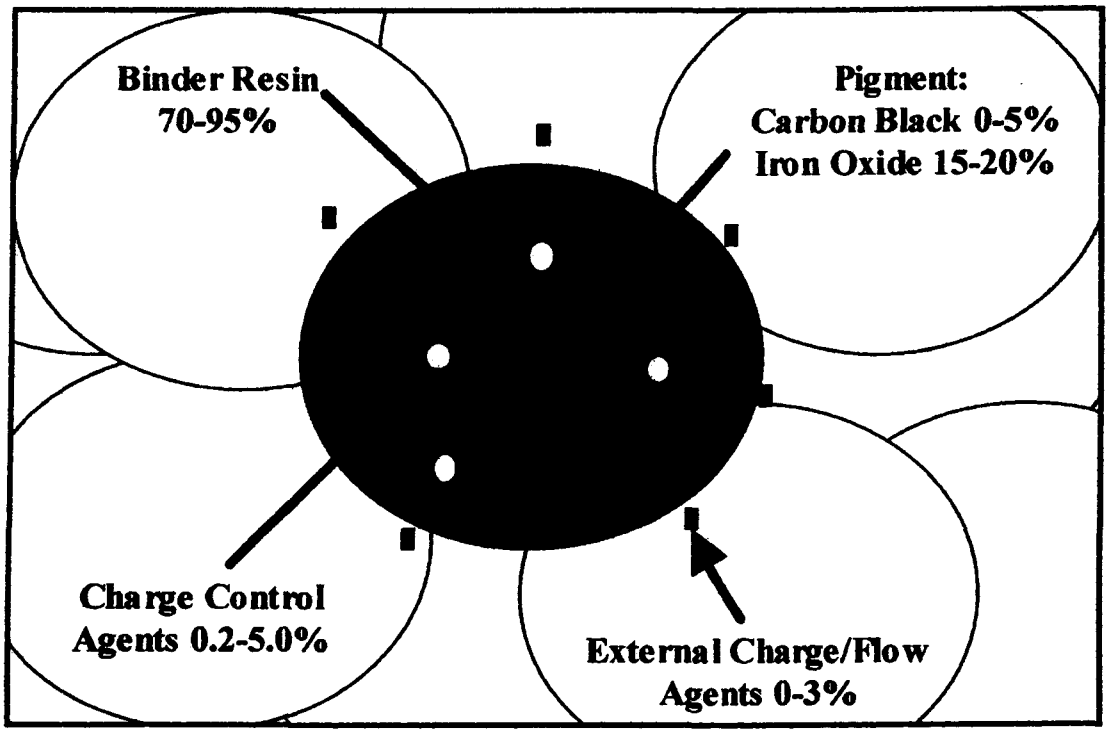

Figure 2.1. Composition of toner particles.

environmental performance of future technologies, the current technology must be evaluated as a baseline. The tool chosen to carry out the baseline evaluation is the life-cycle assessment (LCA). This chapter focuses on the inventory phase of the LCA, specifically the material and energy inputs into the system, along with the wastes produced and by-products leaving the system. These results would determine if the concerns over energy uses and solid waste generated during the manufacturing and use of toner are valid. Therefore, the objectives of the study were to:

1. Establish the boundaries of the life-cycle of toner particles, including all materials and energy required, along with the wastes and by-products produced.
2. Determine areas within the system that have high emissions, material consumption, or energy use levels.
3. Present the resulting data as a baseline in a manner that it could be used to compare the current system to alternative systems and technologies.

2.2 Background

2.2.1 Life-cycle Assessment

A life-cycle assessment (LCA) provides a family of methods for evaluating materials, services, products, processes, and technologies over their entire life [1]. The main goal of an LCA is to evaluate the environmental impacts of a particular process or product from the point where raw materials are extracted from the earth, through manufacturing of the product, its use, and the disposition of residual materials. There are four main parts to an LCA: scoping, inventory analysis, impact analysis, and improvement. During scoping,

initial boundaries are set and objectives are defined. Determining the boundaries of the project is a critical step in the LCA, and is based on a number of factors including the goals and scope of the project, the availability of data, and the time and resources available to fill in the data gaps. Inventory analysis is usually quantitative and consists of thorough mass and energy balances on the system. Developing valid approximations for gaps in the data is critical in this phase of the assessment. Impact analysis involves associating inventory analysis data with their corresponding potential environmental impacts, and then using quantitative and qualitative methods to determine the extent of the environmental impacts associated with the system. For example, is a process with a high-energy consumption rate better than a process with high material requirements? The answer may depend on many factors, such as local environmental issues, types of material used, and sources of power. It is clear that this is a complex process, thus the impact component of the LCA has always been very subjective [2]. Therefore, the focus of this paper is on the inventory phase, with minimal emphasis on the impact. Finally, based on the results, optimization and improvement of the system are explored and recommendations are made.

It is important to understand that there are limitations with LCA. The methodology has been described as too complex and data-intensive [3]. It is also often difficult to differentiate among the critical environmental impacts. However, LCA has emerged as an important tool to aid decision makers in their choice of future products and processes. Among other uses, the LCA assists in evaluating processes or products with similar functions to determine which is environmentally preferred.

2.2.2 Xerography

At the center of the life-cycle of toner is the actual xerographic process. A schematic of this process is shown in Figure 2.2. Xerography begins by imparting a positive charge to a photoconducting belt with a corona wire (# 1 in Figure 2.2). Photoconducting materials behave like insulators when kept in the dark and are more conductive when exposed to light. Using this property the image that is to be copied is exposed onto the belt such that light dissipates the charge on the belt in areas of the image without print (# 2). A "latent electrostatic image" is now on the belt. The negatively charged toner is then introduced to the positively charged image on the belt (# 3). Due to the opposite charges, the toner adheres to the image. This leaves a "toner image" of the original on the belt. The paper is then charged with the corona wire and introduced to the belt (# 4). The "toner image" on the belt is then transferred to the paper, again using the charge differences as the driving force. The "toner image" that is now on the paper proceeds through the fuser rolls, which fix the toner onto the paper (# 5). The final step in this process is cleaning the belt (# 6), where the remaining toner on the photo-conducting belt is removed from the belt and transferred to a waste bin in the xerographic machine.

2.3 Research Methodology

The first step in performing an LCA is to define the boundaries of the system. The system as a whole is shown in Figure 2.3. The system boundaries were initially drawn around the manufacturing process of the toner. The boundaries were then extended

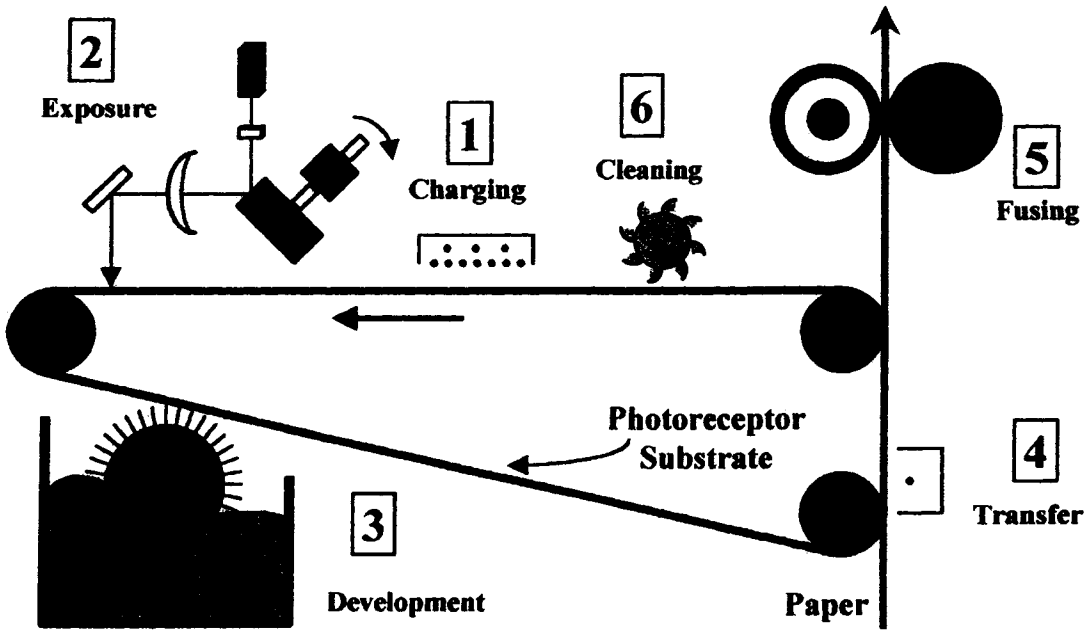

Figure 2.2. The xerographic process.

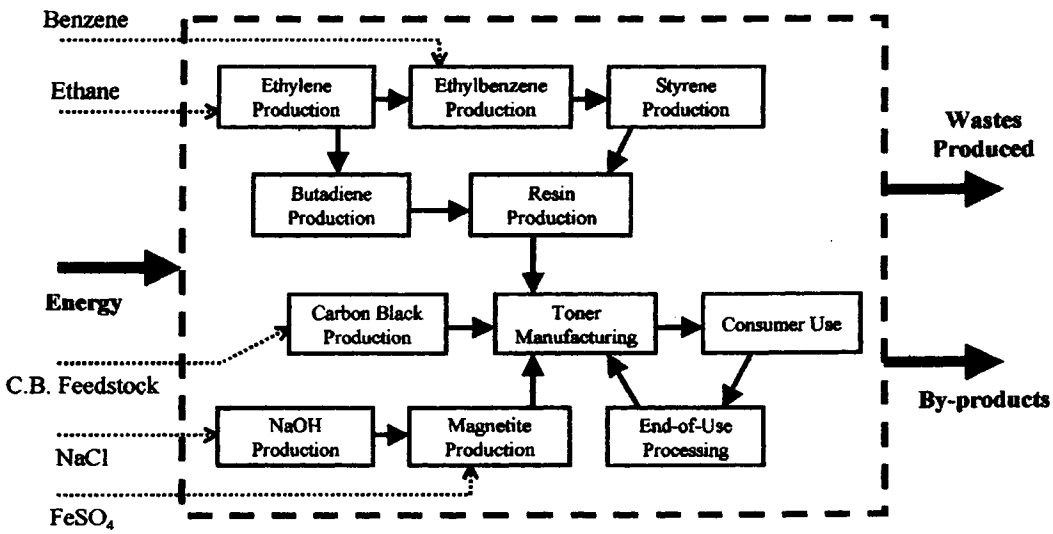

Figure 2.3. The system: life-cycle of xerographic toner.

upstream to include all processes needed to manufacture the raw materials for the toner manufacturing process such that the material inputs of the system were either by-products of another process or were materials from the processing of natural resources. The upstream boundary does not include the mining and extraction of the natural resources (specifically petroleum, natural gas, and rock salt). The boundaries were then extended downstream to include post manufacturing processes such as customer use, paper recycling, and the toner recovery process. The system was then grouped into six sections and evaluated for both material and energy demands, along with by-products and wastes produced: carbon black production, magnetite production, resin production, toner manufacturing, consumer use, and end-of-use processing. Transportation of material between these sections was also considered. The sections are described in detail below emphasizing data collection methods, assumptions made, and calculations used in producing the final results.

The data categories analyzed in this report are: energy use, which includes fossil fuel use and electricity; CO_2 emissions, which is a major contributor to global warming; NO_x and SO_2 emissions, both of which cause acid rain which is a threat to many lakes and forests; VOCs and particulate emissions, which are local air pollutants; wastewater volume, which must be treated before it is released back into the environment; and solid waste, which would enter the local solid waste management system. Air emissions from energy production were calculated using emission factors developed by the Environmental Defense Fund [4]. These categories encompass the substantial emissions from the system that have significant environmental consequences.

The functional unit used in the data calculations was one metric ton of toner produced. The current state of the technology for toner usage is such that one metric ton of toner will produce an average of 22 million images assuming standard letter sized paper and a 6% coverage area [5]. It is important to note that this assessment is only on the toner that is used as a marking material in the production of documents, not on the production of a document. Other materials, most notably the paper used and the xerographic machine, would have to be accounted for in a life-cycle assessment of a document.

2.3.1 Toner Manufacturing

The toner manufacturing process is summarized in Figure 2.4, showing mass flows into and out of the process. In toner manufacturing, the raw materials (resin, magnetite, and/or carbon black) are pre-blended and transferred into a compounding process. The compounder has the dual purpose of mixing and heating the material into a homogeneous polymer melt. The melt is then cooled to form solid pellets that have a size range on the order of a few millimeters. The pellets are then placed into a grinding process, which resembles a fluidized bed where the pellets are constantly colliding with one another and pieces of the pellets become fragmented into the micrometer size range. Following this is the classification process, where the desired size distribution is created. Particles that are too large are returned to the grinding process; particles that are too small are sent to a separate compounding process and are then returned back to the grinding process or are fed back to the compounding process directly. Toner particles are then screened, where any left over aggregates are removed and recycled back into the process. Particles within

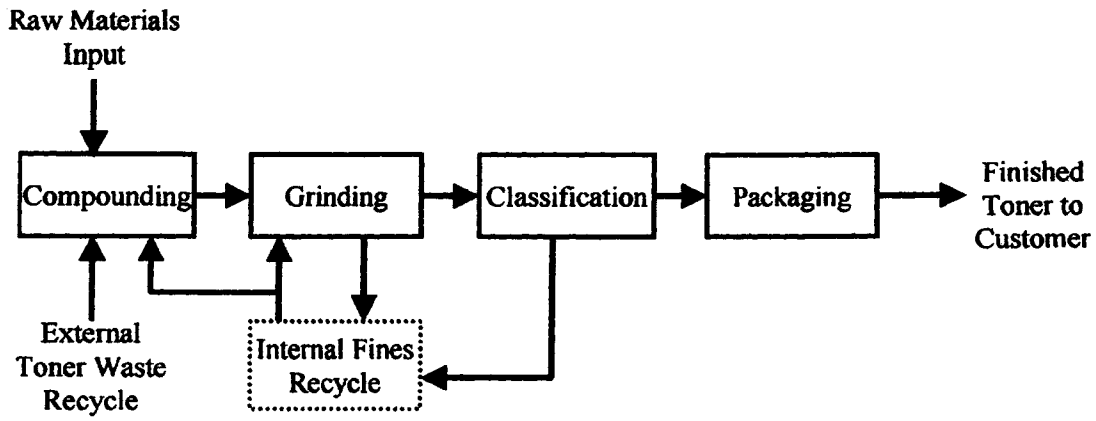

Figure 2.4. Toner manufacturing process.

the desired size distribution are transferred to a packaging line where the bulk toner is packaged and sent to the consumer [5].

In order to reduce wastes and improve toner manufacturing, the industry has taken steps to incorporate recycling where possible. There are two key recycling loops that occur in the manufacturing process. One loop is internal, where toner waste is recycled from the grinder and classifier/screener to a fines recycling process and back into the system. The other loop is external, where toner waste from the consumer is sent to a screening process and then recycled back into the manufacturing process to offset some of the raw materials.

A mass balance was performed based on the main steps of the toner manufacturing process as shown in Figure 2.4. Both internal and external recycling streams were included in the analysis. The mass balance was calculated using the process yield information for the individual steps in the production process. Raw material requirements and intermediate material flows for the production of a specified amount of product were determined. The material flows were labeled and normalized to the functional unit (one metric ton of toner produced). The overall process yield for toner manufacturing was calculated to be 96 - 98%, thus the amount of solid waste produced was relatively low. Determining the total amount of energy consumed during toner manufacturing required collecting data using the nameplate information on all pumps and motors used in the process in order to estimate the energy usage rate. This rate, along with the design rate (the throughput of each machine), and the results from the mass

balance were used to calculate the amount of energy needed to produce one metric ton of toner.

2.3.2 Raw Materials Processing

The three main raw materials used to produce the particular toner studied here are the polymeric resin (80%), magnetite (17%), and the carbon black pigment (3%) [6]. The resin makes up the bulk of the toner particle and is the key to the xerographic process. The melt characteristics of the resin enable the toner to bond with the paper in the xerographic machine. The magnetite and carbon black are both pigment materials, but the magnetite also increases the particles' ability to develop a charge, which is another important aspect in the xerographic process. A charge control agent is also used in this toner, but the weight percent is small (0.2% of total), and the material (a specialty salt) is relatively benign in nature thus the material was neglected. The production processes associated with manufacturing each raw material are described separately below.

2.3.2.1 Resin Production

The resin used in the production of the toner particles is a copolymer of styrene and butadiene. The most common manufacturing process for this resin is a batch emulsion polymerization process [7]. The overall process yield (resin produced / monomer input) is 98%, with the remainder lost as solid waste. For the energy use of the manufacturing process, pump sizes were again used along with the energy needed to heat the reaction slurry to the reaction temperature. The total energy used is assumed to be correct for an

order of magnitude approximation, which will be shown appropriate when comparing these results with other processes within the system that have high energy use.

The material needs for the resin manufacturing process are mainly styrene and butadiene. There are some additives present in small quantities, but these were again assumed to be benign in nature. The styrene and butadiene required for the production of the resin are both derived from organic chemical production and separation methods. Both materials start with products from the steam cracking of ethane that was separated from natural gas [8]. The main product of the cracking process is ethylene, although many other by-products are also produced. One of the by-products from the cracking process is 1,3-butadiene, which is present in the C_4 fraction [9]. The butadiene must be separated from other compounds present in the C_4 fraction, most notably isomers of butane and butene. The most common method of separation used in industry today is extractive distillation. The resulting material flows through this system show very little material losses other than fugitive emissions. For all organic processes within the life-cycle, the fugitive emissions were calculated as a percentage of the total organic material present, according to the boiling point of the material, and listed as VOCs [10]. The butanes, butenes, and other residual organic materials are also separated in the process and used as by-products. Energy use for this process is also low since the boiling points of the materials involved are all near room temperature.

The ethylene produced in the steam cracking of ethane is one of the two chemicals used in the production of ethylbenzene, which is later converted to styrene. The other is

benzene, which is obtained directly from a refinery. The most common process used for the formation of ethylbenzene is called the Mobile-Badger process [11]. The main by-product of this process is a mixed hydrocarbon stream, which can be used as fuel for heating the process stream. The energy required in heating the reactants to the process temperature was calculated to estimate energy use in this step. The energy used in this step was assumed to be derived from the burning of fossil fuels, or more specifically from mixed organic waste streams from the process.

The main use for ethylbenzene is in the production of styrene. The most common industrial process for this conversion is an adiabatic dehydrogenation reaction of ethylbenzene with steam [12]. The elevated temperatures at which the reaction occurs (540 – 650°C) in addition to the endothermic nature of the reaction require significant heat inputs. The main by-products of the process are benzene and toluene, which can be separated or converted to all benzene, and a residual hydrocarbon stream, which can be used as a fuel source for the system. The energy required for the process was again assumed to be derived from fossil fuels and approximated as the energy needed in heating the reactants to the reaction temperature and the heat required to compensate for the endothermic reaction in the reactors.

2.3.2.2 Magnetite Production

Magnetite (Fe_3O_4) is a natural occurring form of iron ore. The purity required to use magnetite as a pigment, however, requires alternative methods of production. One method used to produce pigment grade magnetite is a precipitation reaction of iron

sulfate ($FeSO_4$) with sodium hydroxide [13]. Iron sulfate is a byproduct of titanium dioxide production that uses ilmenite as the raw material. The wastewater from the process contains large amounts of residual salts from the precipitation reaction. The material in the wastewater is mainly sodium sulfate from the reaction, with some sodium hydroxide and magnetite fines present. The sodium sulfate in the wastewater is recovered as a by-product of the process [14]. On a mass scale, three pounds of sodium sulfate are present in the wastewater for every pound of magnetite produced by this process. The energy use is approximated as twice the amount of energy needed to heat the reaction slurry to the reaction temperature to account for the temperature needed to hold the slurry at the reaction temperature and dry the resulting product.

The sodium hydroxide used in the magnetite production process is produced as a co-product of the production of chlorine gas by electrolysis [15, 16]. The caustic solution produced in the electrolysis process is usually concentrated to 50-wt% NaOH during postproduction. The energy requirements for the process have been documented as 2850 kW-h/ton of chlorine gas [17]. The chlorine and hydrogen gas produced are also sold as products, thus the energy used specifically for producing the caustic solution is assumed to be 50% (the approximate weight percentage of NaOH in the total products) of the energy used in the electrolysis process.

2.3.2.3 Carbon Black Production

The carbon black manufacturing process uses high temperatures (2000°C) to break down a hydrocarbon feedstock to elemental carbon [18]. The carbon black feedstock, which is

obtained directly from a refinery, is composed of aromatic hydrocarbons and thus has a high carbon to hydrogen ratio (8:1). Natural gas is used to heat an air stream and remove the oxygen present. The air is then directly used to vaporize and decompose the feedstock to carbon black. Once the process stream has reacted, the carbon black is removed from the process air and pelletized. Any impurities are removed both magnetically and mechanically (screened) before the product is finished. The emissions from this process are mainly from the process air, which can be incinerated for energy recovery. The composition of the incinerated process air is mainly CO_2, H_2O, and N_2, with significant amounts of particulate, VOC, NO_x and SO_2 emissions present [19]. The main energy requirement for this process is in vaporizing the feedstock with the natural gas. The quantity of natural gas used by the process was converted to the heat obtained from the combustion of the gas to comply with the units of energy use by the system.

2.3.3 Post-Production Processes

The post-production processes begin once the manufactured toner is sent to the consumer. The boundaries of the life-cycle extend to the point where the product residuals are disposed or deposited. Post-production processes therefore include the use of the toner in the xerographic machines, the destination of waste toner left in the machines, and the final destination of the toner that is transferred onto the paper (Figure 2.5).

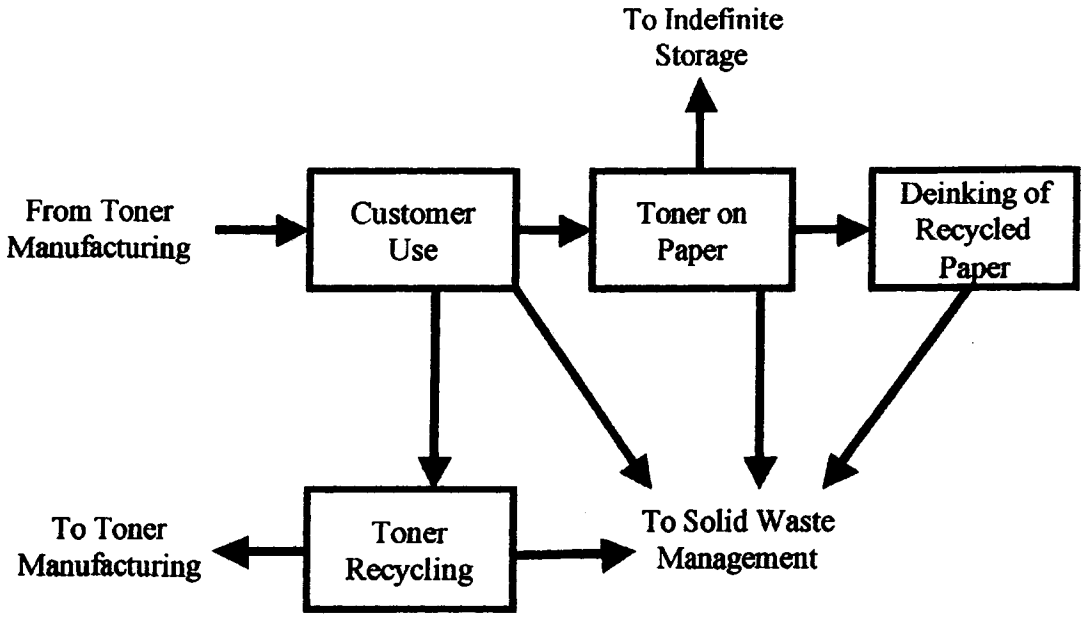

Figure 2.5. Post-production processes.

2.3.3.1 Consumer Use

The internal functions of the xerographic machine were described previously. The most important factors to consider in the LCA are the energy usage during image production, the transfer efficiency of the toner to the paper, and the amount of toner used to produce an average image on a page.

The main energy requirements for the machine are from the exposure of the image onto the belt, and from the fuser rolls, where heat and pressure are used to fix the toner to the paper. Most machines have three operating modes: running, stand-by, and low power. The energy drawn while operating in the three modes (7440 W, 1920 W, and 360 W, respectively), the designed daily volume (17,500 pages per eight hour work day), and reproduction rate for an average machine that uses the toner of interest (135 pages per minute) were used in calculating the energy used in transferring the toner to the paper [20]. It is also important to note that one metric ton of toner makes 22 million copies, which would take over three years on an average machine.

2.3.3.2 End of Use Processing – Toner Waste

The transfer efficiency of xerographic copying is approximately 90% [5]; toner that remains on the photoreceptor is cleaned from the belt and collected in a waste bin. The toner that is collected in the waste bins of the machines can be recycled back into the toner manufacturing process. This recycled toner offsets raw material needs for toner manufacturing. Currently 66% of the waste toner available for recovery is being recovered [21]. Waste toner that is not recovered is assumed to enter the local solid

waste stream. Other material may also accumulate in the toner waste bin, such as paper fibers, staples, and any other material that could be exposed to the photoreceptor. This prevents the direct reuse of the waste material in the machine. Before the waste toner can be reintroduced into the manufacturing process, the impurities must be removed using a screening process. Due to the small size of the toner particles, a screen with a very fine mesh separates the large impurities (paper pieces, staples, etc.) from the re-usable toner. Remanufacturing is a low energy process with much of the operations done manually. Once the toner is screened, it can be reintroduced into the process for toner manufacturing. The screening process is assumed to have a mass efficiency of 95%, although this number could not be verified.

2.3.3.3 End of Use Processing – Toner on Paper

Once toner is bound to the paper by the fuser rolls, the fate of the toner and the paper are the same. Paper used by the machines falls under the general category of "office paper", which is one of the highest quality papers and a good candidate for recycling. Approximately 43% of office paper consumed is recycled [22]. In the recycling of paper, the toner must be removed before new products can be made from the recovered fibers. This process is called "de-inking" and involves both chemical and mechanical processing of the paper as it is re-pulped and the ink is dissolved in the wash water. This is energy intensive since the paper must be slurried in a hot water bath to break up the fibers and dissolve the marking material. The product of the deinking process is pulp, which is used to make recycled paper. To account for the energy needs to remove the toner from the paper versus the energy needs to re-pulp the recycled paper, the energy use for the

deinking process was compared to the energy use in a fiber recovery process. In this process clean scrap paper material from the paper making process is repulped for recycle. This comparison showed that 34% more energy is needed in the deinking process than in the fiber recovery process [23]. Wastewater volumes from the deinking process were also allocated in this manner. The solid waste reported as resulting from the deinking process, however, was only the toner on the paper that was sent to be recycled.

The two other destinations for the paper from the machines are indefinite storage (22% of paper produced), where the paper is filed for later use, or the local solid waste stream (35% of paper produced) [22]. These are both low energy processes, especially compared to the deinking process. Solid waste streams usually lead to a landfill, but there are other forms of managing paper waste, such as incineration or composting. For this report all of the toner on the paper that enters the solid waste stream is regarded as solid waste.

2.3.4 Transportation

The movement of materials between processes must also be considered as part of the life-cycle. Transportation issues include the movement of raw materials from their source to the manufacturing facility, the distribution of the product, and the transportation of all residuals from the use of the product to their final destination. For the calculation of emissions and energy demands in transportation, energy intensity data [24] and emission factors [25] for freight transported by heavy duty diesel truck were used. For the location of the various processes, a central geographic region of the United States was assumed.

All organic processing was assumed to take place in the southwest, the resin and magnetite were manufactured in the midwest, the toner manufacturing facility is in the northeast, and the remanufacturing facility for toner returns is in the southwest. An average distance for the distribution of toner to the customer was also assumed.

2.4 Results

Data collected for this report has been split into seven sections: carbon black production, magnetite production, resin production, toner manufacturing, consumer use, end-of-use processing, and transportation. Table 1 shows the energy needs and emissions for the seven major sections, with subsections included. All of the data has been normalized to the functional unit. Figure 2.6 shows how the different sections of the system compare with one another. The dominance of the post-production processes (consumer use and end of use processing) in the emissions of the system is readily seen. With the exception of VOC emissions and fossil fuel use, post-production processing resulted in greater than 85% of the total value of all categories. The percent contributions from the sections in Figure 2.6 also shows a link between air emissions and energy use, which results from the much larger quantities of energy related air emissions in relation to manufacturing process air emissions.

Customer use is the most energy intensive process of the system. The energy required to transfer the metric ton of toner onto paper (corresponding to 22 million copies at 135 images per minute [26]) consumes 57% of the total energy used during the life-cycle of

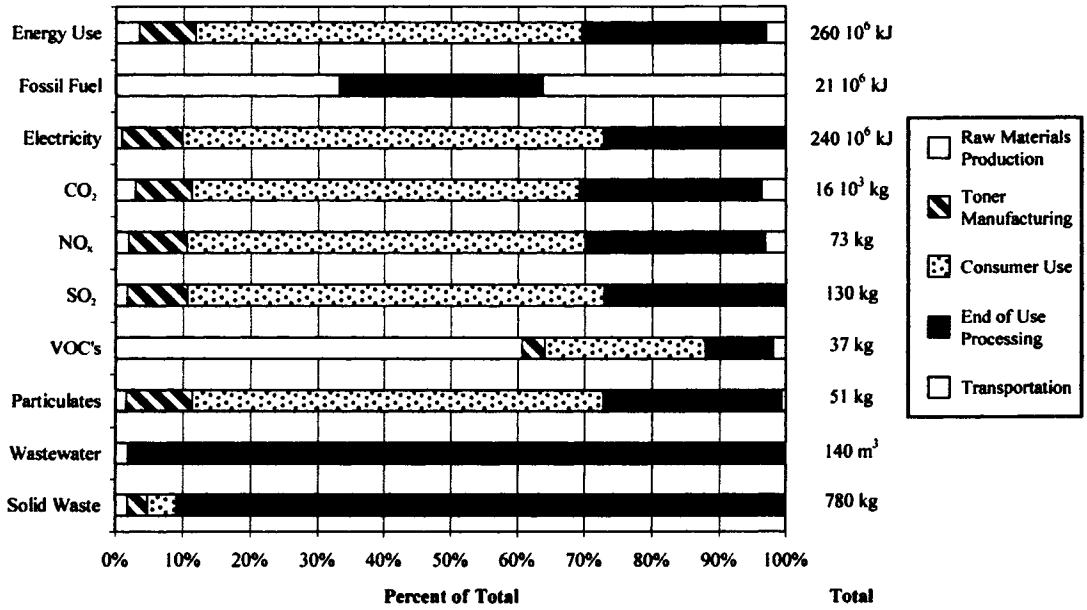

Figure 2.6. Energy use and emissions as a percentage of the total for the system processes.

Table 2.1. Energy use and emissions data for the system processes (per mton of toner).

	Energy Use	Fossil Fuel	Electricity	CO_2	NO_x	SO_2	VOCs	Particulates	Wastewater	Solid Waste
Units	10^6 kJ	10^6 kJ	10^6 kJ	10^3 kg	kg	kg	kg	kg	m^3	kg
Carbon Black Production	**1.5**	**1.5**	**min**	**0.06**	**0.12**	**1.1**	**0.10**	**0.07**	**min**	**min**
Magnetite Production	**2.9**	**1.6**	**1.4**	**0.17**	**0.59**	**0.7**	**0.08**	**0.56**	**1.5**	**min**
NaOH	1.2	0.1	1.1	0.08	0.33	0.6	0.06	0.23	min	min
Magnetite	1.7	1.4	0.3	0.09	0.26	0.1	0.02	0.34	1.5	min
Resin Production	**4.7**	**4.0**	**0.7**	**0.25**	**0.71**	**0.4**	**22.1**	**0.17**	**1.0**	**14**
Ethane S.C.	1.4	1.4	min	0.07	0.18	0.0	1.2	min	min	min
Ethylbenzene	0.7	0.66	min	0.03	0.09	0.0	7.2	min	min	min
Styrene	1.8	1.8	min	0.10	0.24	0.0	6.5	min	min	min
Butadiene	0.1	min	0.1	0.01	0.02	0.0	0.61	0.02	min	min
Resin	0.7	0.11	0.6	0.04	0.19	0.3	6.6	0.15	1.0	14
Toner Manufacturing	**22**	**min**	**22**	**1.4**	**6.2**	**12**	**1.3**	**4.9**	**min**	**23**
Consumer Use	**150**	**min**	**150**	**9.5**	**43**	**82**	**8.7**	**31**	**min**	**34**
End of Use Processing	**72**	**6.5**	**65**	**4.4**	**20**	**35**	**3.8**	**13**	**140**	**710**
Toner Recycle	min	min	min	min	min	min	min	min	min	9.2
De-inking of Paper	72	6.5	65	4.4	20	35	3.8	13	140	390
Toner on Paper to Landfill	min	min	min	min	min	min	min	min	min	320
Transportation	**7.6**	**7.6**	**min**	**0.60**	**2.3**	**0.1**	**0.68**	**0.33**	**min**	**min**
Raw Materials to T. Man.	3.4	3.4	min	0.27	1.0	0.0	0.31	0.15	min	min
Toner to Customer	2.6	2.6	min	0.19	0.73	0.0	0.22	0.11	min	min
Toner Waste Recycle	1.6	1.6	min	0.13	0.49	0.0	0.15	0.07	min	min
Total	**260**	**21**	**240**	**16**	**73**	**130**	**37**	**51**	**140**	**780**

min = minimal to zero use or release

toner. End-of-use processing also has a significant impact, due mainly to the removal of toner from paper that is recycled. Deinking requires large amounts of electrical energy to remove the toner via mechanical and chemical methods. It also results in large effluent flows, accounting for 98% of the total wastewater for the system. The solid waste shown is the quantity of toner that is removed in the de-inking process. The process also results in a large quantity of sludge waste (mostly paper waste, which is not included) that would also enter the solid waste management system.

The industrial concerns with the toner manufacturing process showed to be a relatively small contributor to solid waste, air emissions, and energy use over the life-cycle. Without the recycling initiatives recently implemented at the manufacturing site, however, the production of solid waste from the life-cycle would have been much larger, as shown in Table 2. The recycling streams within the life-cycle are a key factor in reducing both the amount of waste produced, and the amount of raw materials introduced in the process. In regards to the energy use in the toner manufacturing process, the grinding step had the highest energy usage (approx. 80-90% of the total).

The mass flows into and out of the system are also factors in the life-cycle assessment of toner. The material requirements for production in the system and the by-products produced by the system are listed in Table 3. The inputs into the system are mainly products from petroleum and natural gas refineries. A few very small inputs are not listed, such as specialty chemicals in resin manufacturing. In addition, water and air use are not listed as inputs. By-products are products that are used in other sectors of

Table 2.2. Life-cycle improvements associated with recycling toner waste.

Waste/Materials	Without Recycling (kg/mton)	With Recycling (kg/mton)	Percent Reduction
Solid Waste Produced in the Life-cycle	1020	780	24%
Virgin Materials Used in Toner Life-cycle	2530	1790	29%

Table 2.3. Material requirements and by-products of the system.

Material Inputs and Sources	**Quantity (kg/mton)**	**By-product**	**Quantity (kg/mton)**
Ethane from natural gas	240	Light organic products	51
Benzene from refinery	530	Residual organics used as fuel	95
NaCl from rock salt	340	Benzene/Toluene mixed stream	47
$FeSO_4*7H_2O$ from TiO_2 production	510	Chlorine gas	210
Carbon Black Feedstock from Refinery	44	Hydrogen gas	5.8
C_4 fraction from steam cracking of ethane	120	Butanes and C5 fraction	36
Other toner fines from recovery facility	117	Na_2SO_4 salt	260
Total Inputs	**1900**	**Total By-products**	**700**

industry. Some of the by-products can be reused directly by the system, such as burning the residual fuel for heating.

2.5 Discussion

The overall mass balance of the system shows that material enters mainly as virgin raw materials and leaves mostly as non-usable waste. The exit points for the waste are principally through solid waste, such as fines from a dryer. The largest source of waste, as with most "cradle to grave" processes, is the solid waste resulting from the end-of-use processing. The recycle stream from the toner waste generated by the customer to the toner manufacturing process and the in-plant recycling of toner fines do show the beginning of a move to closed-loop production, but the system is still far from the desired "cradle to cradle" scenario. A true closed-loop process would occur when all of the toner is recoverable from the paper using low energy methods that would leave both the toner and the paper in a usable form.

The results of this study show that the consumer use stage in the life-cycle of toner particles has the highest energy use, thereby generating significant air emissions. This suggests that efforts to reduce energy consumption in the photocopier should be the focus of continual efforts to improve xerography. A small percent reduction in emissions from customer use would have a much larger effect on the system than a similar or sometimes much larger percent reduction in any other stage of the system.

The deinking process associated with the recycling of paper also impacts emission levels. While this result may appear to suggest that recycling paper is a less desirable option than landfilling the paper waste, this is only true with respect to the toner on the paper. Focusing on the energy requirements over the life-cycle of office paper, the use of virgin material in the production process and disposal of the resulting paper waste in a landfill requires 84% more energy than that needed to produce 100% recycled paper [27].

The manufacturing and sale of toner is highly competitive. This study was performed not only to evaluate the environmental emissions resulting from toner over its life-cycle, but also to suggest improvements that could be made within the life-cycle and aid in the decision of using alternative toner manufacturing technologies. As described previously, the conventional process conceptually involves creating large particles and breaking them down mechanically to the desired particle size range. An alternative to this process, currently in development, is a chemical toner process in which nanometer-sized particles are grown to the desired particle size range [28]. A comparison of LCA's of both processes should be a factor in determining which process the industry and society would desire. For example while the current manufacturing process has high energy use, particularly in the grinding step, chemical toner manufacturing results in significantly increased water usage. To perform a comparative LCA, the boundaries of the two systems must be drawn to include identical stages in the life cycle. The functional unit must also be chosen such that a valid comparison can be made. If the new toner increases the transfer efficiency of toner to paper, a more appropriate functional unit for such a comparison would be the toner required to produce a specified number of documents. A

comparison of the energy and material needs for the two processes would show the environmental costs or savings associated with the new technology.

The goal of developing a closed-loop system for toner is difficult to achieve, and in the search for sustainable methods of document storage, the use of toner on paper as a storage media may not survive. As the digital age continues to unfold, new reliable and efficient methods of document storage and retrieval are evolving. Computers and the internet are allowing large volumes of information to be stored, searched, copied, and shared in a fraction of the time and effort of past methods; however, it is not clear that this new technology is better for the environment, or is consistent with a sustainable future. It is important to remember that manufacturing computers and the associated storage media results in a significant amount of waste that must be compared to the wastes associated with producing a hard-copy document. A comparative LCA between storing documents as hard copies on paper and as digital files on a computer would highlight the environmental performance of the two processes. The issue of sustainability would be addressed in part via the overall mass flows and energy demands in the life-cycles. The usability of the residuals from the two systems would also be a factor in the sustainability issue. In the final analysis, the comparative life-cycle assessment of the two systems would aid in determining which technology would be optimal for the management of documents.

2.6 Reference

[1] Allenby, B.R., Graedel, T.E., Industrial Ecology, Prentice Hall, 1995.

[2] Owens, J.W. Life-cycle assessment: Constraints of moving from inventory to impact assessment. J. Ind. Ecol. 1997, 1(1), 37-49.

[3] EPA530-N-00-002, March 2000, www.epa.gov/wastewise.

[4] Duke University, Environmental Defense Fund, Johnson & Johnson, McDonald's, The Prudential Insurance Company of America, and Time Inc. Paper Task Force: Appendix to White Paper 10A, December 19, 1995, 29.

[5] Personal communication - George Vianco, Xerox Corp, Webster, NY, 2000.

[6] Material Safety Data Sheet No. A-0058, Xerox Corp, Rochester, NY, November, 2000.

[7] Proprietary resin production process of Xerox Corp, Rochester, NY.

[8] Ullmann's Encyclopedia of Industrial Chemistry *Ethylene.* Vol. A.10. Weinheim, Germany, 1987, 45-93.

[9] Ullmann's Encyclopedia of Industrial Chemistry *Butadiene.* Vol. A.4. Weinheim, Germany, 1985, 431-446.

[10] Jimenez-Gonzalez, C.; Kim, S.; Overcash, M., Methodology for developing gate-to-gate life-cycle inventory information. Int. J. LCA 2000, 5(3) 153-159.

[11] Ullmann's Encyclopedia of Industrial Chemistry *Ethylbenzene.* Vol. A.10. Weinheim, Germany, 1987, 35-43.

[12] Ullmann's Encyclopedia of Industrial Chemistry *Styrene.* Vol. A.25. Weinheim, Germany, 1994, 329-344.

[13] Ullmann's Encyclopedia of Industrial Chemistry *Pigments, Inorganic.* Vol. A.20. Weinheim, Germany, 1992, 243-369.

[14] Ullmann's Encyclopedia of Industrial Chemistry *Sodium Sulfate.* Vol. A.24. Weinheim, Germany, 1993, 355-368.

[15] Ullmann's Encyclopedia of Industrial Chemistry *Sodium Hydroxide.* Vol. A.24. Weinheim, Germany, 1993, 345-354.

[16] Ullmann's Encyclopedia of Industrial Chemistry *Chlorine.* Vol. A.6. Weinheim, Germany, 1986, 399-481.

[17] Ullmann's Encyclopedia of Industrial Chemistry *Chlorine.* Vol. A.6. Weinheim, Germany, 1986, 458.

[18] Donnet, J., Bansal, R., and Wang, M., Carbon Black. *Production by the Furnace Black Process*, 2nd Edn., 1993, 14-28.

[19] US Environmental Protection Agency. "Carbon Black" *AP-42*, Vol. 1, Ch. 6.1, 5th Edn., 1995, 1-10.

[20] Product Safety Data Sheet No. 0707, Xerox Corporation, Rochester, NY, December 1997.

[21] Azar, J., "Environmental Health and Safety Leadership at Xerox", Symposium on Sustainability, Clarkson University, June 16-19, 2001

[22] American Forest & Paper Association - www.afandpa.org.

[23] Duke University, Environmental Defense Fund, Johnson & Johnson, McDonald's, The Prudential Insurance Company of America, and Time Inc. Paper Task Force: Appendix to White Paper 10A, December 19, 1995, 22.

[24] Greene, D.; Santini, D. (ed.) Transportation and Global Climate Change. American Council for an Energy-Efficient Economy, Washington DC, 1993, 283-316.

[25] Technical Report: GREET 1.5 -- Transportation Fuel-Cycle Model, Argonne Transportation Technology R&D Center, August 1999, Vol. 2, Appx. A.

[26] Product Safety Data Sheet No. 0663, Xerox Corp, Rochester, NY, March 1995.

[27] Environmental Defense Fund, White Paper 3 Appendices, 1995.

[28] Kmiecik-Lawrynowicz, et al., "Process of making toner compositions" US Patent #5344738, September 6, 1994.

Chapter 3: Numerical Analysis of Secondary Flows in SdFFF and Centrifugal SPLITT Fractionation

3.1 Introduction

Field-flow Fractionation (FFF) is a family of separation and characterization techniques, which has become a well developed separation technology since its introduction in the 1960's by J. C. Giddings [1]. This technique combines an external force field, dispersion forces, and a laminar flow profile to facilitate the separation of particles [2]. The separations are based on the residence times in a channel. In the classic theory of FFF, particles entrained in a viscous fluid are forced to one wall of a thin channel by an external force (gravitational, centrifugal, magnetic, electric, flow, etc.) where the particles become concentrated. Diffusion forces oppose the external force, and a concentration profile develops across the channel for each particle set. The average height of the particle set from the accumulating wall determines the residence time. Particles with a higher average height (less interaction with the external field and/or more dispersion forces) will have a shorter residence time than particles closer to the accumulating wall, based on the particle interaction with the flow profile of the carrier solution [3] as shown in Figure 3.1(a).

Another analytical technique that has a basis in FFF is split-flow thin-celled (SPLITT) fractionation [4]. This technique again uses thin channels with a viscous carrier fluid under laminar flow with an external force applied perpendicular to flow to facilitate the separation. The main advantage of SPLITT fractionation over FFF is the ability to

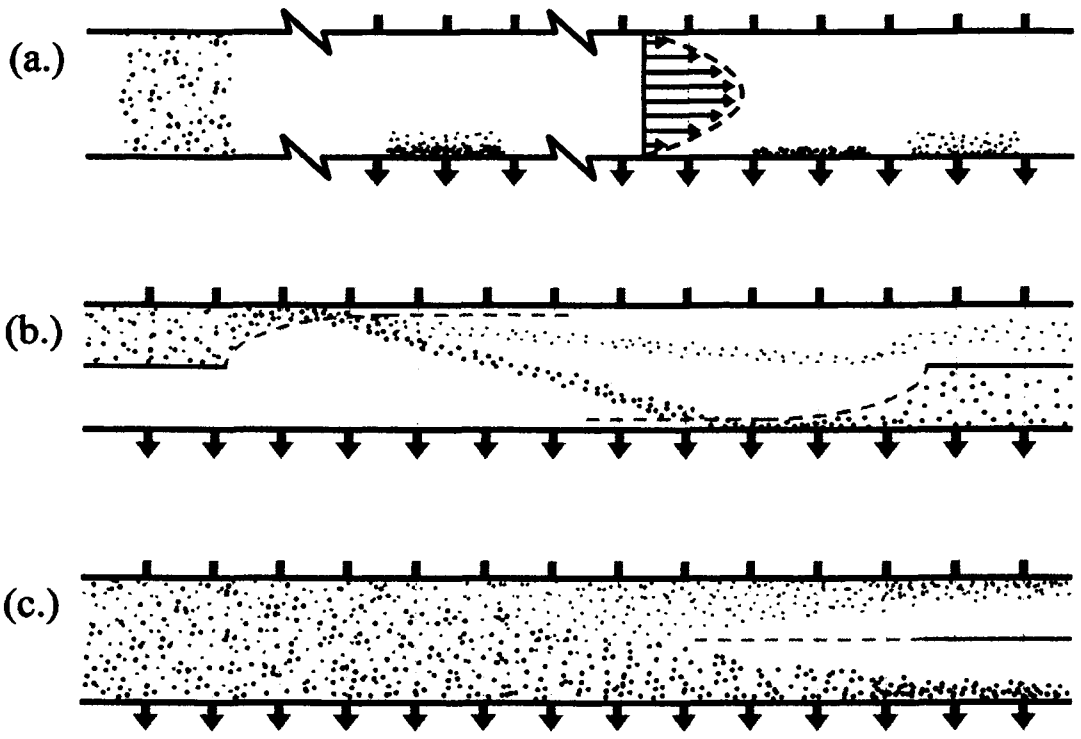

Figure 3.1. Schematic diagram of (a.) FFF, (b.) transport SPLITT fractionation, and (c.) equilibrium SPLITT fractionation.

operate continuously, rather than in a batch mode. There are two operating modes of SPLITT fractionation: the equilibrium mode, and the transport mode. In the transportation mode, particles are initially forced to one wall of a channel through unbalanced flow of two inlets. The external force then transports all of the particles towards the opposite wall. The rate of transport of the particles determines their final location relative to an outlet splitter, as shown in Figure 3.1(b). In the equilibrium mode, only one inlet stream is present so particles are initially dispersed throughout the channel. The applied external force drives particles to an equilibrium height within the channel based on the force balance on the particles, as shown in Figure 3.1(c).

Centrifugal force has been used in FFF and SPLITT Fractionation since the inception of these technologies. Sedimentation FFF (SdFFF) [5] has become a prominent analytical tool, and centrifugal SPLITT Fractionation [6] has been used as a preparative separation technique for many applications including the isolation of human blood cells [7], the separation by size of fly ash for Cd speciation [8], and the fractionation of soil samples by size for soil pesticide concentration analysis [9]. To impart the centrifugal forces perpendicular to the primary direction of flow, the fractionation channels are wrapped around the axis of rotation in a centrifuge. Rotating unions are used to feed fluid into and out of the fractionation channel while the channel is rotating. A typical system set-up is shown in Figure 3.2. Thin channels (typically 0.10–1.0 mm) have been used to minimize the effects of secondary flows on the separation. However, all rotating flow channels with this type of set-up will have some secondary flow. The purpose of this chapter is to quantify the magnitude of these secondary flows and examine the effects of these

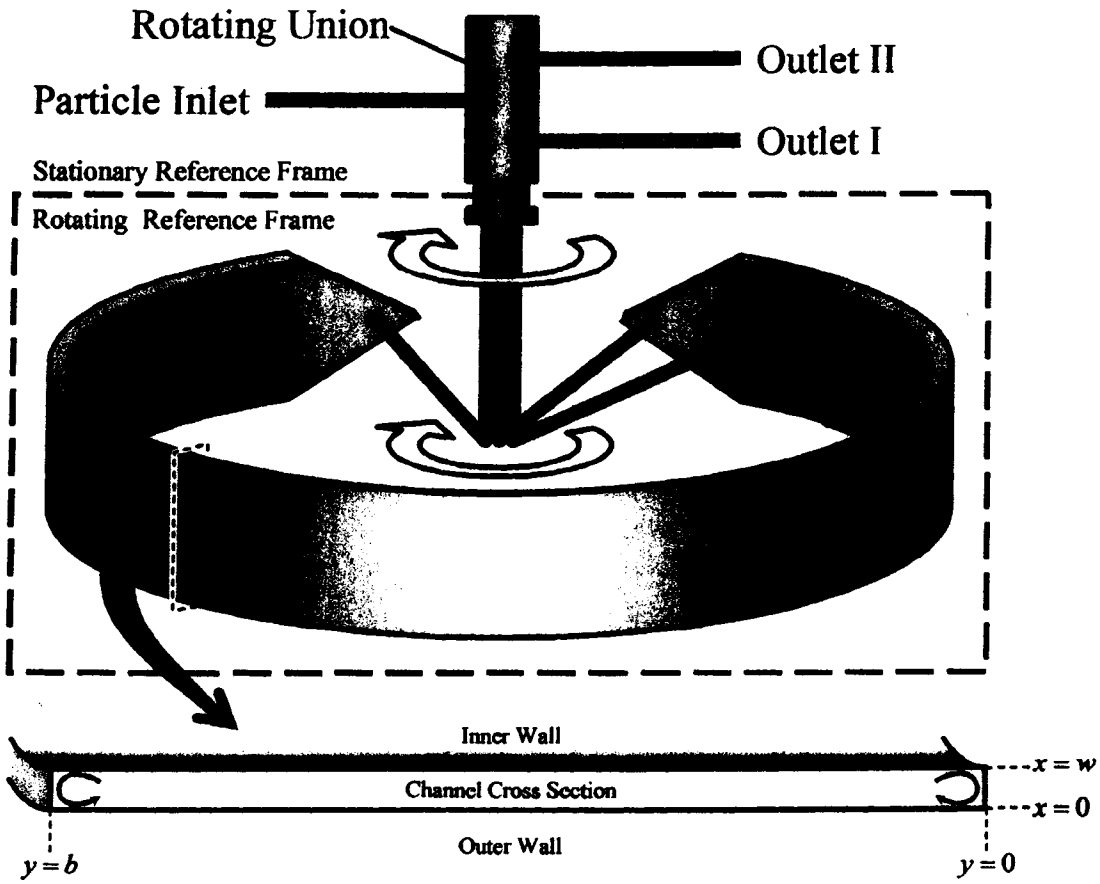

Figure 3.2. Schematic of a centrifugal separation device. For SdFFF, only one outlet is present. For SPLITT in transport mode, two inlets and two outlets are present. For SPLITT in equilibrium mode, one inlet and two outlets are present, as shown.

secondary flows on the particle separations.

The characterization of secondary flows in rotating flow channels has a long history. In the 1920's Dean, was one of the first to theorize the existence of secondary flows and their effects on the primary flow in curved channels [10]. More recent papers have studied the flow characteristics of rotating curved pipes and reported some very interesting flow patterns [11,12], but their calculations are based on systems with much higher Reynolds numbers than those present in SdFFF and centrifugal SPLITT Fractionation channels. Schure and Weeratunga examined the interactions of particles with secondary flows in SdFFF channels and found that to minimize the effects of the secondary flows on particle transport, the system should be run in the antiparallel mode (flow in one direction and rotation in the other) [13].

In this chapter, the analysis of SdFFF and centrifugal SPLITT Fractionation channels is moved beyond identifying general flow patterns. Computational fluid dynamics (CFD) modeling was used to quantify the relationships between a variety of system parameters and the steady state flow properties and particle trajectories. A predictive model is developed which allows for the calculation of the magnitude of secondary flows in a given system. Interactions between particles and the developed flows are also examined with an emphasis on the extent to which the secondary flows disrupt the particles settling trajectories within the flow channel. The scale-up potential of centrifugal equilibrium SPLITT fractionation is also discussed.

3.2 Computational Model

The geometry of the system is shown in Figure 3.2. For the steady state flow in the bulk of the separation channel, models of a thin channel with a rectangular cross section were developed. The dimensions of the channel were varied, along with flow and rotational settings, to analyze the effects of different system parameters on the resulting secondary flows. Three-dimensional modeling of the channels with a structured grid was used in the calculations of the steady state flow properties. The mesh for these channels was generated using the CFD preprocessor Gambit v.2.2 (FLUENT Inc., Lebanon, NH). The axial symmetry of the system was used to reduce the computational domain. In addition, only a small section of the entire channel was needed to determine the steady state properties of the system. Figure 3.3 shows an example of a completed model.

The three-dimensional models were solved using the momentum and continuity equations from the commercial CFD software FLUENT v.6.2 (FLUENT Inc., Lebanon, NH). The boundary conditions were no-slip for the walls, defined inlet and outlet velocities, and symmetry along the middle wall. Laminar flow was assumed, as the Reynolds numbers in the models were all well below the turbulence threshold, and most had a Reynolds number less than 10. The computations were run until the residuals for the velocity and continuity were all below 10^{-6}. The grid is more refined near the end walls than in the center of the channel. This grid structure allowed the secondary flows to be fully resolved. The simulations were run to convergence and the grids were refined until the

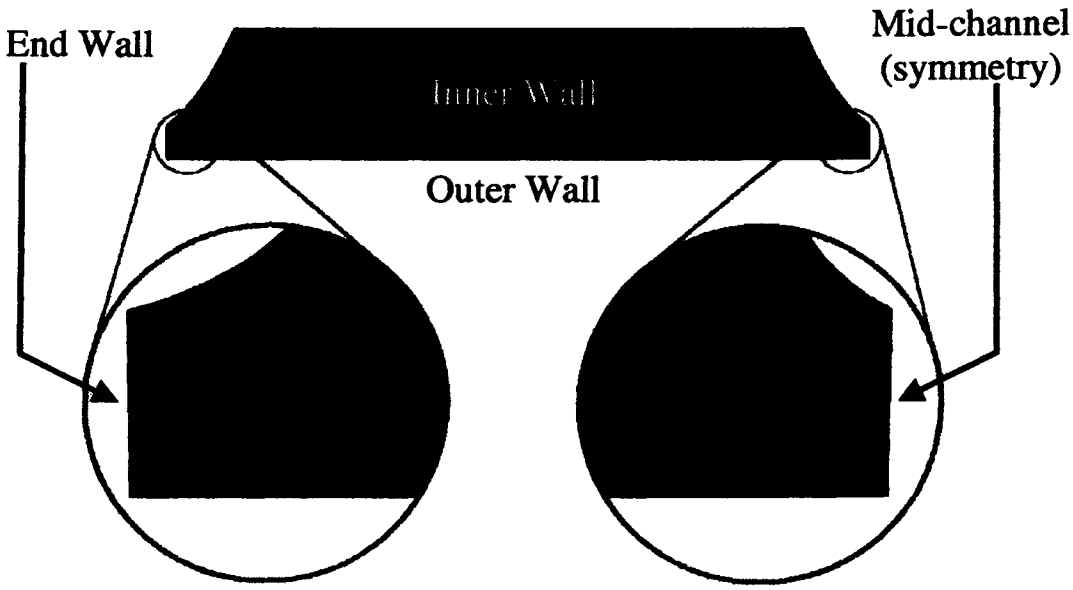

Figure 3.3. FLUENT channel model diagram. The close-up views along the end wall and mid channel symmetry boundaries show the increased resolution near the end wall.

solution for the system flow was invariant. The final models contained approximately 500,000 control volumes. The initial boundary conditions were uniform flow at the inlet and outlet of the system. Once the first solution converged, the flow profile at the central cross section of the channel was obtained. The profile included the relative tangential, axial and radial velocities. This profile was then used as the boundary conditions of the inlet and outlet flows for the next iteration. This process was repeated for three iterations. Subsequent iterations showed no change in the steady state profile. Thus, the steady-state flow in each channel was taken as the flow profile of the central cross section of the third computation.

The relatively short channel lengths used in the three dimensional model were well suited for determining steady state flow characteristics. However, longer channel lengths were needed to examine the particle interactions with the secondary flows within the channels. Thus, a two-dimensional grid was developed using the system symmetry about the axis to examine the particle trajectories throughout the channels. The modeled domain used was a radial cross section of the three dimensional domain. The grid structure in the two dimensional model exactly matched the structured cross sectional grid of the three dimensional model. This grid structure allowed the flow profile calculated in the three dimensional model to be transferred to the two dimensional model. Once the three dimensional model was solved, the resulting flow profile was imported into the two dimensional grid. The axisymmetric rotation about the axis option was used to model the separation channel flows in two dimensions. The particle dynamics within the channels were analyzed by solving Stokes drag using FLUENT's "particle tracking" option.

3.3 Characterizations of flow patterns in the separation channels

3.3.1Coriolis forces in the channels and the Ekman number

The generalized flow patterns in the channels showed that the primary flow in the separation channels away from the end walls are very similar to the parabolic flow patterns seen in the classical solution of flow between two infinite parallel plates. Near the end walls, however, the primary flow slows due to friction with the end walls. This area of low primary flow velocity allows the formation of secondary flows within the system.

The driving force for the development of the secondary flows is the Coriolis force. Coriolis forces are present in rotating objects where there is radial or tangential motion relative to the rotating reference frame. The Coriolis force is given by:

$$\vec{F}_C = 2m(\vec{v} \times \vec{\omega}) \qquad (1)$$

where $\vec{F}_C$ is the Coriolis force vector, m is mass, $\vec{v}$ is the velocity vector, and $\vec{\omega}$ is the angular velocity vector. In this system when the fluid's primary (tangential) velocity and the rotational angular velocity are both in the same direction (acting in parallel), the resulting Coriolis force in the bulk of the channel will be directed radially outward from the axis of rotation. When the fluid's primary velocity and the rotational angular velocity are in opposite directions (antiparallel), the force will be directed towards the axis of rotation. Near the end walls, where the primary flow velocity is reduced due to end wall effects, the relative magnitude of the Coriolis force will be less than in the bulk flow. This imbalance of forces is the source of secondary flows in the separation channel. For

parallel systems, this imbalance results in a secondary flow directed towards the axis of rotation near the end walls of the system. For antiparallel systems, the resulting secondary flows are directed away from the axis of rotation.

The shape of the secondary flow is dependent on the Ekman number, which is defined as the ratio of the viscous force to the Coriolis force. For the system at hand, the Ekman number is defined by:

$$N_{Ek} = \frac{\mu}{\rho w^2 \Omega} \qquad (2)$$

where μ is the viscosity of the carrier fluid, ρ is the density of the carrier fluid, w is the channel thickness, and Ω is the rate of rotation. When the system has a relatively high Ekman number, viscous forces dominate and dampen the effects of rotation on the flow. The resulting secondary flow is an elliptical flow that develops near the end walls, as shown in Figure 3.4(a). In this case, the secondary flows do not extend significantly into the bulk of the channel. However, as the Ekman number decreases, the elliptical flow pattern opens up to a more rectangular flow pattern, with the secondary flows extending into the bulk of the channel. As shown in Figure 3.4(b), the highest magnitude of flow is concentrated in the radial flow at the end walls. This radial flow at the end walls is balanced by an opposing radial flow near the end walls which extends into the bulk of the channel. The axial flow in the channel under these conditions is inversely symmetrical about the radial center of the channel. Its magnitude is also highest near the end walls, and decreases away from

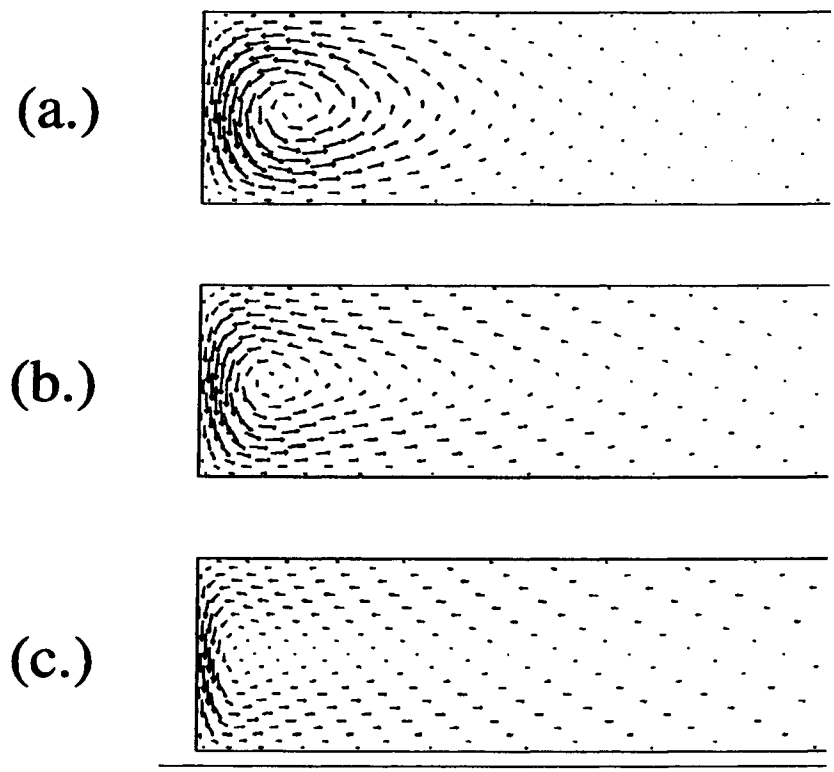

Figure 3.4. Shape of secondary flows at the following Ekman numbers: (a.) N_{Ek}=0.19, (b.) N_{Ek}=0.0093, (c.) N_{Ek}=0.0023. Arrow lengths relate to the velocity magnitude scaled to the maximum secondary velocity for each. For parallel flow, the radial velocity at the end walls is towards the inner cylinder. For anti-parallel flow, the orientation is reversed.

the end walls.

Decreasing the Ekman number further results in complex secondary flows, as shown in Figure 3.4(c). The elliptical flow pattern has now fully developed into a rectangular flow pattern. The radial flow in the channel is concentrated at the end walls, with the balancing radial flow now spread over the bulk of the channel. The axial flows also extend through much of the channel. Separation channels operated under such conditions would be difficult to control, as multiple vortices develop near the end walls and significant secondary flows persist within the bulk of the channel.

The Ekman number also has an effect on the primary flow. When operating at a high Ekman number, the primary flow shows characteristics similar to the flow properties of a channel with no rotation. Decreasing the Ekman number results in an increase in the distance from the end wall for the primary flow to reach its maximum. Decreasing the Ekman number further causes a secondary peak to form near the center of the vortex at the end walls.

3.3.2 Results from numerical models

To quantify the factors that affect the secondary flows in SdFFF and centrifugal SF, a number of numerical trials were developed. Those pertinent to this chapter are listed in Table 3.1. The results of these trials are shown in Figures 3.5 – 3.9. In these figures, the axial velocity (v_{ax}) was taken at $x = w/4$, or one quarter channel thickness away from the outer wall. This is where the axial velocity is at its highest magnitude. The radial (v_{rad})

Table 3.1. System parameters used in the FLUENT models. The direction of flow vs. rotation is (+) for parallel systems and (-) for antiparallel systems.

Trial #	Channel Width (mm)	Rotation Speed (RPM)	Direction of Flow vs. Rotation (+/-)	Average Relative Tangent Velocity (cm/s)	Radius of Curvature (cm)	Channel Breadth (cm)	Aspect Ratio (b:w) (--)	Kinematic Viscosity (m^2/s)	Ekman Number (--)
1	0.254	1,000	+	0.328	15.0	2.0	78:1	1.01E-6	0.148
2	0.254	1,000	-	0.328	15.0	2.0	78:1	1.01E-6	0.148
3	1.016	1,000	+	0.328	15.0	8.0	78:1	1.01E-6	0.00927
4	1.016	1,000	-	0.328	15.0	8.0	78:1	1.01E-6	0.00927
5	0.254	1,000	-	0.328	15.0	4.0	157:1	1.01E-6	0.148
6	1.016	1,000	-	0.328	15.0	4.0	39:1	1.01E-6	0.00927
7	2.032	1,000	-	0.328	15.0	4.0	20:1	1.01E-6	0.00232
8	0.508	1,000	-	0.328	15.0	4.0	79:1	1.01E-6	0.0374
9	1.016	500	-	0.328	15.0	4.0	39:1	1.01E-6	0.0185
10	1.016	2,000	-	0.328	15.0	4.0	39:1	1.01E-6	0.00620
11	1.016	3,000	-	0.328	15.0	4.0	39:1	1.01E-6	0.00310
12	1.016	5,000	-	0.328	15.0	4.0	39:1	1.01E-6	0.00186
13	1.016	10,000	-	0.328	15.0	4.0	39:1	1.01E-6	0.000930
14	1.016	1,000	-	0.328	15.0	4.0	39:1	2.51E-6	0.0232
15	1.016	1,000	-	0.328	15.0	4.0	39:1	5.01E-6	0.0463
16	1.016	1,000	-	0.328	15.0	4.0	39:1	10.0 E-6	0.0930
17	1.016	1,000	-	0.328	15.0	4.0	39:1	20.0 E-6	0.185
18	1.016	1,000	-	0.100	15.0	4.0	39:1	1.01E-6	0.00927
19	1.016	1,000	-	1.000	15.0	4.0	39:1	1.01E-6	0.00927
20	1.016	1,000	-	5.000	15.0	4.0	39:1	1.01E-6	0.00927
21	1.016	1,000	-	0.328	10.0	4.0	39:1	1.01E-6	0.00927
22	1.016	1,000	-	0.328	5.0	4.0	39:1	1.01E-6	0.00927
23	1.016	1,000	-	0.328	15.0	2.0	20:1	1.01E-6	0.00927

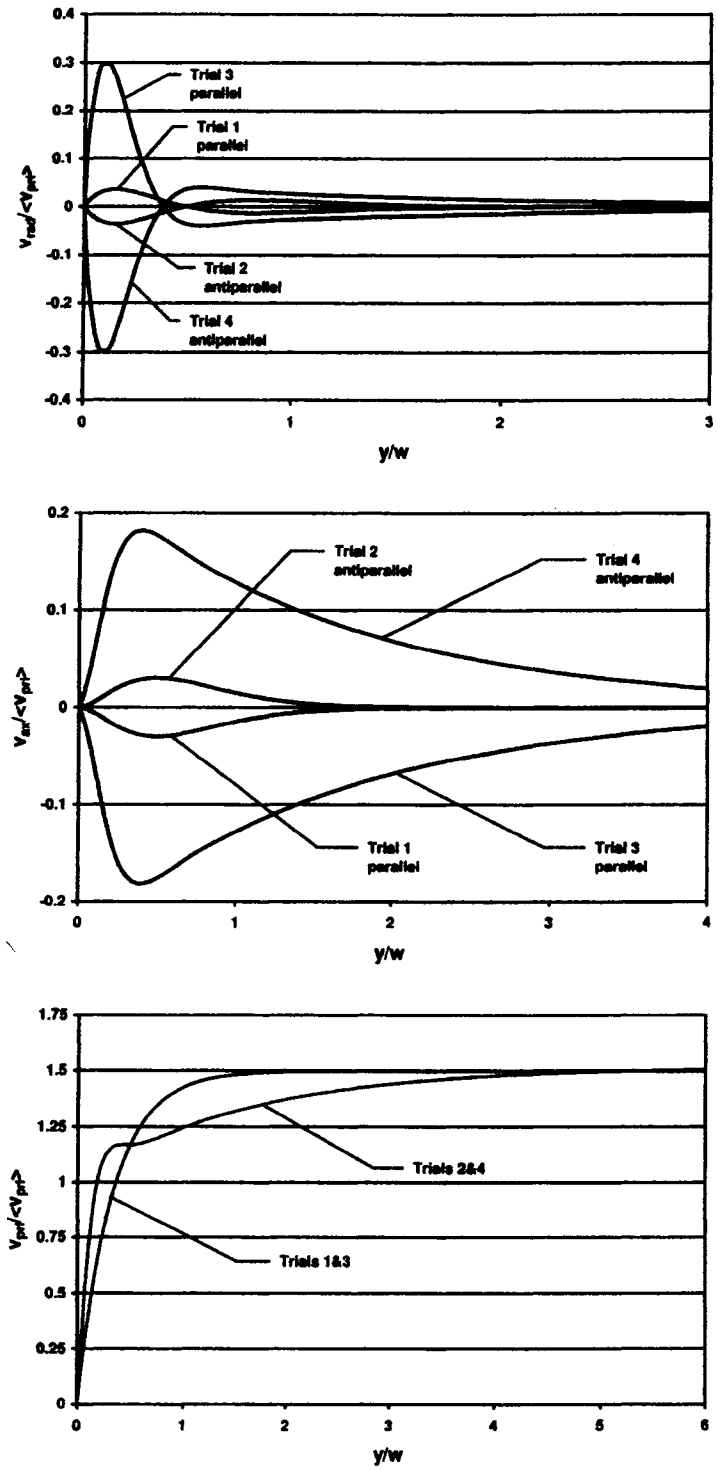

Figure 3.5. Primary and secondary flow components of Trials 1-4, showing the results of changing the orientation between the direction of rotation and primary flow.

and tangential (v_{pri}) velocity profiles are taken at $x = w/2$ or half of the channel thickness. Also, the average primary velocity and the channel thickness are used to non-dimensionalize the velocity and distance parameters in the plots.

Trials 1 – 4 examined the effect of the orientation of the primary flow to the direction of rotation. Figure 3.5 shows that the magnitude of secondary flows was unaffected by this orientation. For systems with rotational properties equal in magnitude but opposite in direction, the direction of the secondary flows was exactly opposite of each other. This reinforces the fact that the Coriolis and viscous forces dominate fluid flow properties within the channel. If the curvature of the channel or centrifugal forces played a large effect on the system, the symmetry between the systems with opposing rotation would not be seen.

Trials 5 – 8 examined the effect of channel thickness on the secondary flows. As shown in Figure 3.6, an increase in channel thickness results in an increase in the magnitude of both the axial and radial flows in the system. The shape of the secondary flows and the primary flow near the end walls is also affected as the secondary flows extend further into the bulk of the channel with increasing channel thickness. Trials 6 and 9 – 13 examined the effect of rotational speed on the secondary flows. In Figure 3.7, a large impact on the magnitude and shape of the secondary flows and a limited impact on the primary flows can be seen. These plots show the transition in the flow properties of the system as the Ekman number is decreased. Higher rotational speeds result in larger secondary flows which extend further into the bulk of the channel.

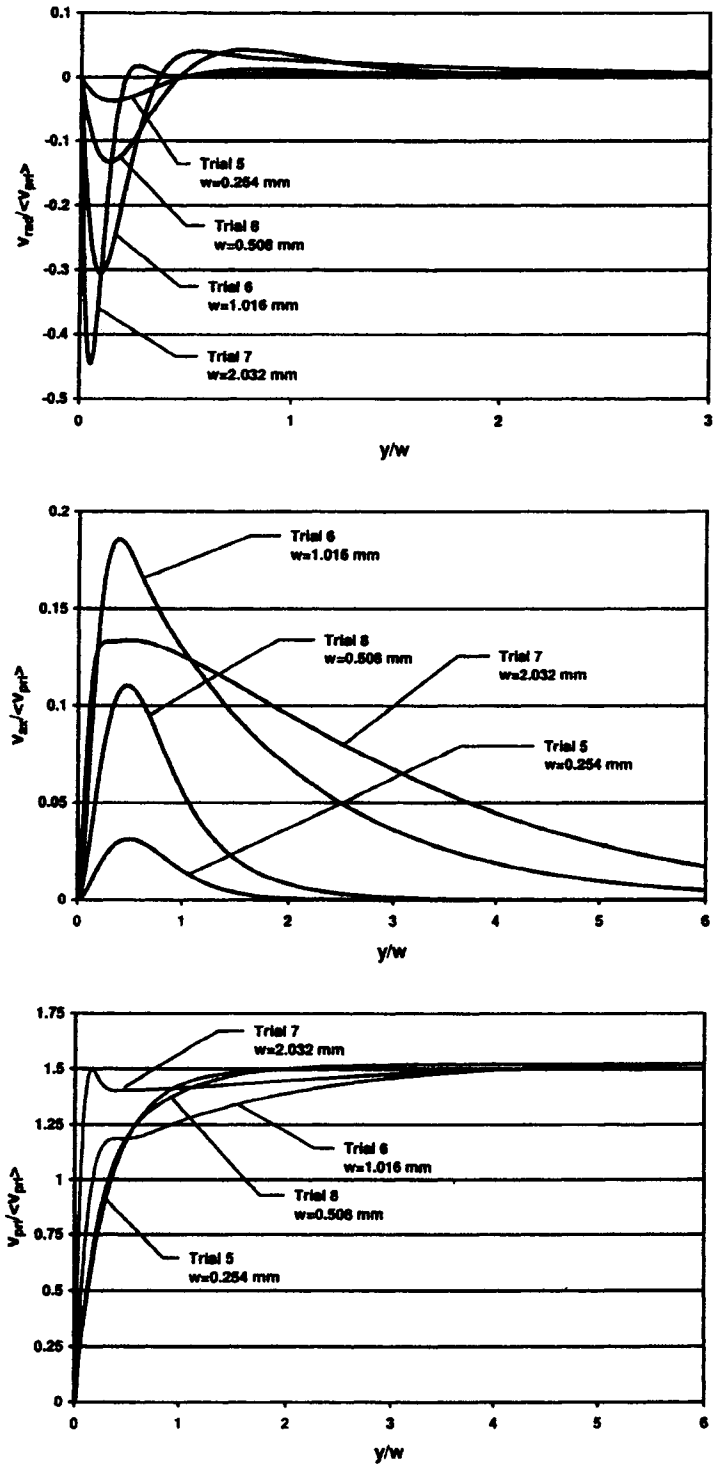

Figure 3.6. Primary and secondary flow components of Trials 5-8, showing the results of modifying the channel width.

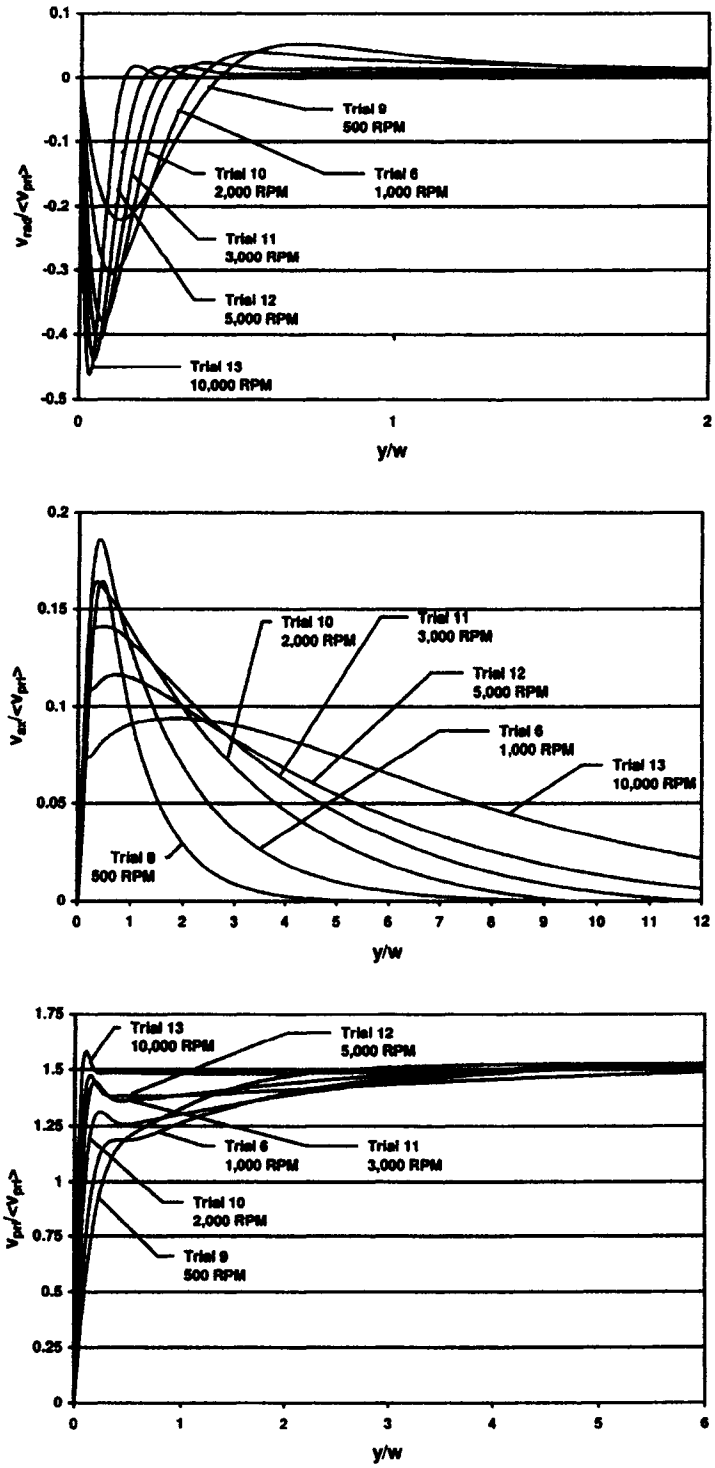

Figure 3.7. Primary and secondary flow components of Trials 6 and 9-13, showing the results of modifying the channel rotation rate.

Trials 6 and 14 – 17 examined the effects of viscosity on the system. The results showed that the viscosity of the fluid has a large effect on the flow profiles in the system. Fluids with a higher viscosity were seen to dampen the magnitude of secondary flows, as well as modify the shape of secondary and primary flows (Figure 3.8). Viscosity, rotational speed, and channel thickness are all variables in the Ekman number, and their impact on the flows behaved as expected.

Trials 6 and 18 – 20 examined the effect of the magnitude of the average primary flow velocity on the different velocity components in the system. A proportional impact on the magnitude of the secondary flows was seen, but the increase in the magnitude of the primary velocity showed no effect on the shape or direction of secondary flows or primary flows. The primary and secondary velocities in the channel, normalized to the average primary velocity, fall in a single curve for all trials (Figure 3.9). Thus, the magnitude of the secondary flow velocity is directly proportional to the magnitude of the primary flow velocity. The magnitude of the primary flow has no effect on the Ekman number, and thus it was not expected to have an impact on the shape of the secondary flows.

The radius of curvature of the channel outer wall is seen to have no significant effect on the primary or secondary flows. Finally, the effects of changing the channel breadth (axial length, or b) showed a slight increase in the secondary flows for trial 23, which had the smallest aspect ratio. The increase resulted from the increase in the primary flow in the center of the channel due to the end wall effects. A further reduction in the channel

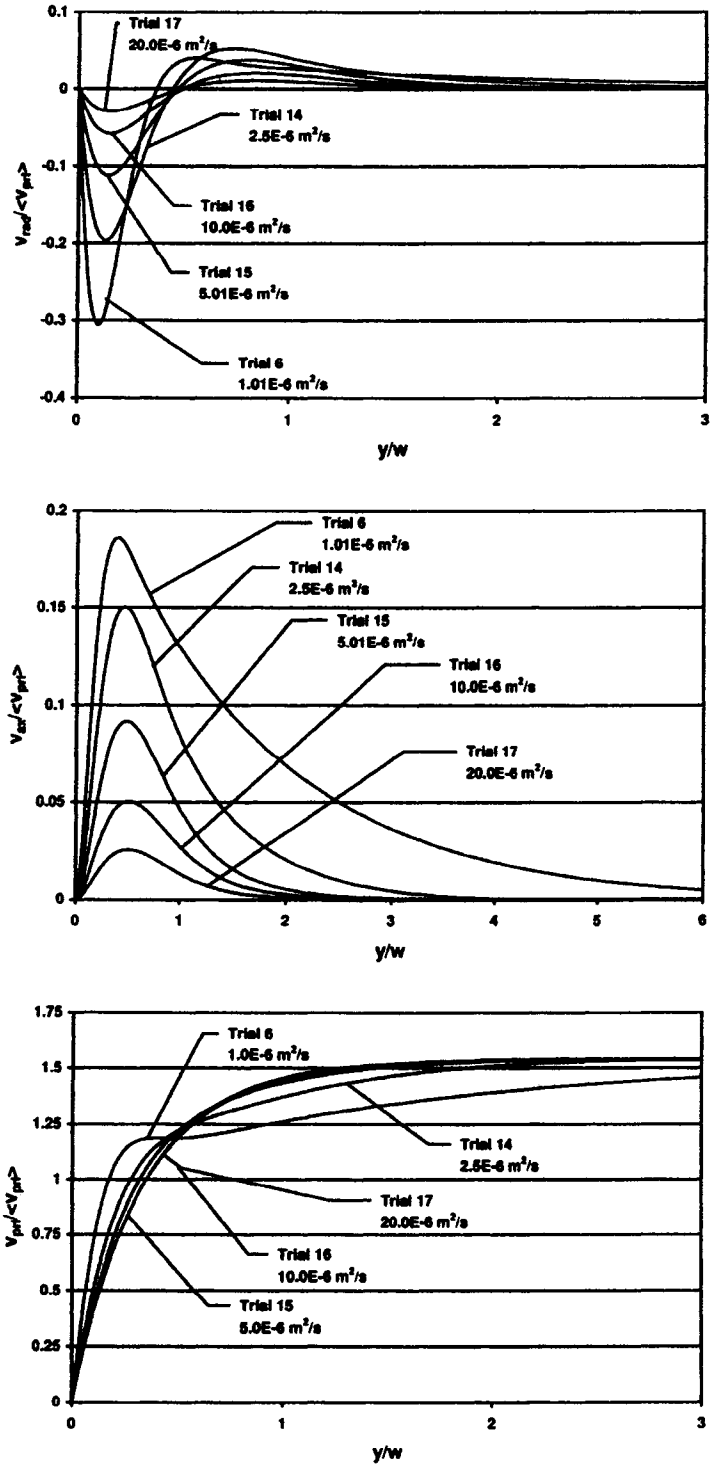

Figure 3.8. Primary and secondary flow components of Trials 6 and 14-17, showing the results of modifying the carrier fluid viscosity.

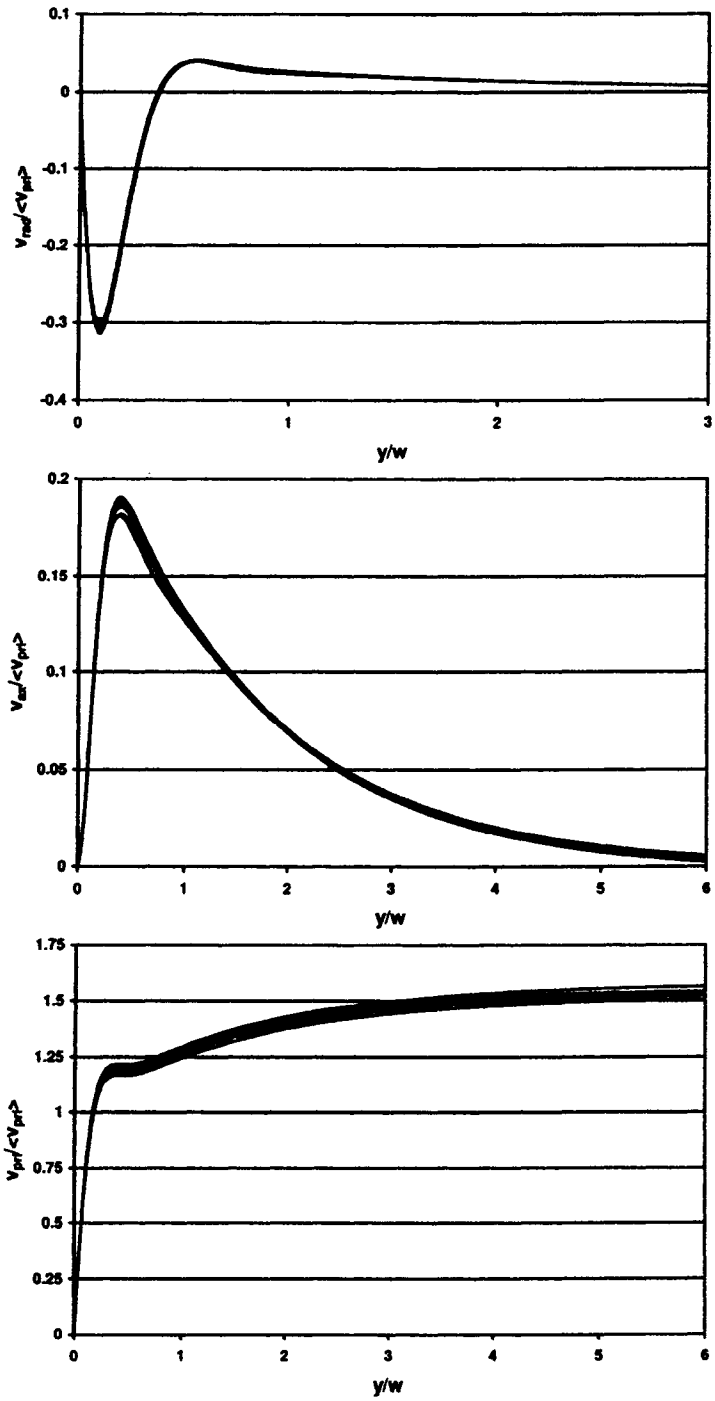

Figure 3.9. Primary and secondary flow components showing the results of modifying the average primary velocity (Trials 6, 18-20), channel breadth (4, 6, 23), and the radius of curvature of the channel (6, 21, 22).

breadth would result in an interaction between the two vortices at the end walls. Such an interaction would not be desirable for the separation systems as the secondary flows would dominate the particle trajectories. The results for both the analysis of the radius of curvature and the channel breadth are also shown in Figure 3.9. The slight variations in the fluid velocities can be seen, but the changes in the fluid velocities are much less significant than those resulting from a shift in other properties identified above.

3.3.3 Results of the analysis

Analysis of flow patterns in centrifugal SPLITT fractionation and SdFFF channels showed some interesting results. The dominance of Coriolis forces and viscous forces in the channel was determined, and the link between Ekman number and the secondary flows was reinforced. To further characterize the secondary flows, Figure 3.10 shows the effects of Ekman number on four main factors of the flow profiles: the maximum magnitude of the radial flow along $x = w/2$, the magnitude of the secondary maximum of the radial flow in the opposite direction, the maximum axial flow magnitude along the $x = w/4$ line, and the distance of the center of the vortex from the end wall. Together, these factors can be used to describe the shape and magnitude of the secondary flows. This plot also shows a strong dependence of the shape of the flow near the end walls on the Ekman number. The continuity of the curves suggests that a prediction of the flow patterns can be made from a system's Ekman number.

For systems operating at $N_{Ek} > 0.05$, the vortices are isolated near the end walls only. In this range, increases in Ekman number result in a decrease in the magnitude of the

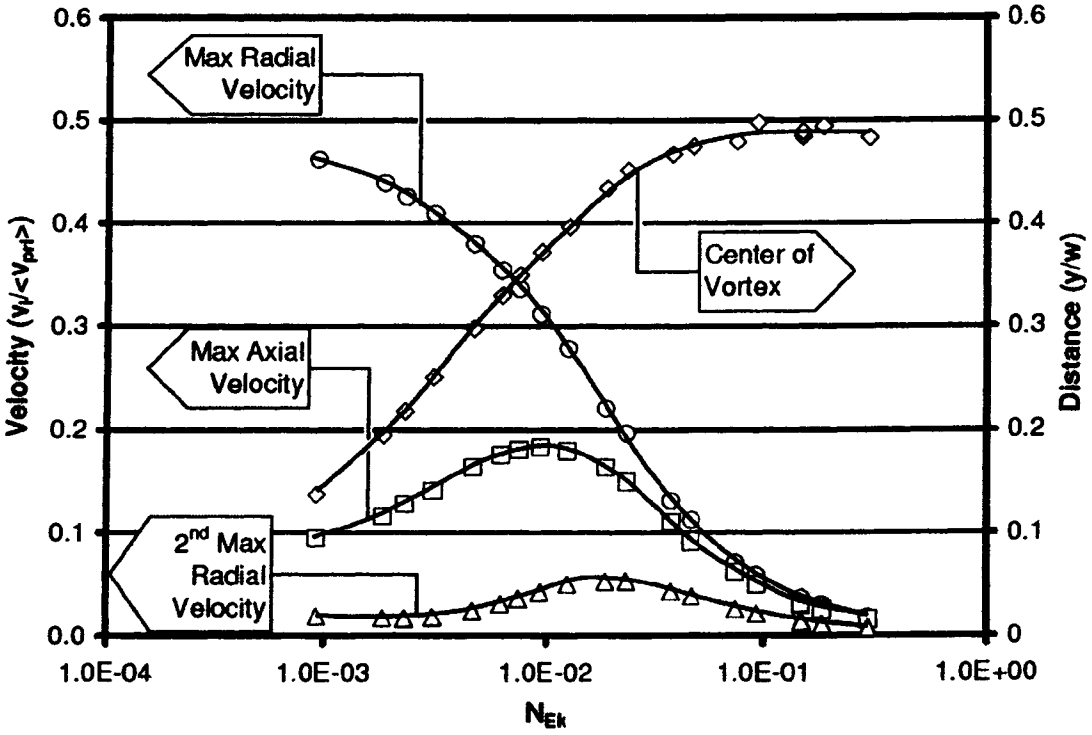

Figure 3.10. Secondary flow properties of thin rotating channels versus Ekman number.

secondary flow velocities. The directional properties of secondary flow velocities are stable in this regime. The center of the vortex remains roughly one-half channel thickness from the end wall ($y/w \approx 0.5$) suggesting a circular vortex formation near the end wall. The primary flow also remains stable in this region of relatively high N_{Ek}. A shift in the flow properties is seen in the "transitional" Ekman number range of 0.05 – 0.009. In this range the simple vortices near the end walls open up towards the bulk of the channel. The shift in the vortex structure is most evident in the magnitude of the secondary maximum of the radial flow. As N_{Ek} decreases, the secondary maximum levels off and begins to decrease as the vortices shift. The center of the vortex also begins to migrate towards the end wall. Thus the flow pattern of the secondary flows shifts from stable elliptical vortices near the end walls to a more rectangular shape which extends well into the bulk of the channel. For $N_{Ek} < 0.009$, complex secondary flows develop near the end walls and extend through the entire channel. The magnitude of the radial flow near the end wall continues to rise, as the vortex is pressed further against the end wall. However, the balancing radial flow in the channel continues to extend into the bulk of the channel, thus reducing its maximum value. Multiple vortices are now present near the end walls which further complicate the flow profiles. The decrease in the maximum magnitude of the axial flow is associated with the secondary flow being squeezed against the end walls. The secondary flow is now rectangular in shape and extends into much of the bulk of the channel, which greatly increases its impact on the system.

Schure, et al., previously studied the characterization of secondary flows in SdFFF channels [13]. A comparison between the results presented here and the results presented

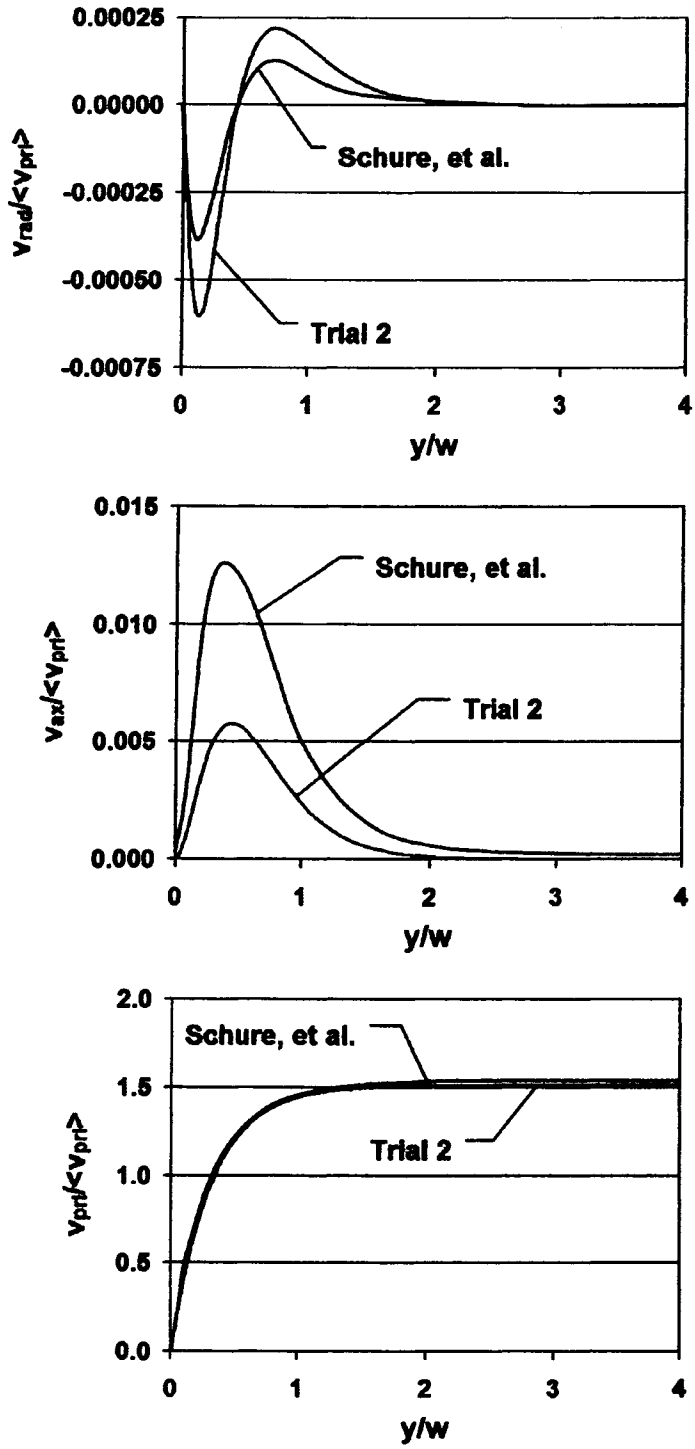

Figure 3.11. Comparison of Trial 2 with the results from a comparable system as reported in Schure, et al. [13].

by Schure, et al., shows agreement between the shape and magnitude of the primary flows as a function of Ekman number. As shown in Figure 3.11, general agreement with the shape of the secondary flows is also seen, although the magnitudes differ somewhat due to the location of the velocity measurements. The radial and axial flows in the channels for Schure, et al., were taken at a line just off of the outer wall of the channel ($x/w \approx 0.0172$). At this location, the maximum axial velocity magnitude found in trial 2 is roughly half of the magnitude reported in the Schure paper. The radial velocity magnitude, however, was roughly equivalent, with trial 2 having a slightly greater magnitude. These values were interpolated within the control volume closest to the wall, so the resolution at this location is not ideal for such a comparison. The agreement of the shape and magnitude of the tangential and radial flows, along with the agreement of the shape of the axial flows does validate the current model.

3.4 Characterization of Particle Motion in the Secondary Flows

The extent to which particles are affected by the secondary flows in the channels has a large impact on the resolution of the separation. Centrifugal, buoyancy, and drag forces, along with diffusion forces for submicron particles, are the main forces involved in particle motion within the system. In the systems at hand, centrifugal forces and buoyancy forces act in opposite directions, with centrifugal forces directed towards the outer wall away from the axis of rotation, and buoyancy forces directed towards the inner wall towards the axis of rotation. The particle density relative to the solution density determines which of these two forces dominates. Particles with a density greater than

that of the solution density will be forced towards the outer wall, while particles with a density less than that of the solution density will be forced towards the inner wall. The rate of particle motion is determined by its drag force. Assuming an absence of secondary flows in the system, the terminal velocity, U, of the particle can be calculated, assuming Stokes drag on the particle, as

$$U = \frac{R\Omega^2 \Delta\rho}{18\mu} d_p^2 \qquad (3)$$

where R is the radial distance from the axis of rotation, $\Delta\rho$ is the density difference between the carrier fluid and the particle ($\rho_{fluid} - \rho_{particle}$), d_p is the diameter of the particle, and μ is the viscosity of the carrier fluid.

The drag on particles due to secondary flows in the separation channels results in their deviation from straight-line trajectories and motion towards the inner or outer walls of the channel. The extent of interaction between a particle and the secondary flows in the channel depends mainly on particle location. In the bulk of the channel, particles are not affected by secondary flows in most separation channels. Particles near the end walls, however, will be affected. Figure 3.12 shows particle trajectories near the end walls for particles with three different densities, all less dense than the carrier fluid. The model used for this example is trial 6. Particle motion is characterized by settling velocity, which directs the particles towards the inner wall. However, the axial flow near the inner wall directs the particles towards the end walls and thus into the vortex. Particles that are entrained in the vortex will continue to circulate within the vortex as they move through

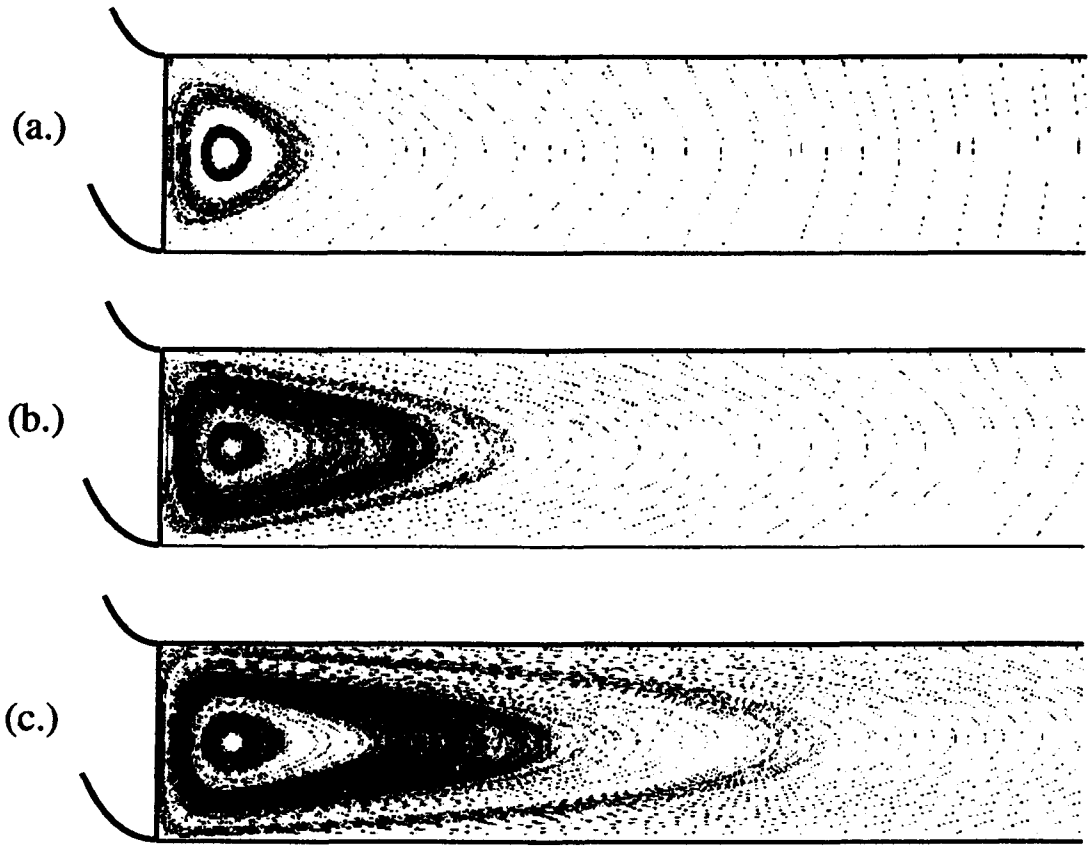

Figure 3.12. Particle trajectories in Trial 6 for 10μm particles. All three cases are for particles less dense than the carrier fluid: (a.) $\Delta\rho = 25.0$ kg/m^3, (b.) $\Delta\rho = 5.0$ kg/m^3, and (c.) $\Delta\rho = 1.0$ kg/m^3, where $\Delta\rho = (\rho_{fluid} - \rho_{particle})$.

the separation channel. Particles with a lower settling velocity are affected by the secondary flows to a much greater extent than particles with a relatively higher settling velocity. In all three cases, particles are entrained in the vortex near the end wall. The distance from the end wall to the axial position where particles are no longer affected by secondary flows is longer for the particles with a lower settling velocity, as seen in Figure 3.12.

In Figure 3.13, motion of particles that are more dense than the carrier solution is shown. The settling velocities act to move particles towards the outer wall. The secondary flows along the outer wall are directed away from the end walls. Thus particles near the outer wall are forced towards the center of the channel and away from the vortex. However, as the particles move through the separation channel, some particles are still entrained in the vortex near the end wall. The particle settling velocity again is shown to have a large influence on this fate, with increasing impact of the secondary flows for particles with lower settling velocities. An area of concentration along the outer wall is also shown in Figure 3.13(b). This results from the particles moving from the end wall to the bulk of the channel.

Particles entrained in a vortex and particles concentrating away from the end wall were also reported by Schure, et al. [13]. The "zone breadth distributions at the outlet" of the channels presented by Schure showed contrasting results for parallel and antiparallel modes of operation. In the parallel mode, the distribution showed an isolated peak in particle concentration near the end walls. The direction of fluid motion in secondary

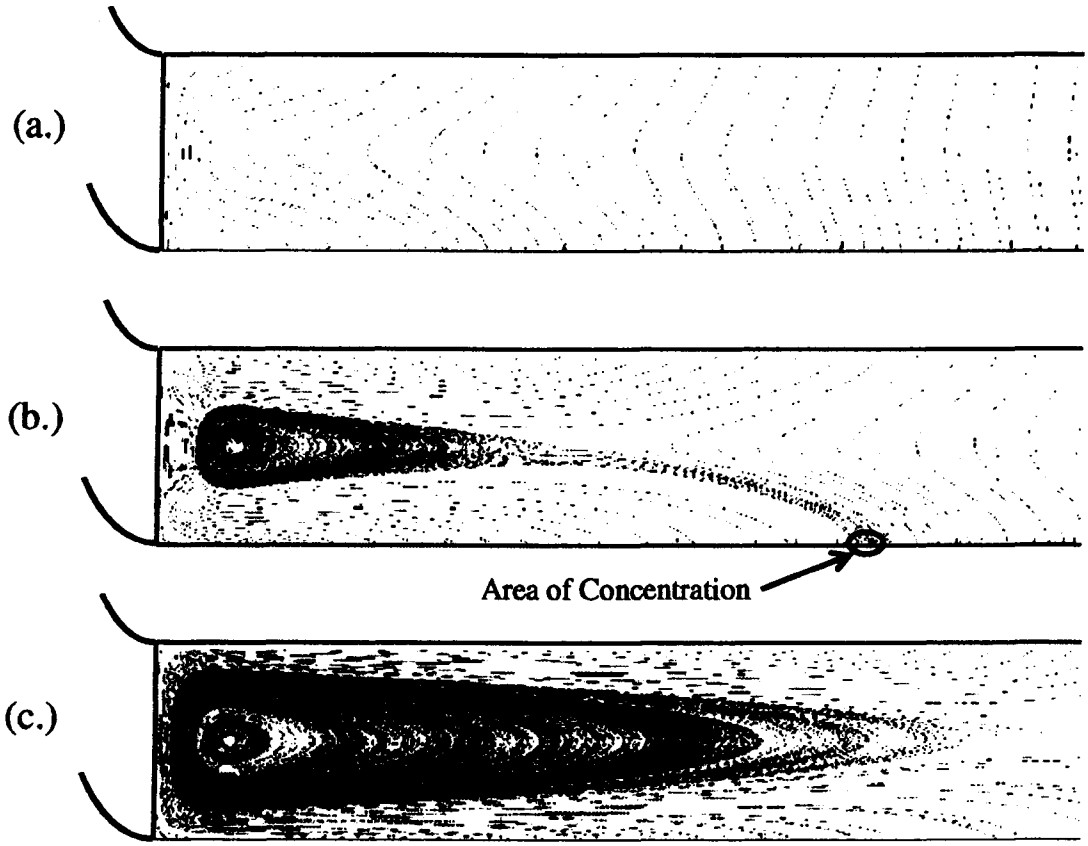

Figure 3.13. Particle trajectories in Trial 6 for 10μm particles. All three cases are for particles more dense than the carrier fluid: (a.) $\Delta\rho = -25.0$ kg/m^3, (b.) $\Delta\rho = -5.0$ kg/m^3, and (c.) $\Delta\rho = -1.0$ kg/m^3, where $\Delta\rho = (\rho_{fluid} - \rho_{particle})$. The location of the area of concentration is also shown in (b.).

flows was reversed in systems operated in parallel mode, and particles near the end walls were forced from the bulk of the channel towards the end walls and into the vortex. This is similar to the results presented in Figure 3.12. In the antiparallel mode, a void is seen near the end walls followed by a spike in particle concentration just before particles in the bulk are encountered. This behavior is due to particles near the end walls being forced away from the end walls and into the bulk of the channel, as shown in Figure 3.13.

The area of increased concentration for particles in Figure 3.13 corresponds to the region where particles that just escape the vortex collect along the outer wall. This point is closer to the end wall for particles with a higher settling velocity. A plot of the particle settling velocity versus the location of this region of concentration is shown in Figure 3.14 for various Ekman numbers. The distance from the end wall to the concentration region is again normalized by the channel thickness, and the settling velocity is normalized by the average primary velocity of the channel. Since the average primary velocity is proportional to the magnitude of the secondary flows for a given Ekman number, the results can be applied to any channel with the specified Ekman number.

Figure 3.14 shows that the secondary flows in high Ekman number channels have very little impact on particle trajectories in the bulk of the channel. Under these circumstances, even for particles with very low settling velocities, the areas affected by the secondary flows are isolated to a few channel widths from the end walls at most. In channels with an Ekman number in the transitional range, however, particles with low

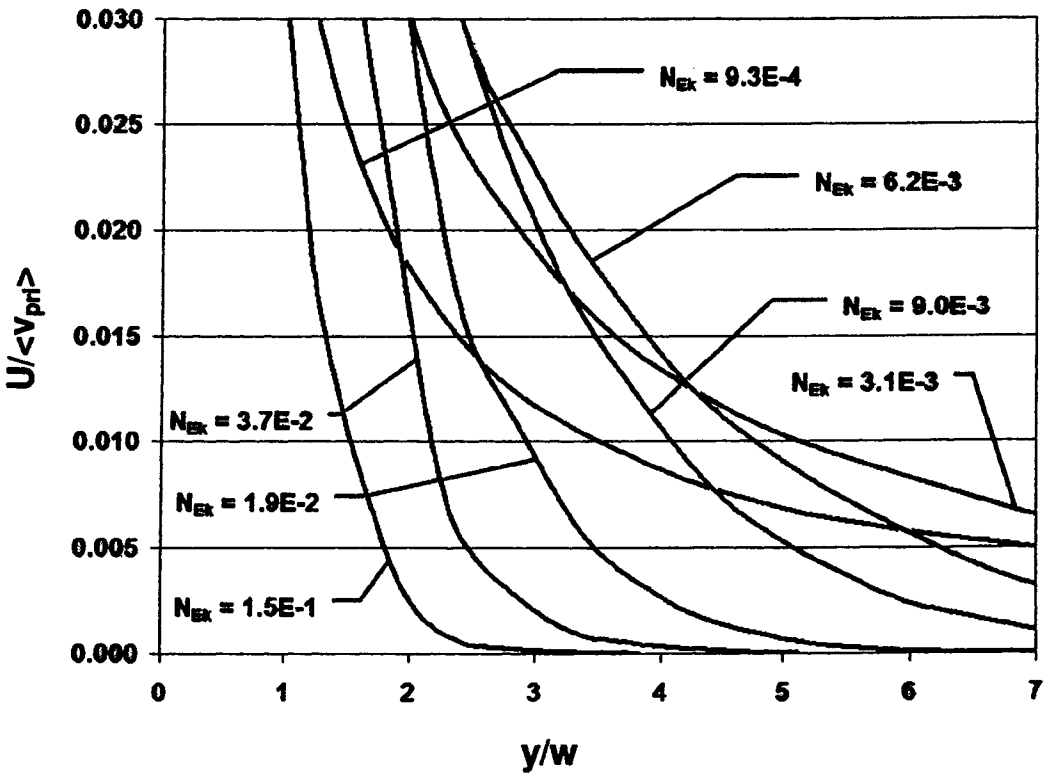

Figure 3.14. Particle settling velocity versus the location of the area of concentration of particles more dense than the carrier fluid for various Ekman numbers.

settling velocities are pushed further into the center of the channel. This corresponds with the expansion of the vortex towards the bulk of the channel. At low Ekman numbers, secondary flows extend well into the bulk of the channel. The radial velocity towards the inner wall, however, decreases in magnitude as this flow is distributed over the entire channel. For the most part, particles that have a higher density than the carrier fluid are no longer caught in the vortex and are largely carried along with the axial flow away from the end wall in the outer half of the channel. This results in a more abrupt transition between particles that have very little interaction with the secondary flows and particles that are greatly influenced by the secondary flows. Particles with low settling velocities will be forced far away from the end walls and concentrated near the center of the channel.

The location of this concentration area is a good indicator of the extent to which the channel is affected by the secondary flows. For instance, for a channel aspect ratio of 80 and Ekman number and particle settling velocity corresponding to an area of concentration at $y/w = 4$, up to 10% of the particles in the channel can be expected to see a significant impact on their trajectories due to secondary flows. The location of concentration given in Figure 3.14 is also useful for systems operating in parallel mode, or for particles that are less dense than the carrier fluid. In such a case, particles along the accumulating wall will be forced towards the end wall and into the vortex. The maximum distance from the end wall that particles in the vortex travel is significantly less than the position reported as the area of concentration. Thus, using the particle

settling velocity and other system parameters, Figure 3.14 can again be used to estimate the extent to which secondary flows will have an impact on particles in the system.

3.5 Effects of Secondary Flows on Particle Separations

The results of the modeling show that secondary flows in the separation channels of SdFFF and centrifugal SPLITT fractionation systems have a significant impact on the system performance. The impact of the secondary flows on the three systems for which these models were developed are discussed below.

3.5.1 Sedimentation FFF

The present results reinforce the conclusion that SdFFF should be run in the antiparallel mode. The concentration step in SdFFF, where particles are forced to the outside wall prior to transport and separation, ensures that the particles will not be transported into the vortex. Near the outside wall the radial flow required to entrain the particles in the vortex is very close to zero. There is, however, the possibility of the concentration effects shown in Figure 3.14 playing a part in the separation. These concentration effects will have the largest impact on zone broadening. As the area of concentration moves away from the end wall, the concentration factor increases proportionately; therefore, channels run at a low Ekman number could see significant leakage due to concentration effects of the secondary flows near end walls.

3.5.2 Centrifugal SPLITT Fractionation – Transport Mode

In contrast to SdFFF, the transport mode of centrifugal SPLITT fractionation, as described in Figure 3.1(b), uses the entire channel width during the separation process. The conventional set-up in centrifugal SPLITT fractionation forces particles towards the inside wall initially through the asymmetric magnitudes of the two inlets. The particles are then allowed to settle towards the outside wall as the primary flow carries them along the channel. This approach exposes the particles to the full effects of the secondary flows. Particle interaction with secondary flows has the potential to disturb the separation process. Following the lead of SdFFF, the direction of rotation and the direction of primary flow are set opposite to one another. The secondary flows resulting from this orientation pull particles near the inner wall into the vortex. These particles would either remain in the vortex during the separation or move away from the vortex along the outer wall. Particles remaining in the vortex would not be allowed to move beyond the outlet splitting plane. Thus, for particles that theoretically should have 100% retrieval in the outer outlet, the actual retrieval factor would be less depending on the percentage of particles that are caught in the vortex. Particles that are influenced by the secondary flows at the end walls but escape the vortex along the outer wall will generally move to the outer wall much faster than similar particles in the bulk of the channel. The result would be the presence of particles in the outer outlet that theoretically should not be there.

This deviation from theory is seen in the results presented by Fu, et al., who did much of the initial development of centrifugal SPLITT fractionation [6]. In their system, the

channel thickness could be adjusted based on the thickness of the spacer layers. Their two channel widths were 762 μm and 381 μm, and both were run from 100 to 800 rpm to examine the retrieval of 1.05 μm polystyrene latex beads. Fu, et al., show the retrieval of the beads in the outer fraction at revolution rates where none should theoretically be retrieved. This result is indicative of particles being transferred to the outer wall via the vortex. The data also show the lack of 100% retrieval of the beads in the outer fraction when theory predicts complete retrieval. This result is indicative of particles being held in the vortex. As the revolution rate is increased, 100% retrieval is achieved, indicating that the increased centrifugal forces on the particles are eventually able to overcome the secondary flows.

The effect of Coriolis forces on particle separations in centrifugal SPLITT fractionation operating in transport mode was identified explicitly in the experimental studies reported by Gupta, et al. [14]. The operating parameters of the Gupta experiments were at such low rotation rates and high flow rates that inertial forces were also a factor in the flow stability. The Rossby number, which is the ratio of the inertial force to the Coriolis force, was used to account for the inertial forces. The results of the experiments showed that as the Ekman number is decreased at a constant Rossby number, the separation efficiency decreases. This effect was attributed to the influence of Coriolis force on particle samples. In their explanation, however, this force acted "in the transverse direction towards the outer wall" and thus increased the settling velocity of the particles above the theoretical settling velocity from centrifugation alone. As discussed above, the direction of the Coriolis force in a system whose angular fluid velocity is opposite to the direction

of channel rotation will be towards the inner wall. Therefore, the direct effect of the Coriolis force on the particle will lead to a very slight decrease in the settling velocity. The larger fraction of "undersized" particles in the outer outlet can be attributed to an increased influence of the Coriolis force in the system, but only through the effect of this force on the development of the secondary flows in the system and the resulting particle trajectories near the end walls. Thus, to minimize the interaction of particles with the secondary flows during the separation, centrifugal SPLITT fractionation operating in transport mode should only be operated at high Ekman numbers.

In the standard system set-up for centrifugal SPLITT fractionation, as stated previously, the direction of rotation and the direction of primary flow are set opposite to one another. However, a purer fraction could be attained in the outer outlet if the system is run with the rotation and primary flow parallel to one another. This would reverse the vortices at the end walls. As the particles are forced towards the inner wall initially, the vortices would push particles towards the center of the channel away from the end walls. As the particles approach the outer wall, particles near the end walls are forced into the vortices. As shown in Figure 3.14, the influence of secondary flows on particle trajectories greatly increases for particles with smaller settling velocities. Thus, larger particles would be affected less than smaller particles. Since the outer outlet collects particles with a larger settling velocity, this removal of smaller particles would enhance the separation. Operating the system in parallel mode, however, would hinder complete retrieval of the outer fraction since some particles that should be collected in the outer outlet would be

forced into the vortex. Nevertheless, the increased purity of the outer outlet fraction may be desirable in specific cases.

3.5.3 Centrifugal SPLITT Fractionation – Equilibrium Mode

The equilibrium mode of centrifugal SPLITT fractionation has not been developed to the same extent as SdFFF or centrifugal SPLITT fractionation operating in transport mode. The separation is based purely on density. Particles that have a higher density than the carrier solution are forced to the outer wall, while particles that are less dense than the carrier solution are forced to the inner wall. In the bulk of the channel, this separation works very efficiently. The presence of secondary flow in the system, however, will affect particles near the end walls for the two fractions differently, as shown in Figures 3.12 and 3.13.

For antiparallel systems, the low-density (relative to the carrier fluid) fraction of particles near the end wall will be forced along the inner wall and into the vortex. The high-density fraction will be forced away from the end walls along the outer wall, with a small percentage residing in the vortex. The particle trajectories of the two fractions suggest three equilibrium locations for the particles: high-density particles in the bulk of the channel along the outer wall, low-density particles in the bulk of the channel along the inner wall, and low-density particles entrained in the vortices near the end walls. For a binary separation with the carrier density equal to the mean density of the two particle samples, the outlet splitter can be modified to collect particles in specific locations in the channel, as shown in Figure 3.15. In the bulk of the channel, the particles will be

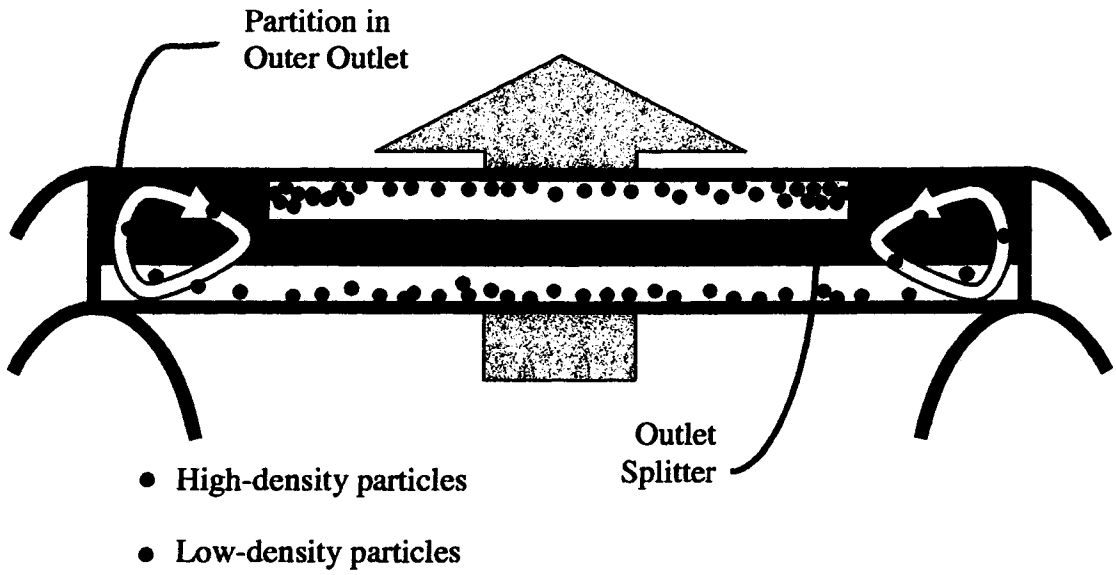

Figure 3.15. Schematic of equilibrium locations for centrifugal SF particles interacting with secondary flows and the novel splitter design.

fractionated simply by their radial location in the channel. Near the end walls, where the low-density particles are entrained in the vortex, the outer outlet can be blocked, thus the particles will traverse to the inner outlet and be fractionated into the correct outlet fraction. The area of concentration given by Figure 3.14 identifies the distance from the end wall that the outer outlet needs to occlude. At this distance, the high-density particles will be concentrated along the outer wall with a relatively small percentage located in the vortex and along the outer wall close to the end walls. The low-density particles in the vortex are isolated closer to the end walls. The trajectories of the low and high-density particles can be visualized by comparing Figure 3.12 and Figure 3.13, where the particle density differences are equal in magnitude and opposite in sign. The addition of this partition in the outer outlet leads to a more complete separation of binary systems. This outlet splitter setup removes the limitation that secondary flows be minimized for high resolution separations. Compensating for the effects of secondary flows on the equilibrium position of the particles allows for higher rotation rates, which is the most dominate factor in the settling velocity equation. The increased speed of the separation would allow for an increase in the throughput of the system. Coupling high rotation rates with other methods of increasing system throughput (higher particle concentrations, larger channel breadths and lengths, etc.) could result in the development of high purity separations in binary systems on a preparative or industrial scale.

3.6 Conclusions

The numerical models presented in this chapter support the conventional set-up of SdFFF to be operated in antiparallel mode. This results in particles being forced from the end walls along the accumulation wall toward the bulk of the channel. For centrifugal SPLITT fractionation, the models show that interaction with secondary flows is inevitable. To minimize the effects of secondary flows when operating in transport mode, systems with high Ekman numbers should be used. In addition, higher purity fractions in the outer outlet may result from operating the system in parallel mode. When operating in equilibrium mode, a modified outlet splitter can enhance the separation by forcing low-density particles in the vortex to the inner outlet, while collecting the high-density particles concentrated a short distance from the end wall in the outer outlet.

3.7 References

[1] Giddings, J.C., *Sep. Sci.*, **1**, 123 (1966).

[2] Giddings, J.C., *Science*, **260**(5113), 1456-1465 (1993).

[3] Giddings, J.C.. *Anal. Chem.*, **53**(11); 1170A-1178A. (1981).

[4] Fuh C.B., *Anal. Chem.*, **72**(7), 266A-271A, (2000).

[5] Giddings, J.C., Yang, J.F., Myers, M.N., *Anal. Chem.*, **46**(13), 1917-1924 (1974).

[6] Fuh, C.B., Myers, M.N., Giddings, J.C., *Ind. Eng. Chem. Res.*, **33**, 355-362, (1994).

[7] Fuh, C.B., Giddings, J.C., *Biotechnol. Prog.*, **11**, 14-20 (1995).

[8] Camerani M.C., Steenari B.M., Sharma R., Beckett R., *Fuel*, **81**(13), 1739-1753 (2002)

[9] Crossan A.N., Lee N., Sharma R., Kennedy I.R., Beckett R., *Anal. Chim. Acta*, **468**(2), 199-208 (2002)

[10] Dean, W.R., *Phil. Mag.*, **V**, 673-695 (1928).

[11] Ishigaki, H., *J. Fluid Mech.*, **329**, 373-388, (1996).

[12] Zhang, J., Zhang, B., Jü, J., *Int. J. Heat Fluid Flow*, **22**, 583-592, (2001).

[13] Schure, M.R., Weeratunga, S.K., *Anal. Chem.*, **63**, 2614-2626, (1991).

[14] Gupta, S., Ligrani, P.M., Myers, M.N., Giddings, C., *J. Microcolumn Sep.*, **9**(3), 213-223 (1997).

Chapter 4: Separation of Mixed Color Toner Waste using Centrifugal SPLITT Operating in Equilibrium Mode

4.1 Introduction

Mixed color toner waste results from most full color xerographic processes. An inherent problem with the xerographic process is that the transfer efficiency of toner from the photoreceptor to the paper is less than 100%. This requires that the photoreceptor be cleaned after each copy is made [1]. The toner that is cleaned from the photoreceptor is collected in a single waste bin. The four colors that go into making a color copy are thus mixed in the bin based on the use of the individual colors by the machine. Previous work done by our research group showed significant environmental gains could be realized by recycling waste toner [2]. A life-cycle assessment (LCA) was performed on black toner in a single component copier. The modeled system included raw material manufacturing, toner manufacturing, customer use, and end of use processes. Within the system, toner from the waste sump in the customer's machine is screened and mixed directly with raw materials at the front end of the toner manufacturing process. The LCA results showed a 29% reduction in virgin material use and a 24% reduction of solid waste production over the life-cycle when the waste toner is recycled.

The gains realized by the recycling of black toner cannot be maintained with color xerographic devices unless a reasonable separation technique can be developed. This chapter investigates the use of split-flow thin-celled (SPLITT) fractionation as a method for separating toner particles. SPLITT fractionation is an analytical technique invented

by J.C. Giddings [3]. This particle separation technique uses thin flow cells with a rectangular cross section and a large aspect ratio. An external field is applied across the thin dimension of the channel and perpendicular to the primary direction of flow. Channels with a high aspect ratio are used to minimize end effects on the flow profile. The interaction of the particles with the carrier fluid and the external field determine the particle position within the system. At the outlet of the flow cell, the carrier fluid is split into two fractions. Particles are separated based on their position relative to the outlet splitter in the channel.

SPLITT fractionation (SF) systems can be operated in one of two modes: equilibrium mode and transport mode [4]. In the transport mode of operation, particles near the inlet of the separation channel are concentrated against one wall of the flow cell. The external field directs all particles towards the opposite wall while the primary flow carries the particles through the system. The rate of transport of the particles towards the opposite wall determines the particle position relative to the outlet splitter. In the equilibrium mode of operation, the particles are dispersed across the flow cell at the inlet of the separation channel. While the primary flow in the flow cell transports the particles through the system, the particles are driven towards one wall or the other based on their interaction with the external field and the carrier solution. At the outlet, the particles are again split based on their relative positions within the channel.

SF is related to the family of field flow fractionation (FFF) techniques in its use of thin channels with a viscous carrier fluid under laminar flow and an external field applied

across the thin dimension of the channel [5]. The main feature distinguishing SF from FFF is the plane in which the separation occurs. While SF separates particles based on their location across a channel, FFF separates particles based on their transport rate through the channel in the direction of primary flow. This restricts the operation of FFF to a batch mode. The small sample size and batch mode of operation were identified early on in the development of FFF as disadvantages to the scale-up of the technique [6]. One of the motivations for the development of SF was to develop a separation system which would overcome these limitations.

In theory, a variety of external fields can be used to drive the separation, including magnetic, electric, gravitational, and centrifugal. In practice, gravitational SF has been the most widely developed technique, with the main application being the separation of oversized particles in a sample. Gravitational SF has been applied to samples such as starch granules [7], lagoon sediments [8], environmental particulates [9], and biological cells [10]. Electrical and magnetic SF equipment has been built and demonstrated, but the technology is not as developed as gravitational SF [11, 12]. Centrifugal fields in SF have been used in biological applications [13] as well as colloidal particles [14] and biomass fly ash particles [15]. With a few exceptions, nearly all of the separations are run using the transport mode of SF.

Particle sedimentation is used by both gravitational and centrifugal SF. The use of centrifugal fields allows SF to be applied to the separation of particles that are not well suited to gravitational SF [14]. Brownian motion in particles smaller than 1 micron

degrades the separation powers of gravitational SF. For particles with densities close to the carrier fluid, rapid separation of the particles in a gravitational field is not possible. Increasing the magnitude of the field is not an option in gravitational SF, thus centrifugal fields are required for these particles. For centrifugal SF, the separation channel is wrapped around the axis of a centrifuge. The carrier fluid transports particles in the angular direction, and particle separation occurs across the channel thickness in the radial direction. The strength of the field is dependent on the speed of rotation and the radial distance of the channel from the axis of rotation.

The presence of secondary flows in sedimentation FFF (SdFFF) was examined numerically by Schure, et al. [16]. The motion of a fluid relative to a rotating reference frame induces a force perpendicular to both the fluid motion and the axis of rotation, called the Coriolis force. Coriolis induced secondary flows are present in both SdFFF and centrifugal SF separation channels. These secondary flows can be minimized through the use of very thin channels and slower rotation rates, but secondary flows are present in all rotating flow channels. In Chapter 3, numerical modeling was used to examine the development of secondary flows in SdFFF and centrifugal SF channels and discussed their effects on the separations. The findings reinforced the conclusion of Schure that for effective operation of SdFFF, the rotation and flow should be in opposing directions. It was also determined that some deterioration of the separation due to the secondary flows will be present with centrifugal SF operating in the transport mode. For centrifugal SF operating in equilibrium mode, where the equilibrium positions are the

opposing walls of the flow channel, the use of an asymmetric splitter was suggested as a way to compensate for the effects of the secondary flows on the particles.

As a first step in achieving the larger problem of separation of mixed color toner waste, this paper will focus on the separation of two toner particles using centrifugal SF operating in equilibrium mode. This separation technique uses density differences as the sole distinguishing factor for the separation of particles. Density differences in toner particles should have very little effect on the performance of toner in xerographic machines. The performance of the system was tested with a single toner, and a binary separation of two toner sets was performed. The concept of an asymmetric splitter in a centrifugal SF device operating in equilibrium mode is also examined.

4.2 Mechanism and Theory

The mechanism of centrifugal SF operating in equilibrium mode (CSF-Eq) is illustrated in Figure 4.1. Particles, which are initially well dispersed, are transported through the rotating channel by the carrier fluid under laminar flow conditions. While moving through the channel, the particles are subject to the centrifugal forces associated with a body in rotation. The resulting balance of forces on the particles causes the particles to be separated according to their density relative to the carrier fluid density. Particles that are more dense than the carrier fluid will be transported towards the outer wall, while particles that are less dense than the carrier fluid will be transported towards the inner wall. As the particles approach the outlet splitter, the particles are sorted according to their radial position in the channel, thus particles less dense than the carrier fluid will be

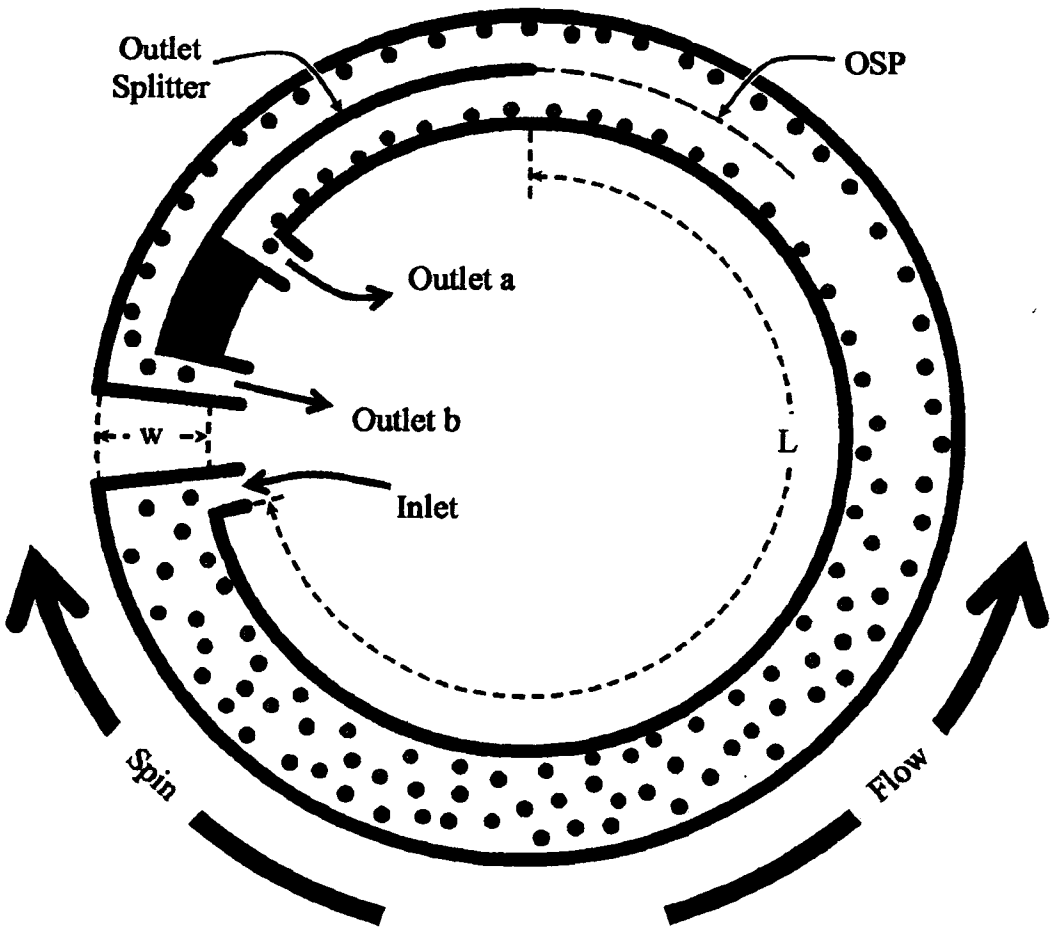

Figure 4.1. Schematic diagram of a CSF-Eq channel for binary separation. The separation is based purely on density differences between the two particles and the carrier fluid, with particles less dense than the fluid eluting from Outlet a, and particles more dense than the fluid eluting from Outlet b.

collected in outlet a, and particles more dense than the carrier fluid will be collected in outlet b.

An outlet splitting plane (OSP) can be defined upstream from the outlet splitter based on the relative flow rate of the two outlets. Any particle between the OSP and the outer wall will elute from outlet b, while any particle between the OSP and the inner wall will elute from outlet a. For a complete separation, the particle with the slowest settling velocity must be transported from the wall opposite of its accumulating wall to beyond the OSP. For example, to recover all of the less dense particles in outlet a, the smallest particle with a density closest to the carrier fluid must be transferred from a position along the outer wall near the inlet to a radial position inside of the OSP at the outlet splitter. The governing factors in the separation are the carrier fluid flow rate and the particle settling velocity. The relation between these two factors in CSF-Eq can be taken from the equation derived for SF operating in transport mode [17]:

$$\Delta\dot{V} = bLU \tag{1}$$

where b is the channel breadth, L is the channel length, U is the settling velocity of the particle, and $\Delta\dot{V}$ is the volumetric flow rate of the lamina traversed by the particle. Therefore, to ensure that all of the less dense particles are recovered in outlet a, the flow rate in outlet b must be less than $\Delta\dot{V}$ calculated for the smallest less dense particle. A similar calculation for particles more dense than the carrier fluid will show the maximum flow rate for outlet a. The settling velocity of a spherical particle in a centrifuge is derived from Stokes Law:

$$U = \frac{R\Omega^2 \Delta\rho}{18\mu} d_p^2 \tag{2}$$

where U is the particle settling velocity, R is the radial distance from the axis of rotation, Ω is the rotation rate, $\Delta\rho$ is the density difference between the particle and the carrier fluid, d_p is the diameter of the particle, and μ is the viscosity of the carrier fluid. In the ideal case of a binary mixture of particles with the only difference being the density of the particles, the carrier fluid can be formulated so that $\Delta\rho$ for the two particles is equal in magnitude and opposite in sign. This would result in a maximum inlet flow rate of $2\Delta\dot{V}$, with each outlet having a flow rate equal to $\Delta\dot{V}$. Flow rates higher than this calculated value would not allow for all of the particles to be transported beyond the OSP before the outlet splitter is encountered.

The calculations above are based on the assumption that ideal flow conditions are present, where velocity is a function only of radial position within the channel. However, the previous chapter has shown that secondary flows are a significant factor in centrifugal SF. The secondary flows manifest as vortices at the axial end walls of the flow channel. The presence of secondary flows in centrifugal SF will cause the position of the particles to be disturbed, thus deteriorating the separation. For an efficient high resolution particle separation, the system must be able to account for the effects of the secondary flow on particle trajectories. The extent to which secondary flows are present in the flow channels is governed by the Ekman number:

$$N_{Ek} = \frac{\nu}{w^2 \Omega} \tag{3}$$

where ν is the kinematic viscosity, and w is the channel thickness. Three regimes were identified in Chapter 3. For $N_{Ek} > 0.05$ the secondary flows are isolated at the end walls as elliptical vortices and do not extend beyond two channel widths from each end wall. For $N_{Ek} < 0.009$ the secondary flows take on a rectangular shape and extend well into the bulk of the channel. A transitional regime is present between these two regimes, where the elliptical vortices open up into the rectangular flow pattern. The most effective way to minimize the secondary flows in a rotating channel is to minimize the channel thickness. Thus, for centrifugal SF, thin channels are desirable.

Even with thin channels, however, secondary flows are present. Their effect on the particles in CSF-Eq was also discussed in Chapter 3. In systems with rotation in the direction opposite to the primary flow, as shown in Figure 4.1, the vortices are oriented so that the radial flow at the end walls is directed towards the axis of rotation. The effect on the particles is such that particles more dense than the carrier fluid are forced away from the end walls, while particles less dense than the carrier fluid are forced into the vortices, as shown in Figure 4.2. The result is three regions of particle concentration in the channels: more dense particles against the outer wall in the bulk of the channel, less dense particles against the inner wall in the bulk of the channel, and less dense particles entrained in the vortices near the two end walls. A symmetrical outlet splitter traditionally used in SF would result in an elevated concentration of the less dense particles in outlet b, thus reducing the purity of the separation. The use of an asymmetrical outlet splitter, where the outlet along the outer wall is blocked near the end

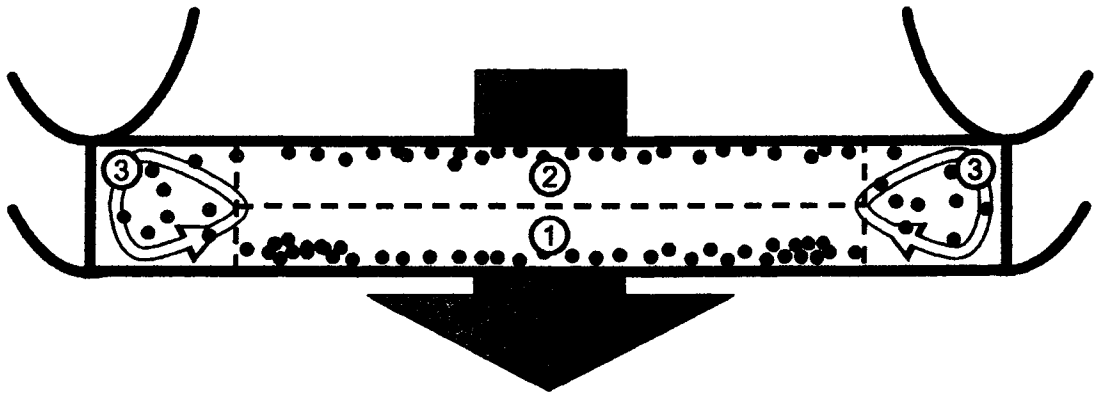

Figure 4.2. Effects of secondary flows on particles in the separation channel. The three regions of particle concentration are (1) particles more dense than the carrier fluid along the outer wall in the bulk, (2) particles less dense than the carrier fluid along the inner wall in the bulk, and (3) less dense particles trapped in the vortices near each end wall.

walls, will enhance the separation by inhibiting the less dense particles in the vortices from entering outlet b.

4.3 Experimental Section

Construction of the separation channel was achieved using three thin strips sandwiched between two stainless steel cylinders. The overall design of the rotor used in the experiments is shown in Figure 4.3. An expansion ring was used to expand the inner ring into the outer ring, thus compressing the three layers against one another. The channel is defined by the outer wall of the inner cylinder, the inner wall of the outer cylinder, and the cuts made in the three middle layers. The middle layers are comprised of a center layer of stainless steel with a layer of Mylar on each side, as shown in Figure 4.3. The steel layer was used as the outlet splitter in the system. The thickness of the steel layer was 381 μm, while the thickness of each Mylar layer was 356 μm. A small bead of silicone sealant (Permatex, part #81158, Hartford, Conn.) was used to ensure that the system did not leak, thus the assembled channel has a maximum thickness of approximately 1.2 mm.

The rotor described above was designed for use in a Thermo IEC Centra GP8 centrifuge (Fisher Scientific, Pittsburgh, PA). The performance of the GP8 centrifuge allows speeds to be set from 500 to 5300 RPM in 10 RPM increments. The large capacity centrifuge provides ample space for the rotor. The other key component of the centrifugal SF device is a rotating union, which allows fluid to flow into and out of the rotating centrifuge. The system used a four-port HSMC series high-speed rotary union, model

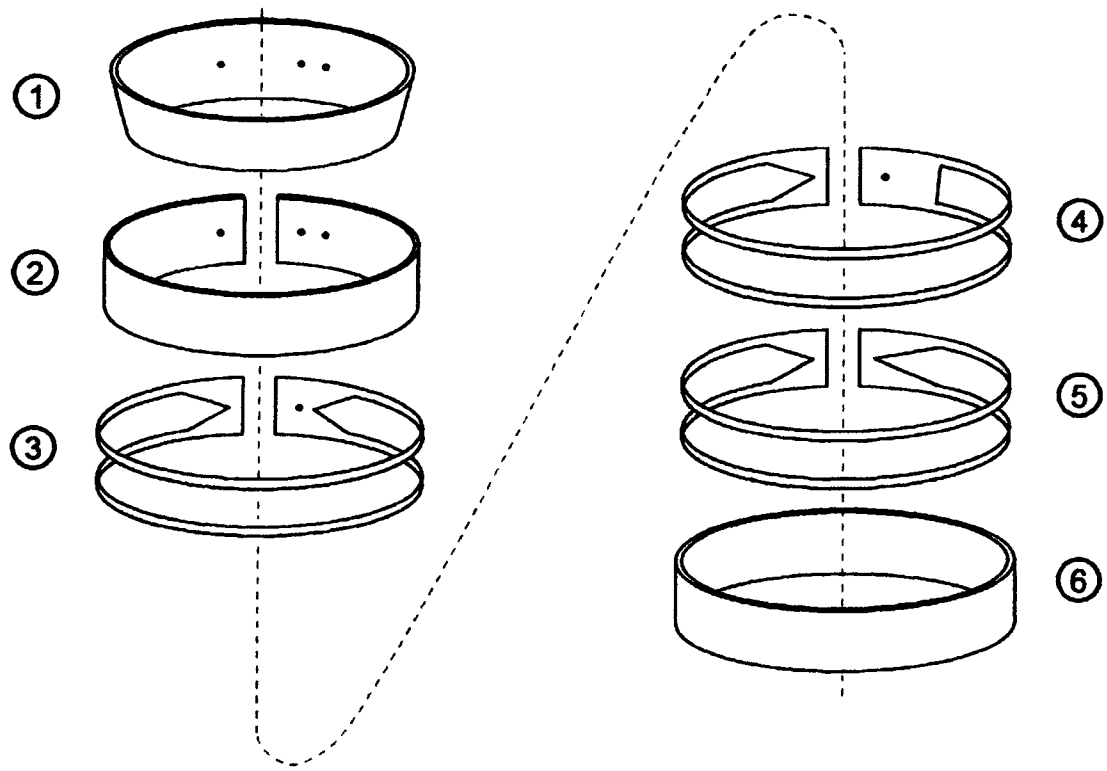

Figure 4.3. The layers of the channel design: (1) aluminum expansion ring, (2) stainless steel inner cylinder, (3) inner Mylar strip, (4) stainless steel splitter strip, (5) outer Mylar strip, (6) stainless steel outer cylinder.

#750810 (Duff Norton, Charlotte, NC). The specifications on this union allow for speeds up to 3000 RPM and pressures of up to 17 bar. Only three of the four ports were employed by the system, which is acceptable with the design of the union as all four ports are individually sealed.

The toner used in the analysis of the performance of the system was Royal Blue Toner, part #6R826 (Xerox, Stamford, CT). This toner uses a polystyrene/butadiene resin with small amounts of blue and magenta pigment (<5%). The density of this toner was measured experimentally using known solutions to test the settling direction. The density was determined to be 1,055 ± 2 kg/m^3. The volume weighted median particle size is 8.0 μm with a log normal distribution from 5-12 μm, as measured by Xerox Corp using a Coulter Counter. For the two-component separation process, two custom toners were produced. A polyester based resin was used for these toners. For the lower density toner, cyan pigment was added to the resin. The higher density toner used carbon black as the base pigment and a small amount of magnetite was added to increase the density of the particles. The density of the cyan toner measured experimentally was 1,249 ± 3 kg/m^3, while the black toner density was measured at 1,280 ± 5 kg/m^3, again using known solutions. The particle size and distribution of the black and cyan toner was approximately equal to that of the royal blue toner. Both the royal blue toner and the cyan and black toners were manufactured using a conventional pulverization process.

The carrier fluid was an aqueous based solution of a density modifying agent and surfactant. For the royal blue test particles, sucrose (Fisher Scientific, Pittsburgh, PA)

was used to modify the density of the carrier fluid. The higher density of the cyan and black test particles required the use of cesium chloride (Fisher Scientific, Pittsburgh, PA) as the density modifying agent. Both sucrose and CsCl are commonly used in density gradient centrifugation, and the performance of their solutions is well documented [18]. The surfactant used in the carrier fluid was 0.50% (v/v) Triton X-100 (Fisher Scientific, Pittsburgh, PA).

A Masterflex multi-channel cartridge pump head, model #07519-10 (head) and #SY-07519-10 (cartridges), was coupled with a Masterflex variable speed console drive with 10-turn speed control, model #7521-50, to drive the fluid through the system (Cole-Parmer, Vernon Hills, IL). The offset occlusion of the cartridges aided in reducing the pulsation associated with peristaltic pumps. A pulse dampener was used to further reduce any residual pulsation. Three Gilmont Accucal flow meters were used to monitor the inlet and outlet flow rates. The variable area flow meters were adjusted for density and viscosity changes associated with the different carrier fluids. The temperature and pressure of the carrier fluid was monitored at the inlet and both outlets. All experiments were performed at ambient conditions. Friction in the rotary union did increase solution temperature under higher rotation rates, but the effluent temperature rarely exceeded 30C. The main impact of such temperature changes was seen in an increase in the viscosity of the carrier fluid. Viscosity changes associated with the temperature changes were automatically accounted for in the flowrate calculations. Density was less affected by the temperature changes and was predicted to have minimal impact on the separations.

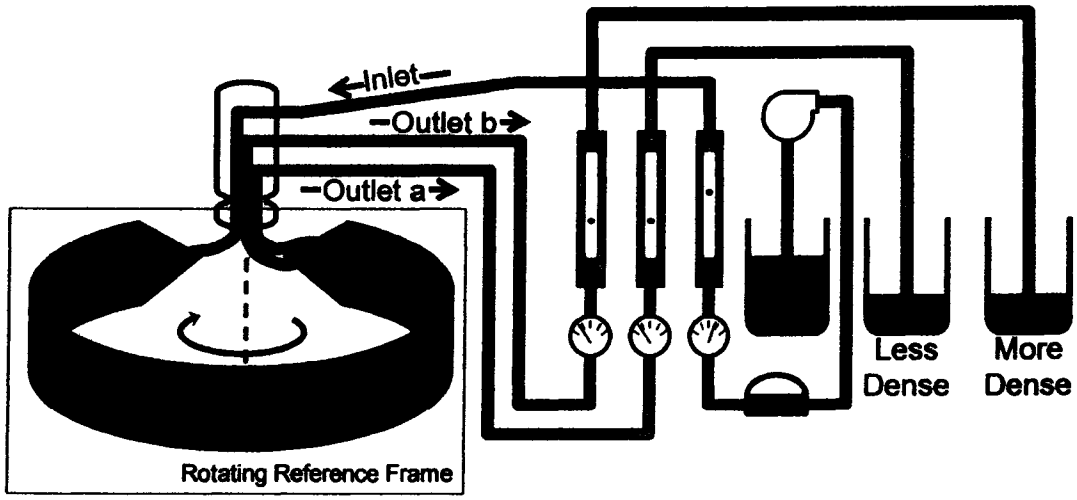

Figure 4.4. Diagram of CSF-Eq system used in the experiments. Fluid from the inlet reservoir is pumped through a pulse dampener, which eliminates pulsation in the flow. The inlet and outlet pressure and flow rate are monitored continuously, and the two effluent fractions are collected separately.

The set-up of the system is illustrated in Figure 4.4. For all experiments in this paper, the system was initially run closed with no rotation, where the system outlet streams returned the effluent to the inlet reservoir. The system was flushed at elevated flow rates (100+ mL/min) until the outlet and inlet streams had equal particle concentrations, as determined visually. The flow rate was then set to the experimental flow rate. Once the flow rate was steady, the system was opened and rotation was initiated. The centrifuge reached the set speed in less than one minute, and the system was allowed to come to steady state, as described previously. Once the samples were taken from the outlet streams, rotation was stopped, the recovered effluent in the outlet reservoirs was returned to the inlet reservoir, and the system was again closed and flushed. This procedure allowed multiple trials to be performed with the same particle solution.

For the analysis of the experimental results, three methods were employed. First, the system was monitored visually while the system was in operation. The intensity of the color of the toner particles suspended in the carrier fluid was a very good indicator of the particle concentration. For the single component system, the known inlet concentration was used as a baseline. The outlet particle concentrations were then monitored until the system reached steady state, usually from 2-10 minutes from start-up, depending on the system configuration. For a system with 100% separation and equal outlet flow rates, one outlet would be free of particles, while the other outlet would have twice the particle concentration as the inlet. In the binary separations, steady state could still be monitored, though not with the precision of the single component experiments. Once it was

determined visually that steady state had been achieved, the system was allowed to run for an extra 5-10 minutes before samples were collected.

Discrete samples were collected from both the outlet streams and analyzed offline. The single component samples were analyzed using a Hach 2100N Turbidimeter. A calibration curve for the particles in different sucrose solutions was constructed so that the turbidity result could be related directly to the particle concentration of the sample. The turbidity measurements had some degree of variability in their results, most likely due to movement of the particles during the measurements. This variability was generally on the order of 4%, which is reflected in the results. For very high degrees of separation, this variability had a smaller effect on the results than for experiments with poorer separations.

For the binary separations, optical microscopy was used to analyze the samples. Using an Olympus BX51 microscope with a color wheel filter, two images were taken of the sample. The first image used a blue filter from the color wheel, which allowed only the black particles to appear in the recorded image. The second image used a red filter from the color wheel, which revealed both the cyan and black particles equally in the recorded image. Both images were taken in less than one second to ensure that the same area of the sample was recorded in both images. The images were then analyzed using MetaMorph software (Molecular Devices, Sunnyvale, CA), which recorded the pixel area of each particle in the image. This data was used to calculate the total volume of each particle in the image. Over 100 images of each sample were taken, with an average

particle count of approximately 100 particles per image. The total calculated volume from the "black only" (blue filter) images and the total calculated volume from the combined (red filter) images could then be used to calculate the volumetric ratio of the cyan to black particles in the sample, indicating the purity of each fraction. A simple balance around the system was used to convert the calculated ratio into the percent recovery of each toner in each fraction.

4.4 Results and Discussion

4.4.1 Single Component Performance Tests

In order to test the performance of the system, the royal blue toner was run as a single component in the system. Various channel designs were explored using different cuts in the three layers. Initial experiments showed that the system had difficulty achieving steady state when run with the channel at maximum thickness for the entire length of the channel. This is possibly a result of the irregular shape of the toner particles. A force balance on a particle near a wall is shown in Figure 4.5 for a spherical particle and a toner particle. Conceptually it can be seen that to initiate removal of the particle by either a sliding or rolling mechanism, much less drag force would be required on the spherical particle than on the irregular toner particle. Numerous studies concerning particle detachment mechanisms have been reported in the literature [19]. The specific mechanism of removal for toner particles near the wall in the CSF-Eq system is beyond the scope of this work. However, it was determined experimentally that to avoid particle adhesion in the system, which would prohibit the system from achieving steady state, a

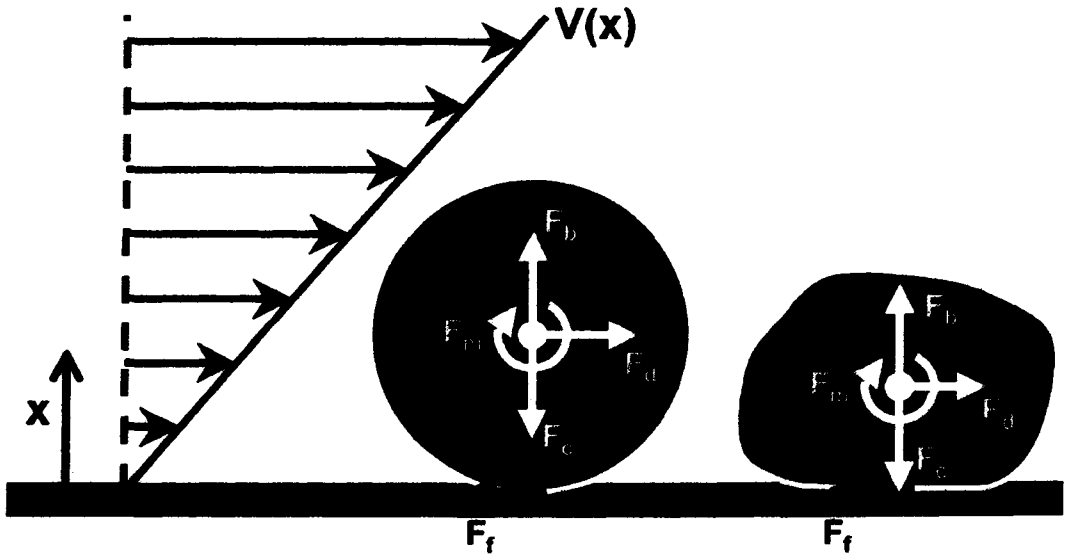

Figure 4.5. Force balance for particles near the outer wall. Particle removal by sliding or rolling is much easier for the spherical particle (left) than for the toner particle (right). The forces on the particle are buoyancy (F_b), centrifugal (F_c), drag (F_d), frictional (F_f), and rotational (F_m).

minimum ratio of the viscous drag force to the centrifugal force on a representative particle at the wall was required. Using a spherical particle with a diameter of 6 mm, a minimum ratio of 40 was needed for the system to operate as desired. The resulting equation was then used to calculate the minimum flow rate required in the system:

$$\dot{V}_{\min} = \frac{40 d_p \Delta\rho w^2 b R \Omega^2}{54 f \mu} \tag{4}$$

where f is a dimensionless coefficient (=1.7009) used as a correction factor for the wall effect given by O'Neill [20]. Equation 4 shows that thinner channels reduce the required minimum flow rate in the system. Combined with Equations 1 and 2 for calculating the maximum flow rate, a range of allowable flow rates could be calculated for each separation system. Based on this result, the final design of the channel used the inner Mylar layer to define the channel thickness through most of the channel, with the steel and outer Mylar layers cut so that the system opens up to the full channel thickness just before the outlet splitter fractionates the fluid, as shown in Figure 4.6. Thus, the separation channel has a thickness of 0.42 mm for the majority of the channel length, and then opens up to 1.2 mm at a distance of 1.2 cm from the outlet splitter. The other dimensions used in the original system are, and $b_1 = b_2 = 4cm$, which corresponds to a symmetric outlet splitter design. The radius of rotation of the separation channel, R, is $14.5cm$ for all experiments.

The performance of this channel design was tested with the royal blue toner at various rotation rates. A carrier fluid density of 1,043 kg/m^3 was used to test the separability of particles more dense than the carrier fluid. A flow rate of 40 mL/min and an inlet particle

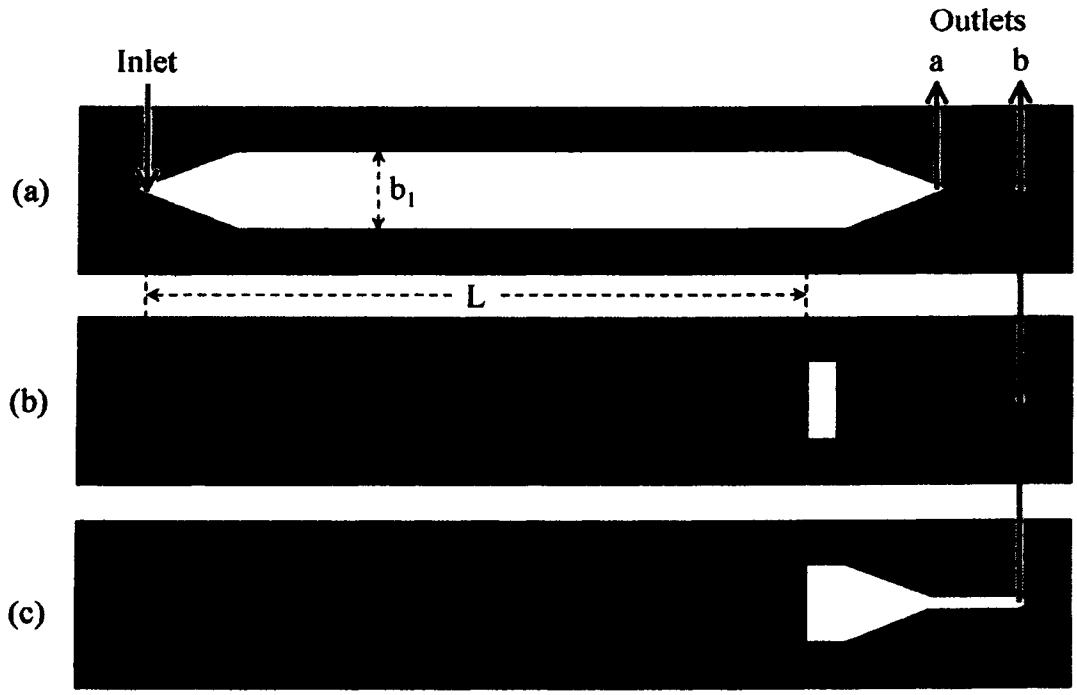

Figure 4.6. Design of layers used in the system: (a.) inner Mylar strip, (b.) stainless steel splitter strip, and (c.) outer Mylar strip. The main channel is defined by the cut in the inner strip, b_1. The dimensions at the outlet splitter are defined by the width of the cut in the splitter and outer strips, b_2. The drawing is not to scale.

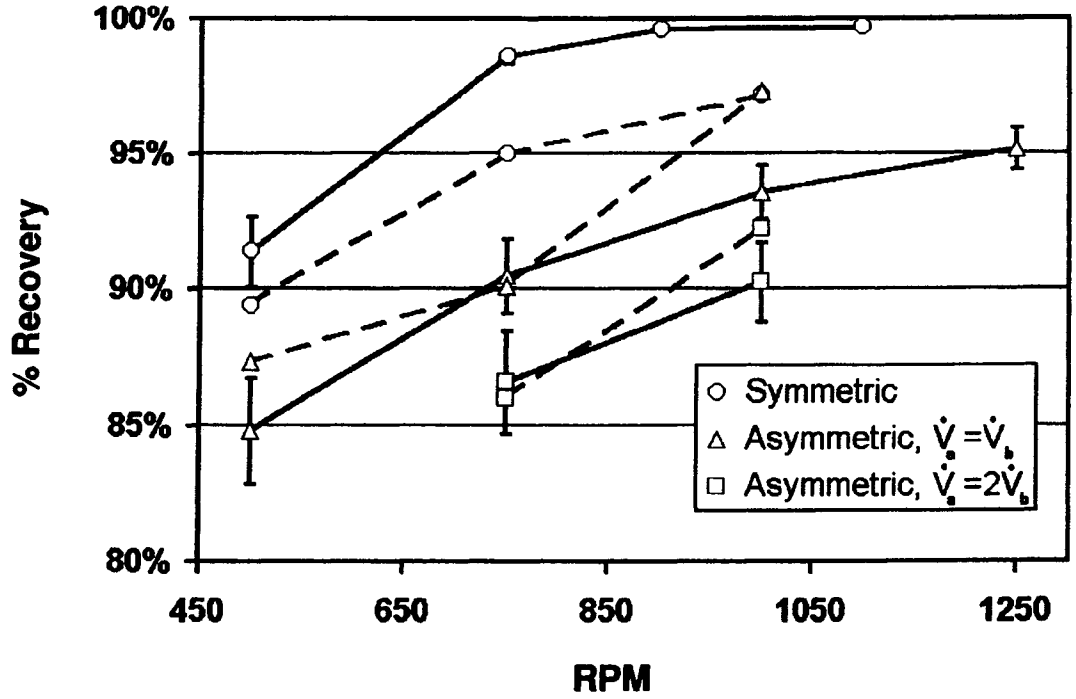

Figure 4.7. Plot of recovery percentage vs RPM for particles more dense than the carrier fluid recovered in outlet b for three systems. Solid lines represent single component results, and dashed lines represent two component separation results. Recovery percentage is the mass of more dense particles recovered in outlet b divided by the total mass of more dense particles fed to the system.

concentration of 0.20% (v/v) was used for all of the experiments. This flow rate was just above the maximum flow rate calculated from Equations 1 and 2 for 500 RPM, but was within the limits for all of the other rotation rates tested. The percentage of particles recovered in outlet b is shown in Figure 4.7 for the symmetric outlet splitter. This plot shows that over 90% of the particles exited with the more dense fraction for all of the rotation rates tested. The general trend shows that higher rotation rates increase the fractionating power of the more dense particles. As expected, the lowest resolution was for the slowest rotation, and the resolution increased to more than 99% at higher rotation.

To test the separability of particles less dense than the carrier fluid, the carrier density was adjusted to 1,070 kg/m^3. This density was chosen so that the settling velocity of the toner in this system would be equivalent in magnitude to the previous experiment. A slight increase in the viscosity is associated with the higher sucrose concentration. The system was again tested at various rotation rates at a flow rate of 40 mL/min. Figure 4.8 shows the percentage of particles recovered in outlet a. The recovery of the less dense particles was greatly decreased as compared to the recovery of the more dense particles in the previous experiment. This results from secondary flows in the system, described previously. In the bulk of the channel, the secondary flows are isolated near the end walls due to the relatively high Ekman numbers. When the channel thickness is expanded just before the outlet splitter, however, the secondary flows enter the transitional regime. The increased influence of the secondary flows on the system is especially seen in the higher rotation speeds, where resolution decreases even as the main driving force for the separation (centrifugal force) is increased as the square of the

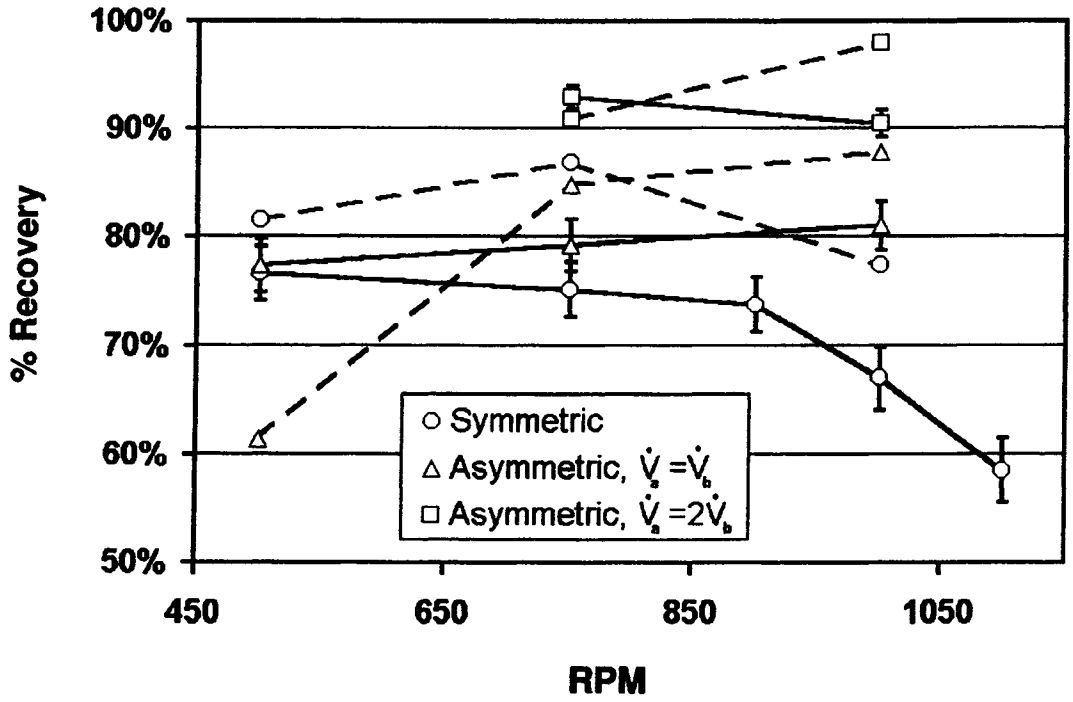

Figure 4.8. Plot of recovery percentage vs. RPM for particles less dense than the carrier fluid recovered in outlet a for three systems. Solid lines represent single component results, and dashed lines represent two component separation results. Recovery percentage is the mass of less dense particles recovered in outlet a divided by the total mass of less dense particles fed to the system.

rotation rate. This is directly related to the expansion of secondary flows away from the end walls for increasing rotation in the transitional regime. The more dense particle separation results showed very little influence of the secondary flows on the separation, as expected.

To resolve the secondary flows in the CSF-Eq device, an asymmetric outlet splitter was employed. From the earlier discussion on the regions of particle concentration in the separation channel, reducing the breadth of the outer particle outlet at the outlet splitter will allow more dense particles concentrated in the center of the channel to be collected while less dense particles in the vortices near the end walls will be excluded from the more dense fraction. For this system, the same dimensions for the channel were used with the exception of the breadth of the splitter layer and outer Mylar layer, labeled as b_2 in Figure 4.6. This dimension was set to $2cm$, centered on the channel. The resulting system allows the less dense particles trapped in the vortices near the end walls to avoid entering the more dense fraction. Particles more dense than the carrier fluid, which are forced away from the end walls by the secondary flows, are still collected in outlet b. Thus, the three regions identified in Figure 4.2 will be collected in their corresponding outlets.

The asymmetric splitter system was again tested with royal blue toner at carrier densities of 1,043 and 1,070 kg/m^3 and a flow rate of 40 mL/min at various rotation rates. The system was initially run with equal flow rates for the two outlet streams ($\dot{V}_a = \dot{V}_b$). This resulted in a slight increase in the resolution of the system for the less dense particles, as

shown in Figure 4.8 for "asymmetric, $\dot{V}_a = \dot{V}_b$". Most importantly, a decrease in this resolution at higher rotation rates was not seen. Figure 4.7 shows that the resolution of particles more dense than the carrier stream, however, was hindered. At low rotation rates, the secondary flows do not extend far enough from the walls to force all of the more dense particles into outlet b. As the rotation is increased, the secondary flows extend further from the walls and an increase in the percent of recovery of more dense particles in outlet b results.

The increase in the resolution of the less dense particles was less than expected for the asymmetric outlet. This can be attributed to the position of the OSP. In the bulk of the channel, for equal volumetric flow rates in the two outlets, the average velocity of the fluid entering outlet b below the outlet splitter is approximately double the velocity of the fluid entering outlet a. This yields a shift in the OSP towards the inner wall, and thus some of less dense particles that did not reach the inner wall would be collected with the more dense fraction. To adjust for this shift, the system was run with equal average velocities in the two outlets at the outlet splitter ($\dot{V}_a = 2\dot{V}_b$). Operating the system under these flow parameters showed a large increase in the resolution of the less dense fraction, as shown in Figure 4.8 for "asymmetric, $\dot{V}_a = 2\dot{V}_b$". Figure 4.7 shows an associated decrease in the resolution of more dense particles, but the system was still achieving approximately 90% recovery.

4.4.2 Separation of Two Toner Particles

The above experiments show the potential for asymmetric outlet splitters to increase the performance in CSF-Eq. To test the system in a binary separation process, cyan and black toners were run for the three systems described above. A 28.07-wt% CsCl solution was used in all of the binary separations. This solution has a density of 1,264 kg/m^3 at 23C and 1,260 kg/m^3 at 30C, which are the extremes in temperature during the trials. Thus, the driving force for the two toners are roughly equivalent in the separation channel. The overall flow rate was again set to 40 mL/min, and the particle concentration for each toner was 0.20-vol%. The recovery percentages of each toner in its correct fraction are reported in Figures 4.7 and 4.8. For the black particles, plotted in Figure 4.7, the recovery percentage in the more dense fraction again remained quite high. The general trend of increased particle recovery with increasing rotation rates was again achieved for all three systems. The effect of a decrease in recovery with the use of the asymmetric splitter was also seen.

Figure 4.8 shows the recovery percentages for the cyan particles in the less dense fraction. The symmetric system showed the expected decrease in recovery at high rotation rates, as the secondary flows become more prominent in the system. For the asymmetric splitter with equal flow rates in the outlets, increased rotation rates resulted in a higher recovery. The low recovery at 500 RPM for this system is most likely the result of particle aggregation in the system. The polyester based particles seemed to have a much higher tendency to aggregate than the polystyrene/butadiene based particles used in the single component experiments. The most likely cause is the magnetite in the black

toner. Though present in a small percentage (3.0-wt%), an elevated rate of aggregation was seen in the black particles. This problem was minimized by increasing the agitation in the system between runs. For a rotation speed of 500 RPM for the asymmetric system, however, the driving force (40g at 500 RPM vs 91g at 750 RPM) seemed to be too low to break up the aggregates. The black toner seemed to capture some cyan particles during aggregation, thus the low recovery for the cyan particles while the black recovery remained high. The recovery rates of the cyan particles at higher rotation rates for the asymmetric splitter showed the expected trends, with increased recovery rates seen in both equal flow and equal velocity systems.

The goal of this separation system is to produce two highly pure effluent streams. Figure 4.9 shows the purity of the two recovered fractions for the three systems run at 750 and 1000 RPM. The effects of the secondary flows and asymmetric splitter on the effluent purity are clearly shown. For the two symmetric systems, Figure 4.9a, the purity of the cyan toner in the less dense stream is enhanced under increased rotation, as the black toner is aided by the increased driving force. For the black toner in the more dense fraction, however, the increase in the associated secondary flows under increased rotation results in a decrease in the purity as more cyan particles are forced into the more dense fraction.

The effects of the asymmetric splitter on hindering the recovery of the black toner in the more dense fraction is seen in both rotation rates. This decrease in the cyan toner purity is most prominent at 750 RPM, where the secondary flows don't extend far enough from

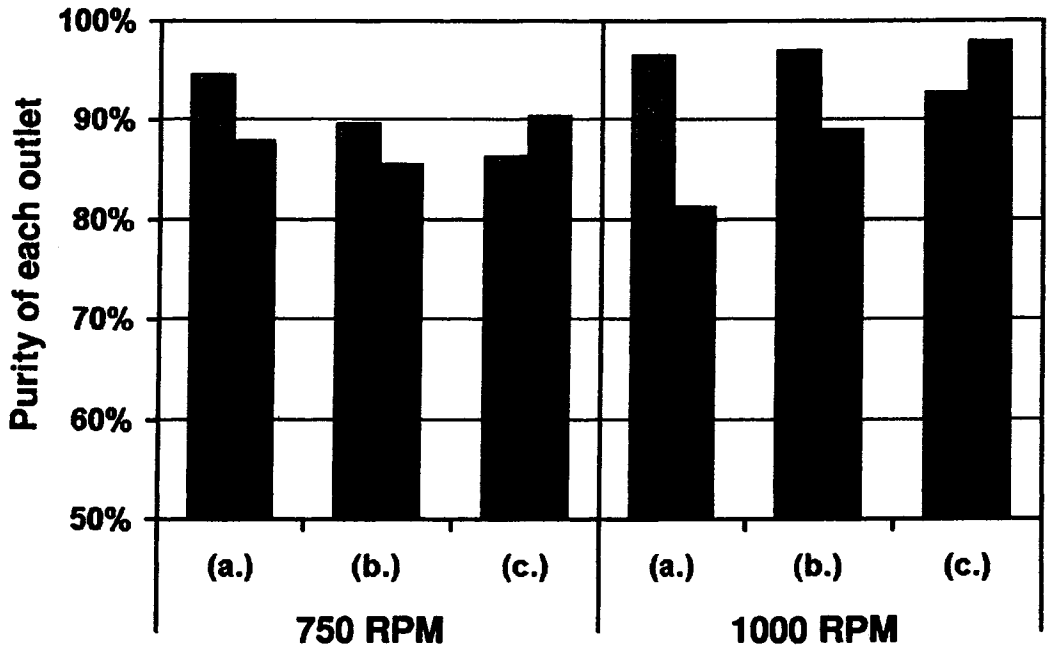

Figure 4.9. Purity of each outlet stream for different systems. For each rotation rate, the systems tested are (a.) symmetric outlet, (b.) asymmetric outlet with equal flow rates in outlets a and b, and (c.) asymmetric outlet with equal face velocities at the splitter in the bulk for outlets a and b. Purity is calculated as the mass concentration of the desired particle in an outlet stream divided by the total mass concentration of both particles in the outlet stream. The dark bars are for the more dense fraction recovered in outlet b, and the light bars are for the less dense fraction recovered in outlet a.

the end walls to push the black toner into the more dense fraction. The increased purity of the more dense fraction through the use of the asymmetric splitter is shown especially well in the 1,000 RPM results. At this rotation rate, the symmetric splitter gave no protection to the more dense fraction from the cyan particles trapped in the vortices near the end walls. The asymmetric splitter, however, encouraged the particles near the end wall to exit through the less dense fraction. This resulted in very high purity of the more dense fraction, especially for the experiments run with equal velocity in the two outlets at the outlet splitter.

The above study shows the improvement in performance of a CSF-Eq device with the use of an asymmetrical splitter. The system was not optimized, but the large improvements in the separation of the less dense fraction verify the numerical model results discussed previously. System variables that directly affect the development of the secondary flows and could be studied for further improvements in the system performance are the rotation rate, the flow rate, and the channel thickness. Adjustments to the breadth of the more dense outlet at the outlet splitter could also aid in improving the separation.

For the two-component separation, the purity of the outlet streams ranged from 81-97%. Further purification could result by repeating the separation on the effluent streams. This could increase the purity of a 90% separation to 99% after only two cycles. Similar coupled separation procedures could be used to zone in on a specific density fraction of the sample. Adjusting the carrier fluid density between runs would allow the recovery of

particles between the two densities used. This would expand the use of the system beyond a two component separation to more complex particle samples.

The four colored toners used in full color documentation could be engineered to have four specific densities. By first fractionating the particles using a carrier fluid density such that two of the four toners are collected in each outlet, then fractionating the resulting two component systems, complete separation of mixed color toner waste could be achieved. A successful application of CSF-Eq to mixed color toner waste on an industrial scale would require a large scale-up of the throughput of the system. Increasing the particle concentration of the sample solution is an obvious method of increasing throughput. As seen in Equations 1 and 2, increasing the throughput could be achieved by increases in channel breadth, channel length, and centrifugal force. The flow rate of the system used in this study is already significantly higher than those traditionally used in centrifugal SF or SdFFF, but further increases are required to move the system beyond a preparative scale separation process. The improvements gained through the use of an asymmetrical splitter make these increases a possibility in CSF-Eq.

4.5 Conclusions

The experimental work presented in this paper studied the capabilities of CSF-Eq in the separation of toner particles. It was determined that secondary flows in the system have a large effect on the separation. With the system run in an antiparallel orientation, the purity of the less dense fraction decreased as rotation rates increased. This effect is a direct result of the development of secondary flows in the rotating channel. When an

asymmetrical outlet splitter was used, the purity of the more dense fraction was enhanced at higher rotation rates as the less dense particles in the vortices were blocked from entering the outer outlet. However, some of the more dense particles were also blocked from the outer outlet and were removed with the less dense fraction. While the system was not optimized, the potential for the use of an asymmetrical outlet splitter was demonstrated.

4.6 References

[1] Williams, E.M., *The Physics and Technology of Xerographic Processes*, John Wiley and Sons, New York City, NY, (1984).

[2] Ahmadi A., Williamson B.H., Theis T.L., Powers S.E., *J. Cleaner Prod.*, **11**(5), 573-592 (2003).

[3] Giddings J.C., *Sep. Sci. Technol.*, **20**, 749-768, (1985).

[4] Fuh C.B., *Anal. Chem.*, **72**(7), 266A-271A, (2000).

[5] Giddings J.C., *Science*, **260**(5113), 1456-1465 (1993).

[6] Giddings J.C., Yang F.J.F., Myers M.N., *Anal. Chem.*, **46**(13); 1917-1924 (1974).

[7] Fuh C.B., Myers M.N., Giddings J.C., *Anal. Chem.*, **64**(24), 3125–3132, (1992).

[8] Blo G., Conato C., Contado C., Fagioli F., Dondi F., *Annali Di Chimica*, **94**(9-10), 617-627 (2004).

[9] Contado C., Dondi F., Beckett R., Giddings J.C., *Anal. Chim. Acta.*, **345**(1-3), 99–110.

[10] Benincasa M.A., Moore L.R., Williams P.S., Poptic E., Carpino F., Zborowski M., *Anal. Chem.*, **77**(16): 5294-5301 (2005).

[11] Fuh C.B., Giddings J.C., *Sep. Sci. Technol.*, **32**, 2945–2967, (1997).

[12] Fuh C.B., Chen S.Y., *J. Chromatogr. A.*, **813**(2), 313-324 (1988)

[13] Fuh C.B., Giddings J.C., *Biotechnol. Prog.*, **11**, 14-20, (1995)

[14] Fuh C.B., Myers M.N., Giddings J.C., *Ind. Eng. Chem. Res.* **33**, 355-362, (1994).

[15] Camerani M.C., Steenari B.M., Sharma R., Beckett R., *Fuel*, **81**(13), 1739-1753, (2002).

[16] Schure M.R., Weeratunga S.K., *Anal. Chem.*, **63**, 2614-1616, (1991).

[17] Springston S.R., Myers M.N., Giddings J.C., *Anal. Chem.*, **59**(2), 344-350, (1987).

[18] Griffith O.M., *Techniques of Preparative, Zonal, and Continuous Flow Ultracentrifugation*, Beckman Inst., Fullerton, CA, DS-468H, (1994).

[19] Mitall K.L. (Ed.), *Particles on Surfaces: Detection, Adhesion and Removal*, Vols 5-8, VSP, Leiden, The Netherlands, (1999,1999, 2002, 2003).

[20] O'Neill M.E., *Chem. Eng. Sci.*, **23**(11), 1293-1298, (1968).

Chapter 5: Conclusions and Suggestions for Future Work

The goal of this work was to investigate the feasibility of separating mixed toner particles using centrifugal SPLITT fractionation (CSF). The numerical models presented in Chapter 3 showed that in CSF, the development of secondary flow near the end walls within the separation channel is inevitable. This secondary flow causes particles near the end walls to deviate from their trajectory towards their respective accumulation wall. The established use of thin channels for the separations was supported by the results of the analysis in an attempt to reduce the effect of the secondary flow on the separation. However, to further resolve the secondary flows and extend the range of feasible operating rotation rates, CSF operating in equilibrium mode (CSF-Eq) was the only option.

The experimental work presented in Chapter 4 describes the design, fabrication, and testing of an equilibrium SPLITT fractionation device. These results were used to verify the numerical modeling work in regards to particle trajectories and separation performance. The performance of a novel asymmetric splitter design was also part of the analysis. The best performance in a two component binary separation was seen for a system with the asymmetric splitter and equal face velocities in the two outlets at the splitter. This system achieved high purity (90+%) for both outlet streams. These results collectively prove the concept of using CSF-Eq for the separation of toner particles by density.

To extend this work back to the initial problem of the separation of mixed color toner waste, the toner particles must be engineered such that the density differences are inherent in the design. The density difference between the two particles tested in the binary separation was ~30 kg/m^3. This is a difference of less than 2.5%. As this is an initial analysis of the use of CSF for the separation of toner particles, the system is far from optimized. Thus, high purity separations should be possible for smaller density differences. Such particles could be fabricated in a variety of methods. One obvious method is to use different resins in the toners. For instance, the single component resin was a polystyrene/butadiene copolymer with a density of 1055 kg/m^3. This density is much less (15+%) than the polyester resin used in the binary separations.

Internal additives are another method for modifying the density of the toner particles. The black test particles in the binary separation used a small amount of magnetite, less than 4%, to increase the particle density as compared to the cyan particles. The high density of magnetite (ρ~5000 kg/m^3) makes it an ideal additive to increase the density of a toner particle. However, other factors limit the use of magnetite in such an application. First of all, magnetite is black in color, and is thus limited to use in black toner particles. Second of all, the magnetic nature of magnetite increases particle aggregation. This was seen in the black test particles. When aggregation was turned off, aggregates formed over a short time period (~5-10 minutes) and fell out of solution. The cyan particles, on the other hand, settled out over a much longer time period (~1-2 hours).

An alternative density modifier in toner particles is Titanium Dioxide (TiO_2). With a density of ~4000 kg/m^3, titania has a sufficient density difference from most resins to produce a significant shift in the particle density at low additive levels. The pure white color of titania is another advantage, as pigment colors would not be affected by the presence of this additive. Finally, titania is currently used in some toner formulations as an external additive to control the developed charge on the particles. Adding a small amount of titania as an internal additive would not change the surface concentration significantly, and any changes could certainly be adjusted for in the formulation. Other additives which could be used in toner particles include glass, silica, and certain pigments. With the use of any additive, a fairly uniform concentration of additive in each particle is required. Without this uniformity, a particle density distribution would result. This would certainly complicate the separation, as median density differences would need to be increasingly large to avoid overlap of the particle densities of the toner.

In addition to toner modifications required for the separation process to be used, the system itself also requires a substantial amount of development work to move the device from a laboratory scale process for separating particles at a gram per minute rate to an economically viable industrial process. An increase in the throughput of the system, in terms of the mass rate of particles being separated, can be achieved through many different means. As presented in Chapter 4, the theoretically derived maximum flowrate is:

$$\dot{V} = bL\frac{R\Omega^2\Delta\rho}{9\mu}d_p^2 \qquad (1)$$

One change which would increase the throughput of the system would be to modify the channel dimensions. By increasing the channel breadth, the volumetric flowrate could be increased while keeping the primary velocity relatively constant. Increasing the channel length would allow the particles more time to reach their equilibrium positions. An increase in the sedimentation force on the particles could be achieved by either increasing the radius of rotation, R, or the rotation rate, Ω. The rotation rate is especially attractive in that no changes to the system are required. Also, since the rotation rate is squared, small changes will result in much larger increases in the maximum flowrate. Increases in the particle density differences between the particle and carrier fluid as well as the particle size would also allow increases in the maximum flowrate of the separation system. Finally, a decrease in the system viscosity would increase the mobility of particles in the system. Thus particles would have a higher settling velocity and an increase in the maximum flowrate could be achieved.

Another method for increasing the throughput of the system is to increase the particle concentration. The particle loading in the current system was less than 0.5 vol% which ensured that particle-particle interactions were kept to a minimum in the solution. Increasing the particle loading would increase the particle throughput directly. However, there is a limit for particle concentration. At low particle concentrations, the rheology of the solution increases proportionately to particle concentration. Above a critical concentration, the viscosity increases very rapidly due to particle-particle interactions. The system most likely can handle a certain level of particle interactions assuming that

only van der Waals forces are driving any particle aggregation. Magnetic, electrostatic, or ionic forces would be more difficult to overcome.

Given a set of four particles with sufficient density differences to allow for particle separations, a system of CSF devices could be envisioned to enable complete separation of the four mixed toner particles. One such system is shown in Figure 5.1. This system shows an initial separation of the mixed toner into two fractions containing two colors each. These two fractions are then run through additional CSF devices for further purifications. Once the particles are sufficiently purified, they can be reintroduced directly into a conventional toner manufacturing process. As shown in the results from the life-cycle analysis presented in Chapter 2, recycling the toner into the toner manufacturing process has the potential to save on both raw materials usage and waste disposal fees.

Further experimental work to optimize the system is needed for the development of the CSF-Eq as applied to the separation of toner waste. In addition to the properties discussed above for increasing throughput, the channel design could also be modified further in an effort to resolve the effects of Coriolis force in the separation system. Possibilities such as an inlet sheath fluid to keep particles away from the end walls, or different end wall geometries to reduce the impact of secondary flow on the separation should be explored to determine their effects on system performance. Determining the bounds for particle concentration, rotation rates, particle properties, and channel designs would aid in the scale-up of the separation process to an industrial scale.

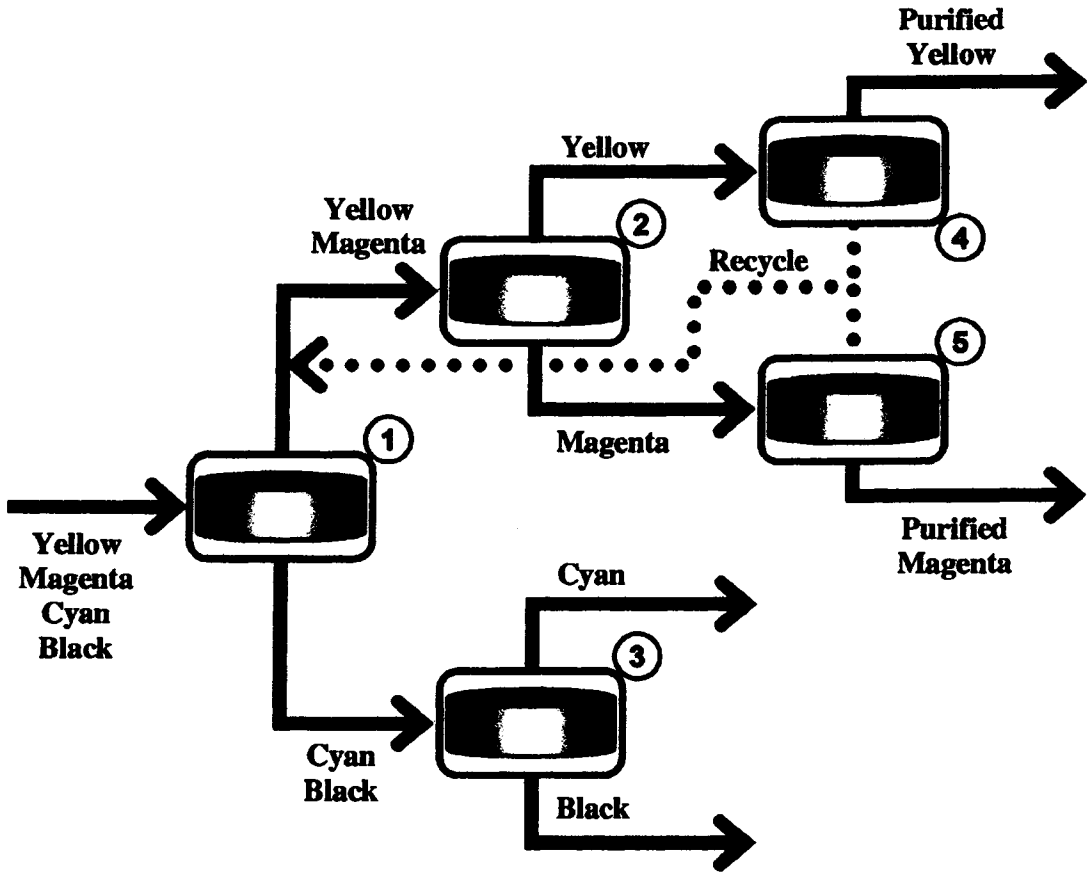

Figure 5.1. Series of CSF devices used for the separation of mixed color toner waste. The first separation device separates cyan and black (more dense) from magenta and yellow (less dense). These two streams are split again in device 2 and 3. Since the magenta and yellow toners are more sensitive to color contamination, additional separations may be required (4 and 5, with the residual toner waste recycled in the separation process).

Appendix A: Calibration of Flowmeter using Analytical Equations

Gilmont Accucal flowmeters were used in the experimental separations. These are variable area flowmeters with both glass and stainless steel floats included. Calibration data was included with the flowmeters for use with air and water. However, the solutions used in the experiments were not pure water. Since the results are dependent on the settling velocity of a spherical float through the carrier fluid, the flowmeter results were very sensitive to changes in the fluid properties. The viscosity of the sucrose solution was especially troublesome. One option to relate the reading from the flowmeter to the actual flowrate of the solution was to create calibration curves experimentally for every fluid to be used. Temperature variations in the fluid would be difficult to account for without performing further calibration experiments. This would be a very time consuming process with limited accuracy.

Another option was developed by Gilmont and Wechsler (1987) [1]. They developed a system of analytical equations which use physical parameters of the system to calculate the flowrate of the solution. The stated accuracy of the analytical equations is within a maximum of 6%, assuming that the fluid properties are known. A computer program is offered for purchase to accompany the flowmeters, but the equations were fairly straightforward. Therefore, an Excel spreadsheet was used to calculate flowrates. The equations are summarized in Omega Engineering report M1072 (Stamford, CT) and shown below. The inputs for the equations are the float position (used to calculate the "R" value), and the viscosity and density of the fluid. The two aqueous solutions used in

the separation experiments are both well characterized for density and viscosity at various temperatures and concentrations. The sucrose calculations for density were taken from an analytical equation relating temperature and sucrose concentration to solution density. The equation is valid from 0 – 100°C [2]. For the sucrose viscosity, an empirical relationship was used which is valid to within 1% error of the experimental results [3]. The CsCl solution properties were calculated using tabulated data in the International Critical Tables [4].

To test the calculated flowrates with experimental values, DI H_2O and a 50.9 wt% aqueous sucrose solution were used. A system was set up such that the test fluid was pumped through the flowmeter at a constant rate. The mass of the fluid pumped through the flowmeter for a set time was measured and the corresponding experimental flowrate was calculated. The position of the float in the flowmeter was also recorded. Using the average temperature of the fluid during the test and the known concentration of the solution, the flowrate was calculated using the analytical equations described in this section. The results are shown in Table A.1. This validates the use of the equations as a correlation of the float position to the fluid flowrate. All of the results agreed to within the 6% maximum error. Once the spreadsheet was developed, the inputs for the calculations were fluid temperature, flowmeter float level, and the density modifier concentration (wt% sucrose or CsCl). The spreadsheet would then calculate fluid density, fluid viscosity, and flowrate.

Below is the summary of the analytical equations derived by Gilmont and Wechsler as reported by Omega Engineering in report M1072:

ANALYTICAL SOLUTION OF FLUID FLOW

1. Select the desired value of R at the corresponding value of the scale division from the calibration curve supplied.
2. Calculate the value of K_R:

$$K_R = \frac{1.021}{\mu}\left[\frac{W_f(\rho_f - \rho)\rho}{\rho_f}\right]^{0.5}$$

where, μ = viscosity of fluid in cp
W_f = weight of float in g/cc
ρ_f = density of float in g/cc
ρ = density of fluid in g/cc
note, W_f and P_f are given in the calibration curve data.

3. Calculate the following:
   a) $St = K_R^2 R^3$
   b) $St_b = 5 + 777R$
4. Determine the region of flow as follows.
   a) If $St < 5$ region is Stokes, skip to step 9
   b) If $St_b \geq St \geq 5$ region is transitional, skip to step 6
   c) If $St > St_b$ region is turbulent, proceed to step 5
5. For the turbulent region, calculate the following:
   a) $V = \log[\log K_R - .350 + 1.5 \log R]$ (K_R from step 2)
   b) $W_c = n_0 + n_1 V + n_2 V^2 + n_3 V^3$
   where, $n_0 = -.197 + .00418R - .000155R^2$
   $n_1 = 1.065 - .0189R + .001375R^2$
   $n_2 = .929 - .1510R + .004025R^2$
   $n_3 = .542 - .06185R$, skip to step 7
6. For the transitional region calculate the following:
   a) $V_0 = \log[0.5 \log St_b - .360]$ (St_b from step 3b)
   b) $W_0 = n_0 + n_1 V_0 + n_2 V_0^2 + n_3 V_0^3$ (coeff. the same as in 5b)
   c) $W_c = W_0 - V_0 + V$ (V as calculated in Step 5a)
7. Calculate the following:
   a) $w_c = \log^{-1} W_c$
   b) $z_c = \log^{-1}(w_c + 0.1193)$
   c) $y_c = 10.040 - (1/z_c)$
   d) $C_R = \log^{-1}(y_c - 10)$
8. Determine the value of K_t as follows. ($K_t = 1$ for gases)
   a) $v = \log^{-1} V$ (V from step 5a)
   b) $R_t = \frac{100}{m_0 + m_1 v}$
   where, $m_0 = 4.81 - 138\frac{R^3}{1000}$
   $m_1 = -2.82 + 369\frac{R^2}{100}$
   c) $K_t = 1 - \frac{\rho}{\rho_f}\left[\frac{R}{R_t}\right]^2$ Skip to step 10
9. For the Stokes region calculate.
   a) $C_R = .0852(St)^{0.5}$
   b) $K_t = 1 - \frac{\rho}{\rho_f}\left[\frac{m_0 R}{100}\right]^2$ (m_0 from step 8b)
10. Calculate the volumetric flow at the conditions of flow

$$q = C_R K_q R\left[\frac{R}{100} + 2\right] K_t$$

where, $K_q = 59.6\, D_t\left[\frac{W_f(\rho_f - \mu)}{\rho\rho_f}\right]^{0.5}$

11. The above flow (q) may be reduced to a volume measured at standard conditions (q') as follows:

$$q' = q\frac{\rho}{\rho_0} \quad \text{where, } \rho_0 = \text{density at std. cond}$$

SAMPLE CALCULATIONS

Flowmeter, Size #1, F1100, Glass Float, W_f = .00530 g, ρ_f = 2.53 g/cc, D_t = .0625 in. Water at 40 °C, μ = .653 cp., ρ = .992 g/cc, ρ_0 = .998 g/cc. Values of R at 5, 10 & 25

$$K_R = \frac{1.021}{.653}\left[\frac{.00530(2.53 - .992).992}{2.53}\right]^{0.5} = .06836,\ K_q = .2130$$

R	C_R	v	$100/R_t$	K_t	q	q'
5	.0842	—	—	1	184	183
10	.233	.097	4.44	.923	.962	.956
25	.526	.693	2.30	.870	5.48	5.46

SAMPLE CALCULATIONS FOR ANALYTICAL SOLUTION

1.	R:	5	10	25
2.	K_R = .06836 for all values of R			
3.	St = .00781 R^3			
	a) St:	.975	7.81	122.0
	b) St_b:	8.885	12.77	24.4
4.	Region:	Stokes	transitional	turbulent
5.	a) V:			−.1592
	b) W_c:			−.4249
	n_0:		−.1707	−.1894
	n_1:		1.0315	1.4519
	n_2:		−.1785	−.3304
	n_3:		−.0765	−1.0043
6.	a) V_0:		−.6923	
	b) W_0:		−.9325	
	V:		−1.0613	
	c) W_c:		−1.2565	
7.	a) w_c:		.0654	.3760
	b) z_c:		1.495	3.126
	c) y_c:		9.371	9.72
	d) C_R:		.235	.525
8.	a) v:		.09632	.6931
	b) R_t:		22.54	43.52
	m_0:		4.672	2.654
	m_1:		−2.451	−5.138
	c) K_t:		.923	.871
9.	a) C_R:	.0842		
	b) m_0:	4.79		
	K_t:	.977		
10.	K_q = .2130 for all values of R			
	q:	.180	.970	5.48

Table A.1. Experimental and analytical calculations of fluid flowrate for DI-H_2O and an aqueous sucrose solution

wt% sucrose	Solution Density	Float Level	Volumetric Flowrate (mL/min)		% error
			Experimental	Analytical	
0	998.6	7.5	9.6	9.9	3.0%
0	998.6	12	22.4	22.4	0.2%
0	998.6	16.5	37.0	36.2	2.4%
0	998.6	19.5	48.2	46.2	4.2%
0	998.6	23.5	63.8	60.2	5.6%
50.9%	1233	15.5	2.4	2.4	-0.9%
50.9%	1233	27	8.4	8.1	-3.1%
50.9%	1233	35	14.4	14.5	0.3%
50.9%	1233	42	21.1	21.7	3.1%

References

[1] Gilmont R., and Wechsler L., *Meas. and Cont.*, **21**(6), p.148-160, (1987).

[2] Bubnik Z., Kadlek P., Urban D., and Bruhns M., **Sugar Technologists Manual**; p. 164, Bartens (1995).

[3] Mathlouthi M., and Génotelle J., *Rheological properties of sucrose solutions and suspensions*, **Sucrose: Properties and Applications**, M.Mathlouthi and P. Reiser eds., Blackie Academic & Professional pp. 126-154 (1995).

[4] **International Critical Tables of Numerical Data, Physics, Chemistry and Technology (1st Electronic Edition),** Ed. Washburn E.W., Knovel, (2003).

Appendix B: Calibration of Turbidometer for Particle Concentration

A Hach 2100N turbidometer was used as a quick and easy method of determining the concentration of particles in a solution. Under ideal conditions, particle concentration is proportional to the turbidity (NTU). To test this, calibration curves were developed for the test particles in three aqueous sucrose solutions. As shown in Figure B.1, the relationship between the particle concentration and turbidity for royal blue (TEST) toner particles is nearly linear. The data were fitted to fourth order polynomials, which were used to interpolate the turbidity readings with the sucrose concentration to determine the particle concentration (vol%). However, the results for black toner (EXP-10) deviated sharply away from linearity at relatively low concentrations. This limited the use of the turbidity experiments to single component solutions of royal blue toner.

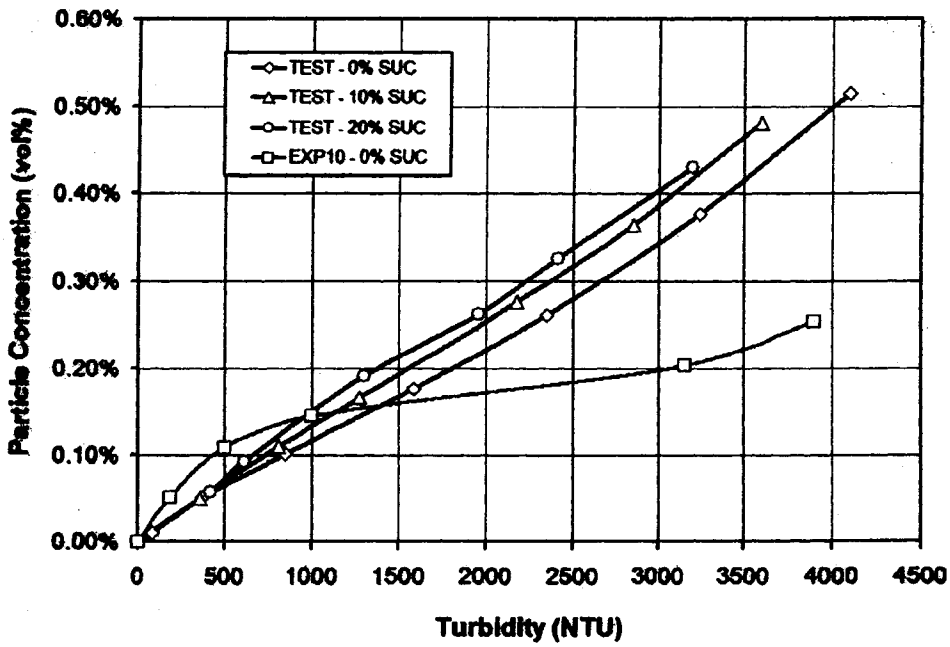

Figure B.1 Calibration curves for royal blue (TEST) and black (EXP-10) toners.

Appendix C: Calculations Used in Determining Particle Concentrations from Optical Microscopy

Optical microscopy was used to analyze the relative particle concentrations of two particles in a binary system. Image acquisition is described in Chapter 4.3. The resulting images show a two dimensional image of the particles. MetaMorph software was then used to analyze the images. Due to the large number of images and particles per image, a methodology was defined to relate the image data to a usable concentration ratio of the two particles. The MetaMorph software isolates particles in an image and counts the "number of pixels" in each particle. This pixel count is proportional to the cross sectional area of the particle. Since the analysis will return the relative particle concentration, the units of length (pixel vs meter) is not important, as long as they are consistent throughout the analysis. Thus, the pixel area can be converted to a pixel radius:

$$A = \pi r^2 \rightarrow r = \sqrt{A/\pi} \qquad \text{C.1}$$

where A is the particle cross sectional area, and r is the particle radius. The volume of a single particle can then be calculated directly:

$$V = \frac{4}{3}\pi r^3 = \frac{4}{3}\frac{A^{3/2}}{\sqrt{\pi}} \qquad \text{C.2}$$

Ideally, all particles would be separate from one another in the image. However, there are many instances where the particles will begin to aggregate together. This causes the particles to be seen as one large particle by the software. To resolve this, the pixel size was related back to the physical size of the toner particles. For the most part, the particles were contained within a thin section of the sample slide. Thus, the aggregates

were oriented in the plane of the sample. There was some overlap of the aggregate particles and it was determined that it is best to treat these particle aggregates as two dimensional plates with a standard thickness, d_s. This thickness was chosen as 9.9 pixel lengths, which was calculated from the median size of the particles (6.4 μm). Multiplying the measured area by this thickness was then used for the total particle volume of aggregated particles. Therefore, two regions for the particles are used: single particles which are converted to volume by Equation C.2, and particle aggregates which are converted to volume by multiplying the pixel area by the standard thickness. To make the curve continuous, a standard area, A_s value was calculated by setting the two volume equations equal:

$$\frac{4A_s^{3/2}}{3\sqrt{\pi}} = A_s d_s \qquad \text{C.3}$$

Solving for A_s and substituting d_s=9.9 gives A_s=173. The response curve for this analysis is shown in Figure C.1. Thus for every particle in the image, the corresponding volume can be calculated.

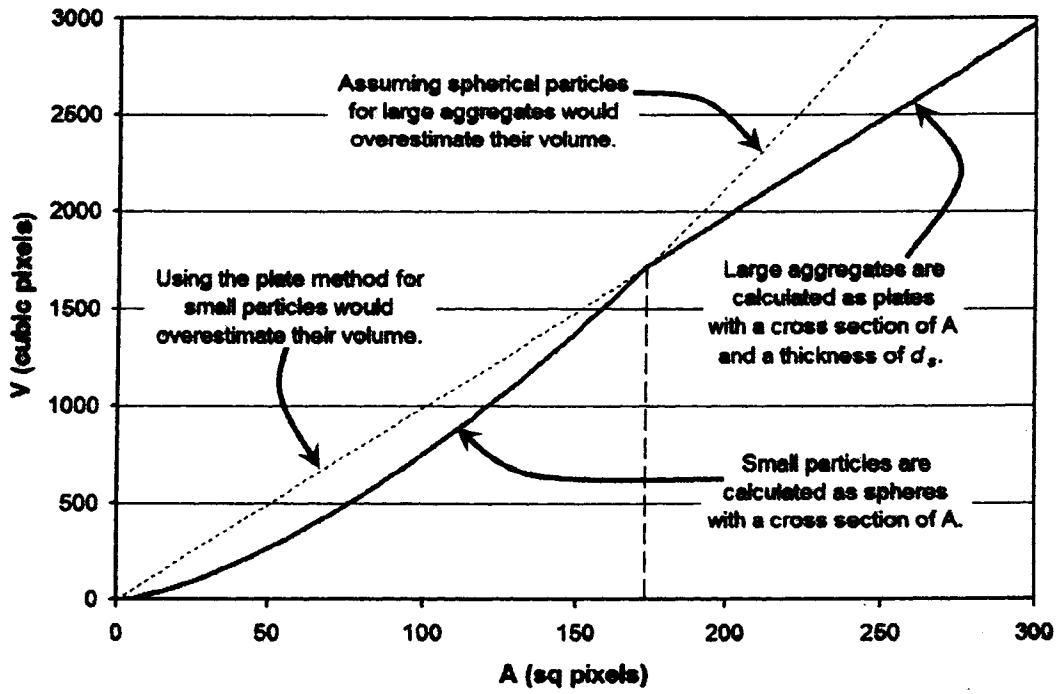

Figure C.1 Response curve for the optical microscopy analysis.